Coherent Manipulation of Rydberg Helium Atoms in Inhomogeneous Electric Fields

A Dissertation Presented

by

Seung Hyun Lee

to

The Graduate School

in Partial Fulfillment of the Requirements

for the Degree of

Doctor of Philosophy

in

Physics

Stony Brook University

August 2006

Stony Brook University

The Graduate School

Seung Hyun Lee

We, the dissertation committee for the above candidate for the Doctor of Philosophy degree, hereby recommend acceptance of the dissertation.

Professor Harold J. Metcalf, Advisor
Department of Physics and Astronomy

Professor Emilio E. Mendez, Chairman of Defense
Department of Physics and Astronomy

Professor Philip M. Johnson
Department of Chemistry

Adjunct Professor Thomas H. Bergeman
Department of Physics and Astronomy

This dissertation is accepted by the Graduate School.

Dean of the Graduate School

Abstract of the Dissertation

Coherent Manipulation of Rydberg Helium Atoms in Inhomogeneous Electric Fields

by

Seung Hyun Lee

Doctor of Philosophy

in

Physics

Stony Brook University

2006

Coherent manipulation of atomic motion has been a subject of increased interest in atomic physics because it provides the opportunity to perform precision spectroscopy. Since the first demonstration of laser cooling techniques, exerting controlled optical forces on neutral atoms has made it possible to develop new tools for working on the near-atomic scale. While most of these tools are based on manipulating atoms with laser light, a different method which exploits the interaction of Rydberg atoms with inhomogeneous electrostatic fields to control the atomic motion was proposed in 1981.

Atoms in Rydberg states have a large dipole moment because their outer electrons are located far from the core. Due to the relatively strong dipole interaction, therefore, the motion of Rydberg atoms can be affected even by weak and moderate field gradients. Ultimately, it is desirable to maximize the population in the Rydberg states to increase the intensity of the beam focused by an electrostatic lens. In a new approach to achieve a highly efficient population transfer, we take advantage of the highly efficient Stimulated Raman Adiabatic Passage (STIRAP) excitation technique.

In this thesis, we first present an investigation of the Stark-shifted atomic energy levels and compare our observations to numerical calculations. Once the state with the highest transition efficiency has been identified we employ the coherent STIRAP excitation technique in order to achieve a complete population transfer from the metastable ground state to the target state via an intermediate state in the three-level ladder system $2^3S_1 \rightarrow 3^3P_2 \rightarrow nL_j$ of triplet helium. In order to fulfill the strict conditions for STIRAP, we also need to know the Rabi frequencies of the laser fields. For this purpose, the Autler-Townes effect is also examined.

Finally, we demonstrate an example of atom optics by focusing the atomic beam with our electrostatic lens after preparing the

metastable helium atoms in one of the well-defined Rydberg states. Possible applications of this new technique are nanofabrication or lithography.

To my family

SungYeon, InHo and InHyuk

Contents

List of Figures

Acknowledgements

I will give thanks to the LORD according to His righteousness,

And will sing praise to the name of the LORD Most High.

(Psalms 7:17)

By coming to Stony Brook in August 2001, I took a first step toward having a novel experience in the United States. Even though it was very difficult to acclimate myself to a new environment in the beginning, I have completed this thesis work under the full support of those who have contributed both directly to this work and also to my life in New York over the past five years.

I have been very lucky to join one of the great atomic physics groups in the world. When I was in Korea I read the book, *Laser Cooling and Trapping*, written by Harold Metcalf, and I'm very glad that I successfully applied for a position as a graduate student in his group and thus had the opportunity to meet him in person. Directly after my arrival in the US, he helped us to settle down and started to take care of my family very warmly and nicely, etc. It is too much to list what he has done for us. Especially, he has given me constant guidance and encouragement throughout my research.

I also cannot forget my first great friend at Stony Brook, Matt Cashen. He found the new home for my family and gave us the first chance to see New York city. Looking back over the years, I recall with heartfelt gratitude his family's inviting us to New Hampshire. Due to the Cashens, we have another family in the United States.

I am also glad to have made friends with Matt Partlow, Matt Eardley, Oleg Kritsun, and Olexiy Boyko. Singing a song while watching the starry sky on the Sound Beach was a very impressive experience. Especially, working with both Oleg and Olexiy will forever be imprinted on my memory. Since my experimental system often required an extra pair of hands, I really appreciate the help of Kyung Soo Choi and Jonathan Kaufman which made big progress in my experiment possible. I believe that they will be great physicists.

We have had several exchange students in our group; Benjamin Dietzek, Joerg Bochmann, Matthias Riedmann, and Michael Keller from Germany and Esther Wertz from France. Meeting all of them was a very special chance to not only experience different cultures but also to build friendship all over the world. Together with Xiyue Miao, Claire Shean, and Jason Reeves we used to have a really good time in and outside the lab. My experiences with all of them definitely enriched my life.

I would especially like to acknowledge the theoretical calculations and comments of Tom Bergemann in our AMO group, who is one of the most generous persons I have ever met. I have thoroughly enjoyed our discussions about my work. Marty Cohen has dedicated his time and knowledge to this group, and his advice was always helpful. I thank Emilio Mendez and Philip Johnson for

being in my committee and correcting my thesis.

I would also like to thank the staff in our department for their assistance over the years, especially Pat Peiliker for helping me and my family with warmth. Diane Siegel, Maria Hofer, and Linda Dixon have also always been helpful. I would like to thank Pete Davis, Walter Schmeling, and Mark Jablonski, who always helped me in the machine shop and with numerous hardware problems.

I am very fortunate to have accepted plenty of useful advice from Heung-Ryoul Noh and Jaewan Kim. They gave me practical guidance whenever I met some trouble with my experiment. For this I am forever grateful.

An important part of these acknowledgements should be addressed to my great coworker, Andy Vernaleken, who spent a lot of time to correct my thesis. We left the laboratory with the dew of dawn many times. If my life in this laboratory started with Matt Cashen, then now it's the right time to complete my work here with Andy. (*GamSaHamNiDa, Andy !*)

Finally, I'm deeply indebted and inexpressibly grateful to my whole family who dedicated a tremendous part of their lives to my thesis. My mother-in-law and my mother took turns and came to the United States several times to help us, which made it possible for me to concentrate on doing research. My wife has had faith in me and supported me for a long time ever since I started to study physics. She and my two sons, InHo and InHyuk, have been my continuous source of joy.

I was granted the opportunity to do research at Stony Brook and supported by the Republic of Korea Air Force.

Chapter 1

Introduction

1.1 General Background

There has been great interest in developing new techniques to exert controlled force on the atoms and to manipulate atomic trajectories [1]. To control the motion of atoms and exploit their wave-like properties it is crucial to invent elements which have the same effect on atoms as mirrors, lenses, beam splitters, etc. on light [2]. The possibility of the field of *atom optics* can be traced back to Kepler [3]. The trajectory of a comet tail is directed away from the sun because the light of the sun carries momentum and thus affects the trajectory of the tail. If we explain this situation from the classical viewpoint of the atom-field interaction, the light force on atoms comes from the dipole potential due to the light [3]:

$$V(\mathbf{x}, \mathbf{r}, t) = -\mathbf{d} \cdot \mathbf{E}(\mathbf{r}, t) \tag{1.1}$$

where $\mathbf{d}$ is the electric dipole moment, $\mathbf{r}$ the center-of-mass coordinate of the atom, $\mathbf{x}$ the position of the electron relative to the nucleus, and $\mathbf{E}(\mathbf{r}, t)$ is the

electric field. This fact explains the possibility that the atomic trajectories can be manipulated by the dipole force of the field.

Although this classical picture of atoms moving in a comet tail without regard to their overall wave-like character has been of great use, the explanation of recent experiments on atom optics requires a quantum mechanical atom-photon interaction model [2]. In 1923, Louis de Broglie proposed that all massive particles should be thought of as waves [4] and that the wave-like properties of any massive particle of mass M could be characterized by the so-called de Broglie wavelength [3]

$$\lambda_{dB} = \frac{h}{Mv} \tag{1.2}$$

where h is Planck's constant and v the particle velocity. The first experimental confirmation of Eq.(1.2) was done for the case of electrons by Davisson and Germer in 1927 [5]. A further development was established by Otto Stern and co-workers in 1929 who demonstrated that atoms can be reflected and diffracted from metal surfaces [6].

At that time, it was exceedingly difficult to detect the wave-like properties of thermal atoms because the dependence of the thermal de Broglie wavelength on the temperature T $\left(\lambda_{th} \propto 1/\sqrt{T}\right)$ gives $\lambda_{th} \approx 10^2$ nm at room temperature [7]. Effects of such short wavelength are enormously difficult to observe. Thus the results of those experiments can be regarded as the starting point of experimental atom optics.

Further developments in this field depended critically on increasing the thermal wavelength by lowering the temperature so that profound progress

towards manipulating atomic motion was directly linked with the invention of the laser. One of the first experiments with lasers was done by Cook and Hill [8], who suggested that an atom is reflected from a dielectric surface in the thin transmitted evanescent wave of laser radiation. The evanescent wave is formed on the dielectrics surface if blue detuned laser light is totally reflected internally at a vacuum-dielectric interface. Thus the evanescent wave acts as an atomic mirror.

For the first experimental observation of atomic diffraction Pritchard and his coworkers [9] employed an optical standing wave as a diffraction grating. In addition to atomic mirrors and diffraction gratings, there have been several experiments to build coherent atomic beam splitters. In a first experiment, Moskowitz *et al.* [10] showed that an atomic beam crossing a standing wave is split into two symmetric peaks.

Among all these developments one of the most important achievement in atomic physics was initiated by Wineland and Dehmelt [11] and Hänsch and Schawlow [12] who discussed new ideas for using laser light to cool atoms. They realized that atoms can be cooled to very low temperature using laser light pressure [2]. In fact, laser cooling techniques enable us to produce atomic samples as cold as several micro-Kelvin. Even lower temperatures down to the order of a few nano-Kelvin were achieved by a technique called evaporative cooling [2]. which, in particular, made possible the first observation of Bose-Einstein condensates (BECs) in 1995 [13] which ever since have been studied intensively [14]. For high-resolution experiments, BECs have excellent properties: ultra-low temperature, high density, and a well-defined quantum state

[15, 16, 17].

The manipulation of the transverse motion of an atomic beam to increase its brightness, that is, the number of atoms per second and steradian (atoms/sr·s), has been a subject of interest because a well-collimated atomic beam can be a useful tool for atom optics applications. However, the main obstacle comes from the fact that electrostatic potentials $V(\mathbf{r})$ created up to date are too weak compared with the typical kinetic energies of thermal atoms [19]. In most cases, for example, the velocity spread of thermal atoms is on the order of 500 m/s.

Consider an atom in a typical laboratory electric field of magnitude $\sim 10^3$ V/m with a gradient of about 10^6 V/m^2. The polarizability α of the atom, which is defined by the relation between the induced dipole moment $\mathbf{d}$ of the atom and the electric field $\mathbf{E}$ as $\mathbf{d} = \alpha\mathbf{E}$, is typically on the order of $\sim 10^{-50}$ farad·m^2 [20]. Therefore, we can just get a very small acceleration of $\sim 10^{-15}$ m/s^2 for thermal atoms. This shows that the interaction of a ground state neutral atom with an electrostatic field can be neglected. Hence, it is important to either develop the methods to increase $V(\mathbf{r})$ to gain more control of the atomic external (motional) state, or to make the interaction stronger through controlling the atomic internal (electronic) state. The optical bichromatic force is an example for the former case and its application to nanolithography has been developed in our group [21, 22]. As an example of the latter case, we can change the internal state of the atoms by exciting them to high principle quantum numbers (n $>$ 15) called Rydberg states whose huge dipole moments will naturally cause a stronger dipole interaction. This is the

method we use in our experiment.

In this chapter, several key concepts of the manipulation of atoms with lasers will be presented.

1.2 Atom-Photon Interaction

The motion of an atom traversing a laser beam can be derived starting from the Hamiltonian of the atomic system [2, 3].

$$H = H_A + H_{AF} \tag{1.3}$$

where H_A is the atomic Hamitonian and H_{AF} describes the interaction between the atom and the laser field. For a two-level atom of mass M with lower electronic level $|g\rangle$, upper electronic level $|e\rangle$ and Bohr transition frequency ω_0, the atomic Hamiltonian can be expressed as [3]

$$H_A = \frac{\mathbf{p}^2}{2M} + \hbar\omega_0 |e\rangle \langle e| \tag{1.4}$$

Here $\mathbf{p}$ is the atomic center-of-mass momentum. The internal energy of the lower state is set to zero. In the optical field region, the electric dipole approximation is valid to describe the interaction between optical fields and atoms [23], and we have [3]

$$H_{AF} = -\mathbf{d} \cdot \mathbf{E}(\mathbf{r}, t) \tag{1.5}$$

where $\mathbf{d}$ is the atomic dipole moment, and can be represented as

$$\mathbf{d} = q\mathbf{r}(|e\rangle \langle g| + |g\rangle \langle e|) \tag{1.6}$$

with the electric charge q. If we treat the field classically, it can be written in the general form

$$\mathbf{E}(\mathbf{r},t) = \mathbf{e}_k(\mathbf{r})E_0(\mathbf{r})\cos[\omega t + \phi(\mathbf{r})] \tag{1.7}$$

where ω is the frequency of the field and ϕ the phase. k represents the polarization direction of the electric field in a spherical basis. If we choose the quantization axis properly, k can be a single value 0 or ± 1 for linear- or $\sigma^{\pm}$-circular polarized light. This is associated with the components in the Cartesian space as follows: $\mathbf{e}_0 = \mathbf{e}_z$ and $\mathbf{e}_{\pm} = \mp\frac{1}{\sqrt{2}}(\mathbf{e}_x \pm i\mathbf{e}_y)$. Using Eqs.(1.5) -(1.7), the interaction Hamiltonian can be expressed as

$$H_{AL} = \hbar\Omega\cos(\omega t + \phi)\,\{\ |e\rangle\langle g| + |g\rangle\langle e|\ \} \tag{1.8}$$

Here we define the Rabi frequency Ω associated with the strength of a transition between two atomic states $|g\rangle$ and $|e\rangle$ by the expression [24]

$$\hbar\Omega = -qE_0\langle e|\,\mathbf{e}_k\cdot\mathbf{r}\,|g\rangle = -qE_0\langle e|\,r_k\,|g\rangle \tag{1.9}$$

The procedure for evaluating the matrix element $\langle e|\,r_k\,|g\rangle$ in an atom with no hyperfine structure such as helium is to first invoke the Wigner-Eckart theorem [24, 25] to get

$$\begin{aligned}\langle e|\,r_k\,|g\rangle &= \langle nSLJM_J|\,r_k\,|n'S'L'J'M'_J\rangle \\ &= (-1)^{J-M_J}\begin{pmatrix} J & 1 & J' \\ -M_J & k & M'_J\end{pmatrix}\langle nSLJ\|\,r_k\,\|n'S'L'J'\rangle\end{aligned} \tag{1.10}$$

where $(\cdots)$ is a Wigner 3j symbol. The reduced matrix element, $\langle nSLJ\|\,r_k\,\|n'S'L'J'\rangle$,

can be evaluated in terms of a reduced matrix element in L representation as [24, 25]

$$\begin{aligned}\langle nSLJ\|\, r_k \,\|n'S'L'J'\rangle &= \delta(S,S')(-1)^{S+L'+J+1}\sqrt{(2J+1)(2J'+1)} \\ &\times \left\{ \begin{array}{ccc} L & J & S \\ -J' & L' & 1 \end{array} \right\} \langle nL\|\, r_k \,\|n'L'\rangle \end{aligned} \tag{1.11}$$

where $\{\cdots\}$ is a Wigner 6j symbol and $\delta(S,S')=0$ unless $S=S'$. Substituting Eq.(1.11) into Eq.(1.10) leads to

$$\begin{aligned}\langle e|\, r_k \,|g\rangle &= (-1)^{2J+S+L'-M_J+1}\sqrt{(2J+1)(2J'+1)} \left(\begin{array}{ccc} J & 1 & J' \\ -M_J & k & M'_J \end{array} \right) \\ &\times \left\{ \begin{array}{ccc} L & J & S \\ -J' & L' & 1 \end{array} \right\} \langle nL\|\, r_k \,\|n'L'\rangle \end{aligned} \tag{1.12}$$

As a selection rule, $k = M'_J - M_J$ should be satisfied. The values for the 3j and 6j symbols can be found in Ref.[24]. In addition, the reduced matrix element is related to the spontaneous emission rate Γ and wavelength λ of the transition between the upper state $|nL\rangle$ and the lower state and $|n'L'\rangle$ as [24]

$$\langle nL\,\|r_k\|\,n'L'\rangle = \sqrt{2L+1}\left(\frac{3\lambda^3\Gamma}{32\pi^3 c\alpha}\right)^{1/2}\delta(L',L-1) \tag{1.13}$$

where α $\left(= \frac{1}{4\pi\varepsilon_0}\frac{e^2}{\hbar c}\right)$ is the fine structure constant and c the speed of light. Using this result (1.13) and the electric field amplitude $E_0 = \sqrt{\frac{2I}{\varepsilon_0 c}}$ (where I is the intensity of the radiation field), the Rabi frequency can be obtained.

The saturation parameter s_0 is also defined as [2]

$$s_0 = I/I_s = 2\Omega^2 \Big/ \Gamma^2 \tag{1.14}$$

where I_s is the saturation intensity which is given in Eq.(1.16).

1.3 Excitation Scheme of Metastable Helium

The metastable helium (He^*) beam in our experiment is produced by a DC glow discharge. Then the 2^3S_1 metastable state can be regarded as the ground state in the 3-level ladder scheme that we use because of its long lifetime ($\sim$ 8000 sec)

Figure 1.1 shows the excitation scheme of He^* from the state 2^3S_1 to the Rydberg state $26S$. The excitations are done with two linearly polarized laser beams, a blue one (λ = 389 nm light, which is generated by an external frequency-doubling cavity) for the first transition ($2^3S_1 \rightarrow 3^3P_2$), and a red one ($\lambda$ = 796.762 $\sim$796.763 nm light). We use a two-step process for experimental ease of light generation.

In order to see how the Rabi frequencies are affected by the polarizations of the applied fields, we first consider the transition $|1\rangle \rightarrow |2\rangle$ with σ^+-circular polarized beams. In this configuration, the atoms are optically pumped into the ground state sublevel $M'_J = 1$. Therefore, the relevant transition is $M'_J =$

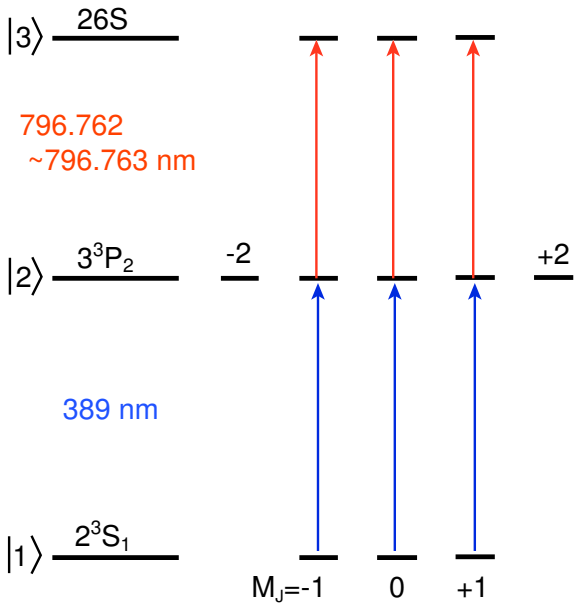

Figure 1.1: Excitation scheme of He* from the 2^3S_1 metastable ground state to the $26S$ Rydberg state bond by only ~ 500 GHz using two linearly polarized laser beams.

$1 \rightarrow M_J = 2$ and we get

$$\langle 3P_2 M_J \, |r_k| \, 2S_1 M_J' \rangle = \sqrt{1/3} \;\; \langle 3P \, \| r_k \| \, 2S \rangle \tag{1.15}$$

Substituting Eq.(1.15) into Eq.(1.9), and using Eqs.(1.13) and (1.14) leads to

$$I_s = \frac{\pi hc}{3\lambda^3} \Gamma_2 \tag{1.16}$$

Here we use Γ_2 as the spontaneous emission rate of level $|2\rangle$ (3^3P_2) which can be evaluated from Eq.(1.13) using the reduced matrix element $\langle 3P \, \| r_k \| \, 2S \rangle = 0.9 \; a_0$ (a_0 : Bohr radius). This gives the values $\Gamma_2 = 2\pi \times 1.49$ MHz, which corresponds to a lifetime of $\tau_2 = \Gamma_2^{-1} = 106.83$ ns for the 3^3P_2 state, and we get

$I_s = 3.31$ mW/cm^2 for the $\lambda = 388.98$ nm transition [2]. Thus the Rabi frequency, $\Omega_0 = \Gamma_2\sqrt{s/2}$ (Ω_0 : Rabi frequency for the transition of $|1\rangle \rightarrow |2\rangle$ with circular polarization beams), can be evaluated using Eq.(1.14) if the intensity of the radiation field I for the transition is known.

For the linearly polarized case, the matrix elements [Eq. (1.12)] can be expressed as

$$\begin{aligned} \langle 3P_2 M_J \left| r_k \right| 2S_1 M_J' \rangle &= \beta \cdot \underbrace{\sqrt{1/3}\ \langle 3P \left\| r_k \right\| 2S \rangle}_{\text{for } \sigma^+\text{–pol.}}, \\ \beta &= \begin{cases} \sqrt{2/3} & for M_J = M_J' = 0 \\ \sqrt{1/2} & for M_J = M_J' = \pm 1 \end{cases} \end{aligned} \tag{1.17}$$

There are three different contributions to the transition strengths from the states having $M_J = 0, \pm 1$ and the Rabi frequencies for these states can be expressed by $\Omega_l(0) = \sqrt{2/3}\ \Omega_0$ and $\Omega_l(\pm 1) = \sqrt{1/2}\ \Omega_0$ for $M_J = 0$ and $M_J = \pm 1$, respectively. But these values are approximately equal, and we can thus take the average Rabi frequency for the linear polarization case to be $\Omega_l \approx 0.75\ \Omega_0$. In principle, the evaluation of the Rabi frequencies for the second excitation, $|2\rangle \rightarrow |3\rangle$, to the Rydberg states follows the same procedure as explained the above. The reduced matrix element was calculated $\langle 26S \left\| r_k \right\| 3P \rangle = 0.079\ a_0$ and the lifetime of the state 26S is evaluated to be $\sim 40\ \mu s$.

1.4 Motivation and Outlook of Thesis

In 1981, T.Breeden and H.Metcalf [1] suggested that a non-uniform electric field can be used to decelerate a beam of highly excited thermal atoms, whose electric dipole moments are large because they scale as the orbital radius ($r \sim n^2$). In van der Straten's group, the intensity of the flux in their experiment was increased by focusing the atoms with a magnetic hexapole lens [26]. These results reveal that atoms in Rydberg states can also be focused with inhomogeneous electro-static fields produced by a electrostatic hexapole lens.

The purpose of this experiment is to manipulate the atomic trajectories of helium atoms using the strong dipole interaction of the atoms with a moderate electric field. A strong dipole interaction in a moderate electric field is based on a large atomic dipole moment which is one of the exaggerated properties of Rydberg atoms. In our system, Rydberg helium atoms are created driving the optical two-photon transition from the metastable ground state to highly excited Rydberg states. The energy level structure for an atom in a highly excited state is dominated by the Stark interaction. Thus, understanding the behavior of the Stark energy level is a prerequisite for carrying out this experiment.

The properties and the Stark energy levels of Rydberg atoms are described in Chapter 4. In order to increase the transition efficiency to the Rydberg states we employ the Stimulated Raman Adiabatic Passage (STIRAP) technique, whose details are explained in Chapter 5. In addition, the method to

produce the 389 nm blue beam is presented in Chapter 2. The vacuum systems and the laser systems including the feedback systems used to stabilize the laser frequencies are described in Chapter 3. Details on the construction of the electrostatic lens and a brief numerical calculation associated with the potential produced by the lens can be found in Chapter 6. A discussion of all the experimental results will be the final Chapter 7.

Chapter 2

LBO-based Second Harmonic Generation (SHG)

2.1 Introduction

We employ the transitions $2^3S_1 \rightarrow 3^3P_2 \rightarrow nL_J$ (nL_J : Rydberg states) of the three-level cascade scheme (see Figure 3.1) to excite metastable helium atoms to Rydberg states. Therefore, a laser beam at $\lambda = 389$ nm for coupling the two states $2^3S_1 \rightarrow 3^3P_2$ is required. As it is also pointed out in Section 5.4 in order to produce a highly efficient population transfer via the STIRAP technique, this 389 nm beam must have a high enough Rabi frequency ($\geq$ few tens of MHz) and its optical frequency also needs to be stabilized. In our system, we can achieve this by second harmonic generation (SHG) of a continuous wave Ti:Sapphire laser in an external enhancement cavity containing a nonlinear LBO (LiB_3O_5) crystal. More thorough and elaborate discussion of SHG can be found in [19, 27, 28, 29, 30, 31, 32, 33]. Therefore the theoretical review of SHG in this thesis will be focused on the case of the LBO crystal

used in this experiment instead of describing all different types of crystals. The stabilization methods of our doubling cavity will be also discussed in this chapter.

2.2 Second Harmonic Generation

The polarization $\mathbf{P}$ induced in a medium when a monochromatic plane wave, $\mathbf{E}(\mathbf{k},\omega) = \mathbf{e}E\exp\{i(\mathbf{k}\cdot\mathbf{r}-\omega t)\}$, is applied can be expanded as

$$\mathbf{P}(\mathbf{k},\omega) = \mathbf{P}^{(1)}(\mathbf{k},\omega) + \mathbf{P}^{(2)}(\mathbf{k},\omega) + \mathbf{P}^{(3)}(\mathbf{k},\omega) + \cdots \tag{2.1}$$

with

$$\begin{aligned}
\mathbf{P}^{(1)}(\mathbf{k},\omega) &= \epsilon_0\chi^{(1)}(\mathbf{k},-\omega;\omega):\mathbf{E}(\mathbf{k},\omega), \\
\mathbf{P}^{(2)}(\mathbf{k},\omega) &= \varepsilon_0\chi^{(2)}(\mathbf{k},-2\omega;\omega,\omega):\mathbf{E}(\mathbf{k},\omega)\,\mathbf{E}(\mathbf{k},\omega), \\
\mathbf{P}^{(3)}(\mathbf{k},\omega) &= \varepsilon_0\chi^{(3)}(\mathbf{k},-3\omega;\omega,\omega,\omega):\mathbf{E}(\mathbf{k},\omega)\,\mathbf{E}(\mathbf{k},\omega)\,\mathbf{E}(\mathbf{k},\omega)
\end{aligned} \tag{2.2}$$

where $\chi^{(n)}$ is the $nth-order$ nonlinear susceptibility of the medium whose dependence on the wave vector $\mathbf{k}$ can be neglected because its effect is practically very small. Therefore, using Einstein's summation convention, the second order polarization vector $\mathbf{P}^{(2)}(\omega)$ in a medium may be represented by

$$P_k^{(2)} = \varepsilon_0\chi_{klm}^{(2)}E_lE_m \tag{2.3}$$

$\chi_{klm}^{(2)}$ is a $(3\times3\times3)$ third-rank tensor whose elements are restricted by the spatial symmetry of the crystal structure [34]. It is especially convenient to rewrite $\chi_{klm}^{(2)}$ in a contracted form, in which the two symmetric subscripts l

and m are replaced by a single subscript j such that

$$xx \to 1,\ yy \to 2,\ zz \to 3,\ yz \to 4,\ zx \to 5,\ xy \to 6 \tag{2.4}$$

Using this contracted matrix form, the so called 3×6 Kleinman d_{ij}-tensor [33, 35], Eq.(2.3) can be written as

$$\begin{pmatrix} P_x \\ P_y \\ P_z \end{pmatrix} = \varepsilon_0 \begin{pmatrix} d_{11} & d_{12} & d_{13} & d_{14} & d_{15} & d_{16} \\ d_{21} & d_{22} & d_{23} & d_{24} & d_{25} & d_{26} \\ d_{31} & d_{32} & d_{33} & d_{34} & d_{35} & d_{36} \end{pmatrix} \times \begin{pmatrix} E_x^2 \\ E_y^2 \\ E_z^2 \\ 2E_yE_z \\ 2E_zE_x \\ 2E_xE_y \end{pmatrix} \tag{2.5}$$

For the majority of crystals, only a few of the d_{ij} coefficients have to be known. In an LBO crystal, for example, symmetry requires that all the d_{ij} vanish except d_{31}, d_{32}, and d_{33} [27] . Although we can calculate the second harmonic polarization using the above equations, this is only true for infinitesimal volume elements. That is to say that only the local second harmonic polarization can be calculated according to Eqs.(2.3) and (2.5). On a macroscopic scale, the total second harmonic polarization is the sum of the individual contributions from all the infinitesimal elements of the crystal. For efficient second harmonic generation, these infinitesimal contributions throughout the material

must add coherently. Due to inevitable material dispersion, however, waves of different frequencies propagate at different phase velocities. Consequently, the problem of phase-matching between second harmonic fields generated at different positions in a material should be considered.

For simplicity we consider the one-dimensional case in a material of length L and assume a fundamental wave of the form [30]:

$$E^{(1)}(x) = E^{(1)}(0) \cdot e^{-ik_\omega x} \tag{2.6}$$

where k_ω is the wave vector for the optical frequency ω and the refractive index n_ω, which is defined by $k_\omega = n_\omega \omega / c$ (c : speed of light in free space).
The second harmonic polarization can be calculated using Eq.(2.3), and the susceptibility tensor $\chi^{(2)}$ reduces to the one scalar coefficient d_{eff}.

$$P^{(2)}(x) = 2d_{eff}E^{(1)}(x)\,E^{(1)}(x) = 2d_{eff}E^{(1)}(0)\,E^{(1)}(0) \cdot e^{-2ik_\omega x} \tag{2.7}$$

where d_{eff} is a function of the suitable element of the Kleinman d-tensor. For example, this effective tensor element $d_{eff} = d_{32} \cdot \cos\Theta_P$ can be used in an LBO crystal (Θ_P : phase matching angle) [27]. The polarization $P^{(2)}(x)$ acts as a driving force in the Maxwell equations for $E^{(2)}(x)$ [32, 31, 33],

$$\frac{\partial^2}{\partial x^2}E^{(2)} - \left(\frac{n}{c}\right)\frac{\partial^2}{\partial t^2}E^{(2)} = \mu\frac{\partial^2}{\partial t^2}P^{(2)} \tag{2.8}$$

Now $E^{(2)}(x)$, the solution of the wave equation (2.8), travels through the material with frequency 2ω and wave vector $k_{2\omega}$. At an arbitrary position x' in the material the second harmonic wave becomes

$$\begin{aligned} E^{(2)}(x') &= E^{(2)}(x) \cdot e^{-ik_{2\omega}(x'-x)} \\ &\propto \left|E^{(1)}(0)\right|^2 e^{-ik_{2\omega}x'} e^{-i(2k_\omega - k_{2\omega})x} \end{aligned} \tag{2.9}$$

Thus the total second harmonic field generated in a material for $(0 < x < L)$ can be calculated by integrating all contributions from $E^{(2)}(x')$, and we finally get [32]

$$E^{(2)}_{total}(x') \propto e^{-ik_{2\omega}x'} e^{iL\Delta k/2} \cdot \frac{\sin(L\Delta k/2)}{\Delta k/2} \tag{2.10}$$

with

$$\Delta k = k_{2\omega} - 2k_{\omega} = \frac{4\pi}{\lambda}\{n_{2\omega} - n_{\omega}\} \tag{2.11}$$

where λ is the wavelength of the fundamental field.

From Eqs.(2.10) and (2.11), the *coherence length* L_c, which is a measure of the maximum length of the nonlinear medium that is useful in producing second harmonic waves, can be defined as

$$L_c = \frac{\lambda}{2\{n_{2\omega} - n_{\omega}\}} \tag{2.12}$$

For some typical values ($\lambda = 780$ nm , $n_{2\omega} - n_{\omega} = 10^{-2}$) we find a coherence length of 39 μm. The proof of the coherence length effect is given in an experiment by Maker *et al* [36]. The generated second harmonic beam intensity $I_{2\omega}$ can be calculated at the exit of the nonlinear medium ($x = L$) [37].

$$I_{2\omega} = \frac{8\pi^2 d^2_{eff} I^2_{\omega} L^2}{c\varepsilon_0 n^2_{\omega} n_{2\omega}} \cdot \frac{\sin^2(L\Delta k/2)}{(\Delta k/2)^2} \tag{2.13}$$

The maximum intensity of second harmonic light $I^{\max}_{2\omega}$ is achieved at $\Delta k = 0$, that is, $n_{2\omega} = n_{\omega}$. But there is always dispersion in a medium like LBO, and the intensity $I_{2\omega}$ decreases dramatically with Δk ($\neq 0$). Therefore, the key to achieving high efficiency second harmonic frequency light is increasing the coherence length L_c.

2.2.1 Nonlinear Crystal

Consider an electromagnetic wave (propagation direction $\mathbf{k}$) incident on the surface of a birefringent nonlinear crystal. The polarization of the incident wave can be split into two orthogonal components along two different axes of the crystal. The Fresnel equation describes that these two waves see different indices of refraction and thus propagate with different angles in the crystal, a phenomenon referred to as *birefringence* [31]. The general method to find the index of refraction for the different polarizations of a propagating wave is to use a three dimensional ellipsoid [32],

$$\frac{x^2}{n_x^2} + \frac{y^2}{n_y^2} + \frac{z^2}{n_z^2} = 1 \tag{2.14}$$

where x, y, z are the principal axes of a crystal, and n_i $(i = x, y, z)$ is the index of refraction along the axis i.

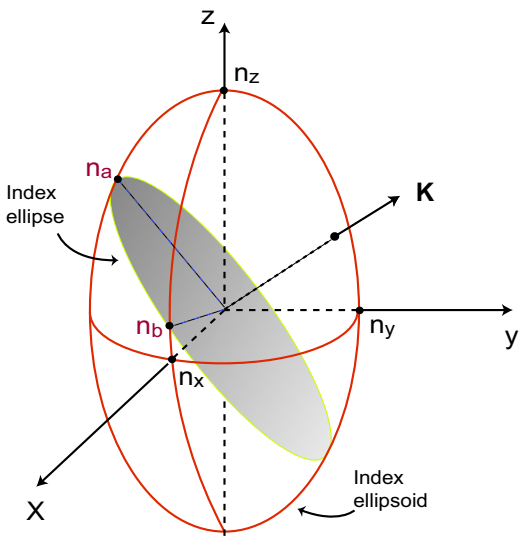

Figure 2.1: Index ellipsoid and Index ellipse.

For the case of the wave traveling in the direction of **k**, the plane perpendicular to **k** going through the center of the ellipsoid intersects the ellipsoid given in Eq.(2.14) and forms an ellipse, whose major and minor axes determine two polarization directions in a crystal as shown in Figure 2.1. The length of each axis represents the index of refraction along the axis, n_a and n_b . Suppose the ellipse has a cylindrical symmetry about the z-axis and the wave is propagating along the z-axis. In this case the intersecting plane normal to the direction of propagation (z-axis) will form a circle and the wave sees only one refractive index. We call the propagating direction in which the refractive index is independent of polarization the *optical axis*.

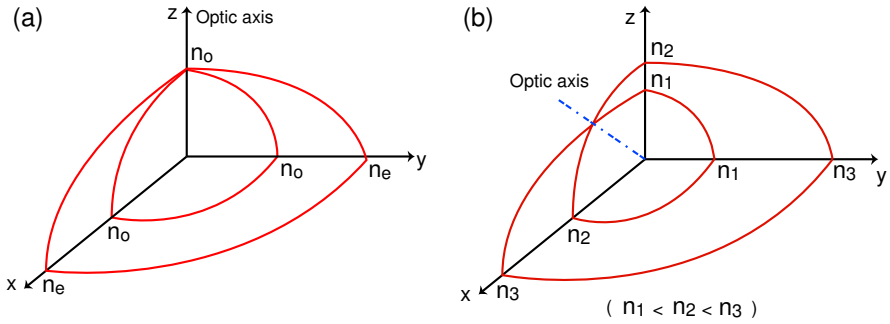

Figure 2.2: Refractive index surfaces. (a) uniaxial crystal (b) biaxial crystal

By the directional dependence of the refractive index, a crystal can be divided into two classes - *uniaxial* and *biaxial* [32]. As shown in Figure 2.2, there are always two different refractive indices seen by a propagating wave

in any direction except one special direction (optical axis) of the wave vector. This fact makes it possible for the wave propagating in the crystal to have two different polarizations. For an uniaxial crystal, only the wave propagating along the z-axis sees one index of refraction value. So there is only one optical axis [Figure 2.2(a)]. However, if there is no cylindrical symmetry axis as shown in Figure 2.2(b), all three refractive indices are different ($n_1 < n_2 < n_3$) and the optical axis is along a direction other than any of the principal axes. There are two optical axes, one in shown in Figure 2.2(b) and its symmetry equivalent, in a biaxial crystal. In a birefringent crystal, the two waves whose polarizations are orthogonal to each other have special names - ordinary and extraordinary wave. The ordinary wave has a polarization perpendicular to the *principal plane* formed by the optical axis and the propagation direction. For the ordinary wave, the crystal has a constant index of refraction n_o. The polarization of the extraordinary wave lies in the principal plane, and the refractive index for the extraordinary wave n_e is dependent on the angle between the optical axis and the propagation direction $\mathbf{k}$.

2.2.2 Phase Matching

In a birefringent crystal the refractive index depends on the direction of the polarization of the wave propagating in the crystal. Using this property, the index of refraction for the fundamental and second harmonic wave can be matched in a nonlinear crystal [27]. Figure 2.3 shows the directional dependence of the refractive index for a biaxial LBO crystal.

It is shown that in the $XY(\theta = 90^o)$ and XZ ($\phi = 0, \theta$ between Z and

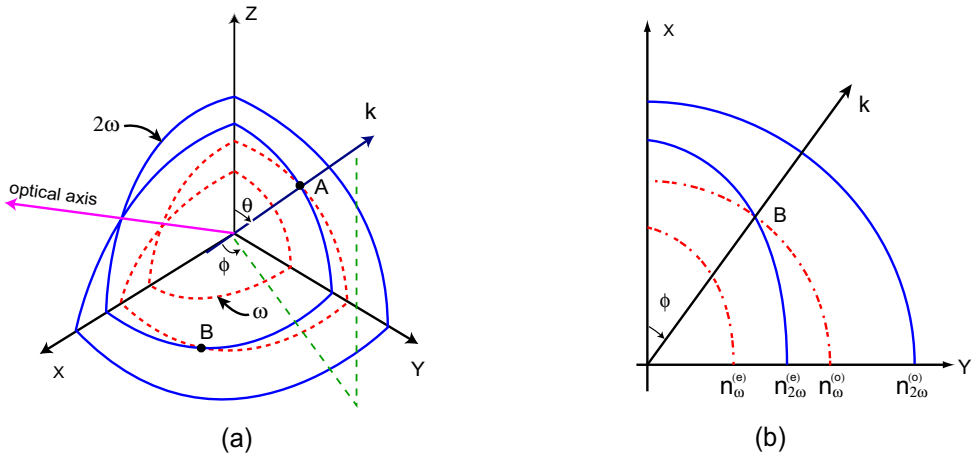

Figure 2.3: Refractive index surfaces for the birefringent LBO crystal. (a) biaxial case and (b) negative uniaxial case ($n^{(e)} < n^{(o)}, \theta = 90^o$)

optical axis) planes the crystal can be thought of as a negative uniaxial crystal because of $n^{(e)} < n^{(o)}$, whereas it shows the same behavior as a positive uniaxial one in the YZ ($\phi = 90^o$) and $XZ(\phi = 0, \theta$ between X and optical axis) planes. In *positive birefringent crystals*, for which $n^{(e)} > n^{(o)}$, the second harmonic wave is polarized along the ordinary axis that gives the lower refractive index $n_{2\omega}^{(o)}$. At point A, one can realize the phase matching condition $n_{2\omega}^{(o)} = n_{\omega}^{(e)}(\theta)$. Therefore, two fundamental waves with the same polarization create a second harmonic wave. This type of phase matching is called *TYPE-I phase matching*. It is also possible to create a wave at the second harmonic frequency with two fundamental waves having orthogonal polarizations to each other, referred to as *TYPE-II phase matching*. In this case the phase matching condition $n_{2\omega}^{(o)} = \frac{1}{2}\left[n_{\omega}^{(o)} + n_{\omega}^{(e)}(\theta)\right]$ must be satisfied, and it is not favorable to realize in practice.

In the case of a *negative birefringent crystal* ($n^{(o)} > n^{(e)}$) the polarization of the second harmonic wave is along the extraordinary axis. At point B in Figure 2.3(b), phase matching can be achieved for $n^{(e)}_{2\omega}(\phi) = n^{(o)}_{\omega}$, such that the fundamental waves polarized along the ordinary axis $n^{(o)}_{\omega}$ create a second harmonic wave along the extraordinary axis. Figure 2.3(b) shows the negative uniaxial phase matching condition in the case of $\theta = 90^o$. The phase matching condition explained above is based on tuning the angles (θ, ϕ), a technique referred to as *critical phase matching*, whereas *non-critical phase matching* is based on accurate temperature control utilizing the temperature dependence of refractive indices for some crystals.

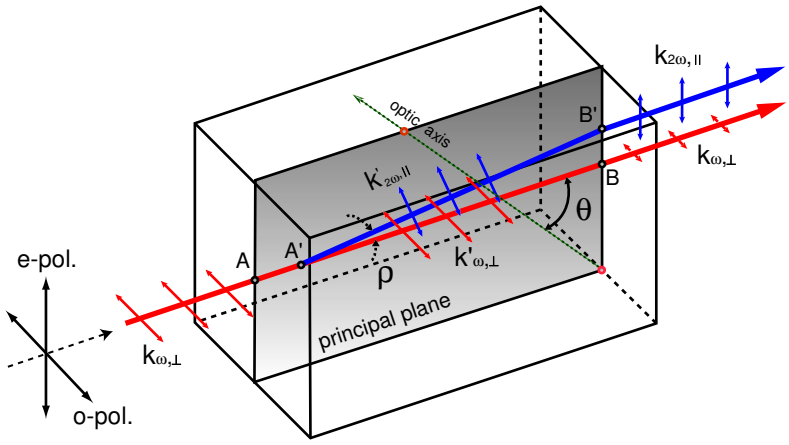

Figure 2.4: Critical phase matching in a uniaxial negative birefringent crystal.[38]

As mentioned above, a biaxial LBO crystal can be thought of as a negative uniaxial crystal when satisfying the phase matching condition at point B in Figure 2.3(b). Therefore we may consider phase matching practically with Figure 2.4 [38]. Suppose the second harmonic wave is generated at a point A'

when the fundamental wave $\mathbf{k}_{\omega,\perp}$ travels along the line AB. The polarization of the second harmonic wave is perpendicular to the polarization of the fundamental wave in this configuration, the so-called *Type-I phase matching* [32]. Therefore, the second harmonic component $\mathbf{k}'_{2\omega,\parallel}$ in the crystal will be polarized along the principal plane and will also have a different phase velocity. In order to achieve the phase matching condition, the angle θ can be adjusted by rotating the crystal about an axis perpendicular to the principal plane. This is called *critical phase matching*.

As obvious from the description of phase matching in a birefringent crystal, there is a geometric *walk-off* of the second harmonic wave from the fundamental wave, specified by the *walk-off angle* ρ. In Eq.(2.13), the conversion efficiency increases quadratically as a function of crystal length L. The effect of the walk-off is a reduction of the spatial interaction length, which restricts the intensity of the second harmonic wave.

2.2.3 SHG for a Focused Gaussian Beam

The intensity of the second harmonic wave is given in Eq.(2.13) for the case of a plane wave. The equation shows that the intensity is proportional to the square of the length of the crystal and to the square of the intensity of the fundamental wave. In practice, the output mode of most laser systems has a Gaussian transverse beam intensity profile, implying that a tightly focused beam in the crystal will ensure the greatest power conversion efficiency due to a higher power density. However, this also decreases the *Rayleigh length*, which is defined by $z_R = \pi w_0/\lambda$ (w_0: beam waist at the focal point, λ :

wavelength)[31], and increases the divergence angle of the beam. For TYPE-I phase matching, in addition, there is always a walk-off effect that limits the spatial interaction length. The optimal second harmonic generation coefficient γ_{SHG} in the case of TYPE-I phase matching under the consideration of these effects was derived by Boyd and Kleinman in 1968 [35]:

$$\gamma_{SHG} = \frac{P_{2\omega}}{P_{\omega}^2} = \frac{128\pi^2\omega^2 d_{eff}^2 k_{\omega} L}{c^3 n_{\omega}^2 n_{2\omega}} \cdot h\left(B, \xi\right) \tag{2.15}$$

The factor $h\left(B, \xi\right)$ is the Boyd-Kleinman focusing parameter that depends on both the walk-off parameter $B = \rho_{walk-off}\left(Lk_{\omega}\right)^{1/2}/2$ and the focusing parameter $\xi = L/w_0^2 k_{\omega}$.

2.3 Selection of Nonlinear Crystal

When selecting a nonlinear crystal for frequency doubling of a 780 nm Ti:Sapphire laser, the most important thing to consider is how to get the highest possible conversion efficiency. The Eqs.(2.13) and (2.15) show that a higher conversion efficiency can be achieved through higher power density, longer crystal length, smaller phase mismatching, and larger nonlinear coefficients. However, there is always some limitation, for example, the nonlinear crystal coefficients are intrinsic properties that cannot be altered and the maximum input power is limited by the damage threshold of the crystal.

In Type-I critical phase matching, the fundamental wave is incident on a crystal with the phase matching angle. A small amount of divergence of

the beam and a small deviation from phase matching angle cause a dramatic reduction of the conversion efficiency. If the beam divergence angle is larger than the acceptance angle of the crystal, only a fraction of the input beam is involved in the doubling process. Among many different nonlinear crystals, three candidates can be considered for frequency doubling of 778 nm light: BBO (beta-barium borate), LBO (lithium tri-borate), and $LiIO_3$ (lithium iodate). More details on the optical properties of these crystals can be found in [29, 40]. Of these three candidates, LBO has the highest damage threshold (2.5 GW/cm^2), the smallest walk-off angle (17 mrad), and the largest acceptance angle (4.3 mrad) at a wavelength of 780 nm. For Type-I critical phase matching in the XY-plane (see Figure 2.3) the nonlinear coefficient d_{eff} is given by $d_{eff} = d_{32} \cos\phi$ and $\phi = 33.73^o$. The dimension of our LBO crystal is $3 \times 3 \times 18$ mm. In this case, the maximum second harmonic efficiency can be estimated to be $\gamma_{SHG} = 1.6 \times 10^{-4}$ W^{-1} and the estimated optical waist size in the crystal is $w_0 = 31$ μm. For a more detailed description of our LBO crystal, see Ref.[29].

2.4 Performance of the SHG Cavity

The power of single pass second harmonic generation through the LBO crystal is expected not to be enough for the STIRAP experiment because the value of γ_{SHG} is only a small number on the order of 10^{-4} W^{-1}. To achieve higher second harmonic power, thus, a significantly higher fundamental power is needed. A promising tool to increase the available fundamental power is

an external enhancement resonant cavity (EEC). For a theoretical calculation of the second harmonic output of an EEC, we can use the external resonator SHG theory of Ashkin *et al.* [41]. For a given incident fundamental power P_ω, the circulating power P_c of the fundamental light on resonance in the doubling cavity becomes [42]

$$P_c = \frac{T_1 P_\omega}{\left(1 - \sqrt{R_1 R_m}\right)^2} \tag{2.16}$$

Here, R_1 and T_1 $(= 1 - R_1)$ denote the reflectivity and the transmission coefficient of the input coupling mirror M_1, respectively [see in Figure 2.5]. R_m is the reflectivity of the cavity except the input coupler M_1.

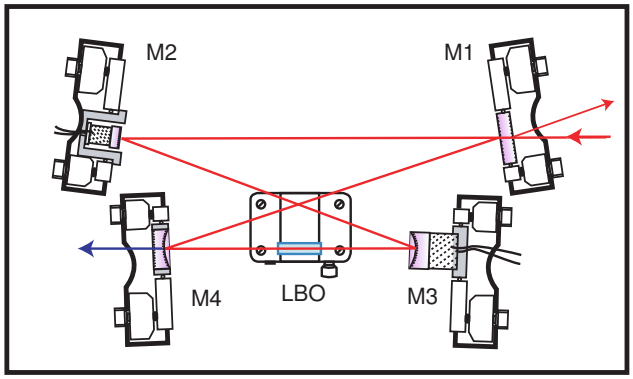

Figure 2.5: External Frequency Doubling Cavity

Thus R_m can be thought of as the effective round trip loss caused by the remaining cavity mirrors ($M_2 \sim M_4$) as well as losses within the LBO crystal. From Eq. (2.16), the maximum circulating power P_c is achieved when the reflectivity R_1 is equal to the cavity loss R_m. This condition is referred to as impedance matching to maximize the power inside the cavity. Now, if we consider the generation of second harmonic light by the circulating power, conversion losses caused by SHG itself should be included and the Eq.(2.16) should be modified to [38, 42]

$$P_c = \frac{T_1 P_\omega}{\left[1 - \sqrt{R_1 R_m \left(1 - \gamma_{SHG} P_\omega\right)}\right]^2} \tag{2.17}$$

Thus, we can calculate the output power $P_{2\omega}$ of SHG with respect to the various losses and transmissions of the input coupler using the relation, $P_{2\omega} = \gamma_{SHG} P_c^2$, as shown in Figure 2.6 [43].

The maximum total measured output power of our doubling cavity was $\sim$ 450 mW. But if we filter the transmitted red component out of the total output, a *pure* blue power $P_{2\omega}$ of $\sim$ 200 mW was measured. This corresponds to total losses of about 2 % from Figure 2.6. According to Ref.[43] possible sources of losses ($\sim$ 1 %) are reflections on the surface of the LBO crystal (0.2 %), absorption and scattering due to impurities in the LBO crystal (0.7 %), and the cavity mirrors (3×0.05 %). Therefore, most losses are caused by misalignment of the cavity.

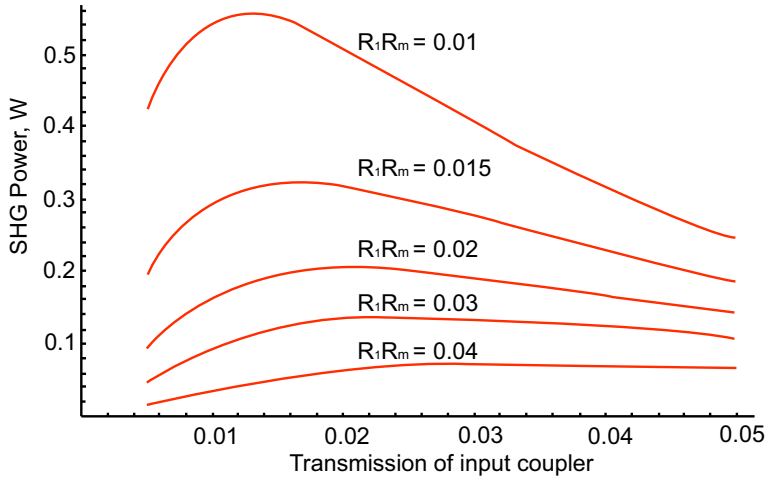

Figure 2.6: Calculated variation of the power $P_{2\omega}$ of the SHG with respect to the transmission T_1 of the input coupler for various losses $R_1 R_m$. The calculation is performed with $P_\omega = 1.5$ W and $\gamma_{SHG} = 1.6 \times 10^{-4}$ W^{-1}.

2.5 External SHG Cavity

Our four-mirror ring resonator, shown in Figure 2.5, is mounted on an aluminum based optical breadboard that is isolated from the dust free optical table by a thick sheet of rubber. The fundamental beam is coupled into the doubling cavity through a 1- inch diameter flat mirror M_1, whose transmission is about $T = 1.8 \sim 2.4$ % at 778 nm. The other flat mirror M_2 and the two curved mirrors (M_3, M_4) are high-reflection (HR) coated for 778 nm. The radius of curvature and the diameter of both curved mirrors is 150 mm and 12.7 mm, respectively. Furthermore, M_4 has a transmission of more than 95 % at 389 nm.

To be able to apply a feedback signal to lock the cavity, the small mirror M_2(6 mm diameter) is mounted on a PZT (piezoelectric stack) whose max-

imum displacement is 3.0 ± 1.5 μm with an applied voltage of 100 V. The bandwidth is 250 kHz so that a fast actuation is possible. In addition to the fast feedback signal a slower PZT is attached to the curved mirror M_3 because the fast PZT has a limited range of motion. This slow mirror M_3 is driven by a higher voltage (up to 1000 V) so that it is possible to compensate changes in a larger range ($\sim$ 4 μm) on a slower time scale ($\sim$10 Hz). Therefore, we can adjust the cavity length roughly to the resonant position and the fast correction signal can be applied to the cavity. The LBO crystal is mounted to a copper block so that any heat generated by the high power laser beam can be dissipated from the crystal. The copper block is attached to a stage that allows to translate and to tilt the crystal. An anti-reflection coating on the two optical facets gives a reflectivity of less than 0.25 % for the fundamental beam and a transmission coefficient larger than 95 % for the second harmonic beam. More practical information on how our doubling cavity was built can be found in Ref.[29].

2.6 Alignment Procedure and Electronic Stabilization

2.6.1 Cavity Alignment

We have learned how to align the frequency doubling cavity on the basis of the instructional manual from Tekhnoscan [44], and I quote the manual in this section because it describes a suitable procedure for our doubling cavity.

First, the doubling cavity can be roughly aligned without scanning its length. Thus all control electronics should be turned off.

The infrared laser beam (778 nm) is guided using mirror M (in Figure 2.7) such that it comes through the center of the input coupler M_1 and hits the small mirror M_2. Then, the beam from M_2 is guided to the center of the spherical mirror M_3 by adjusting M_2. Now, the control knobs of M_3 are used to make the beam pass through the LBO crystal and hit M_4. The first step to achieve a closed loop is to make the beam from M_4 hit the same spot as the first transmitted input beam on the input coupler M_1. Second, M_1 is adjusted so that the transmitted incoming beam from mirror M and the reflected beam from M_1 that already ran one round trip in the cavity travel along the same path. Further adjustment should be continued until an infrared flash appears inside the doubling cavity. Once the light flash is observed, the ramp generator to scan the cavity by applying a high voltage to the PZT2 is turned on [see in Figure 2.8(b)].

After fine alignment of the mount for the LBO crystal a blue spot appears in the output region. To take a part of the blue beam, which in turn hits a photo diode detector (not shown in Figure 2.7), a beam splitter is inserted in the output beam of the doubling cavity. The photo diode (PD) may easily be saturated, so that a filter must be positioned in front of the PD. The output cable of the PD is connected to an oscilloscope which should be synchronized by the trigger signal (TTL) from the ramp generator. Further fine alignment of the cavity mirrors ($M_1 \sim M_4$) is required to optimize the signal and maximize the height of the transmission peaks.

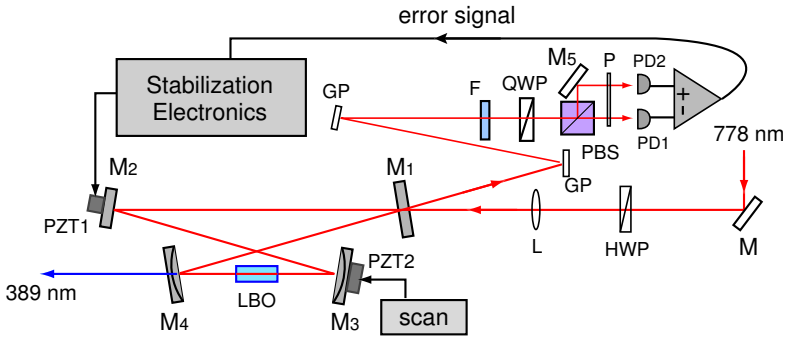

Figure 2.7: Schematic design of SHG : M-mirror, L-mode matching mirror, HWP-half wave plate, QWP-quarter wave plate, GP-glass plate, PBS-polarization beam splitter, P-polarizer, F-neutral density filter, PD-photodiode detector

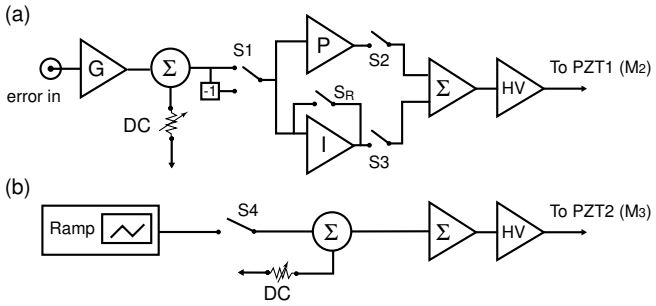

Figure 2.8: Control Electronics for the doubling cavity : G-gain control, S-switch, Σ-summing junction, P-proportional, I-integral, HV-high voltage amplifier

Under certain conditions, the height of some of the peaks dominates all the others [see Figure 2.9(a)]. The adjustment procedure with the mirrors and the LBO mount needs to be continued until periodical high peaks with one or two small peaks in between are observed. In the case of ideal alignment, only the clear periodical high peaks without any small peak between them can be seen. The small peaks can be further minimized by careful adjustment of the input beam with mirror M in Figure 2.7. Furthermore, the correct polarization of the input beam can be chosen by rotating a half wave-plate (HWP in Figure 2.7) such that the output of the doubling cavity is maximized.

2.6.2 Hänsch-Couillaud Method

Various perturbations can cause deviations of the doubling cavity from resonance. To compensate for these deviations and to stabilize the resonance cavity, Hänsch and Couillaud introduced a polarization spectroscopy method [45] that is commonly referred to as the Hänsch-Couillaud method. Consider an incident beam whose polarization axis is rotated with a HWP (see Figure 2.7) and forms an angle θ with the transmission axis ($o - pol.$ axis in Figure 2.4) of the doubling cavity. Thus, the incident beam can be decomposed into two orthogonal linearly polarized components: $E_{\parallel} = E\cos\theta$ and $E_{\perp} = E\sin\theta$ (E : amplitude of the incident beam) are the electric field components parallel and perpendicular to the transmission axis.

The perpendicular component $E_{\perp}$ is simply reflected by the input coupler M_1 and serves as a reference, while the parallel component $E_{\parallel}$ sees a cavity of low loss and experiences a frequency-dependent phase shift in reflection

depending on the direction of the cavity length deviation from the resonance position. For example, if the cavity length changes from resonance to a shorter length, the component that made one round trip in the cavity will be ahead in phase by an amount $(-\delta)$ compared to the component that was directly reflected from the input coupler. Similarly, a deviation to a longer cavity length causes a delayed phase shift $(+\delta)$. Ideally, there is no reflection of $E_{\parallel}$ when the cavity becomes resonant [see in Figure 2.9 (b)] and the quarter wave-plate (QWP in Figure 2.7) creates circularly polarized light just out of the $E_{\perp}$-component. Otherwise, the QWP generates elliptically polarized light with a relative phase difference δ between the two reflected components. After passing through the QWP and a polarization beam splitter (PBS) cube, we get [45]

$$I_1 - I_2 = 2I \cos\theta \sin\theta \frac{T_1 R_m \sin\delta}{(1 - R_m)^2 + 4R \sin^2(\delta/2)} \tag{2.18}$$

where I is the intensity of the incident beam, I_i $(i = 1, 2)$ is the intensity measured by the PD, and the quantities T_1, R_m are defined in Eq.(2.16). The signal of Eq.(2.18) can be used as an error signal to stabilize the cavity. The produced error signal in our set-up is shown in Figure 2.9(c). Only a small fraction of the incident beam needs to be reflected as a reference to create the error signal, and thus, a very small θ ensures a higher intensity of the circulating beam which gives a larger output of the cavity. After observing the reflected beam shown in Figure 2.9(b), the error signal is generated by rotating the QWP. The intensities at both photo diodes have to be balanced with a polarizer to get the correct error signals.

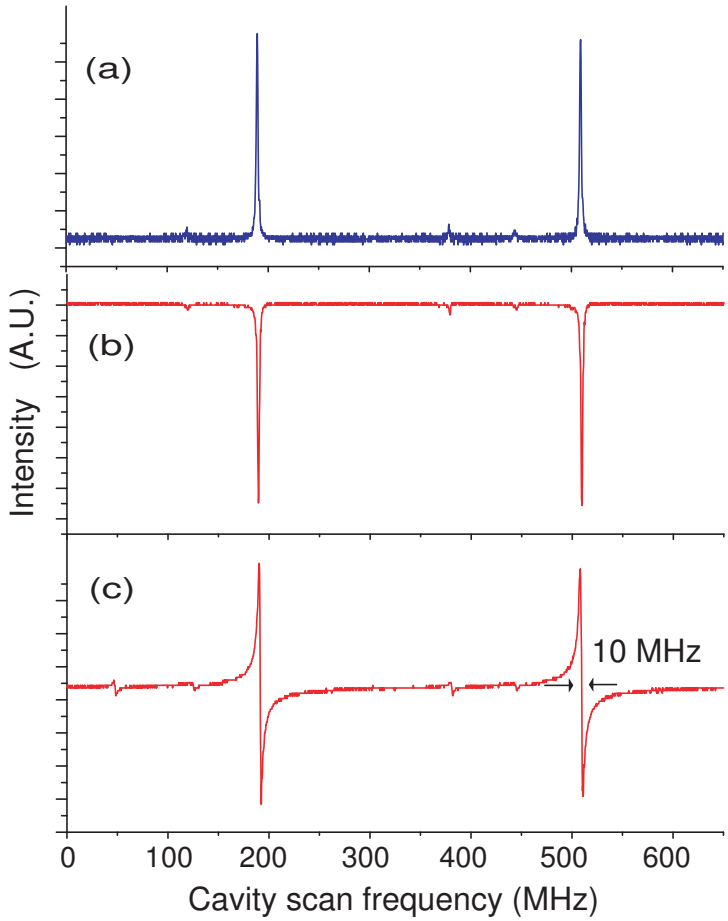

Figure 2.9: Experimental results for (a)Transmitted blue signal, (b)Reflected red signal from M_1, (c)Hänsch-Couillaud error signals

2.6.3 Electronic Stabilization

If the scan is turned off when the cavity is on resonance and the error signal is zero, respectively, any perturbation will make the error signal deviate from zero. To lock the cavity to the resonance position we use the feedback electronics shown in Figure 2.8. The Hänsch-Couillaud error signal can be applied to the PZT1 through a combination of integrator (I) and proportional gain control (P) by switching S2 and S3 ON/OFF. Usually, slow deviations (temperature drift) are controlled with the integrator whereas fast deviations (mechanical, electrical noise) are compensated for with proportional feedback. The reset switch S_R is used for re-locking the cavity to resonance when the PZT voltage of the error compensation approaches its limit value. In our doubling cavity, we can maximize the output power by adjusting the LBO crystal mount and the mirrors M_2, M_3 very carefully and slowly while the locking system is operating.

Chapter 3

Experimental Apparatus and Procedures

3.1 Introduction

Rydberg states of helium (^{4}He) atoms can be produced by successive excitation from the 1^1S_0 ground state. The energy levels relevant to our experiment are shown in Figure 3.1. With a lifetime of 8×10^3 s the first excited 2^3S_1 state can be considered as the effective metastable ground state (He*) on the time scale of atomic experiments. Its lifetime is mainly determined by the decay rate to the ground state via magnetic dipole transitions because electric dipole transitions are prohibited by the selection rules [46, 47]. Here the selection rules say that the electron spin cannot change and that the change in total orbital angular momentum has to be $\Delta L = \pm 1$.

The direct optical transition from the ground state to the metastable state is difficult due to a big internal energy of 19.8 eV, and thus He* atoms are created by a DC electric discharge in our experiment.

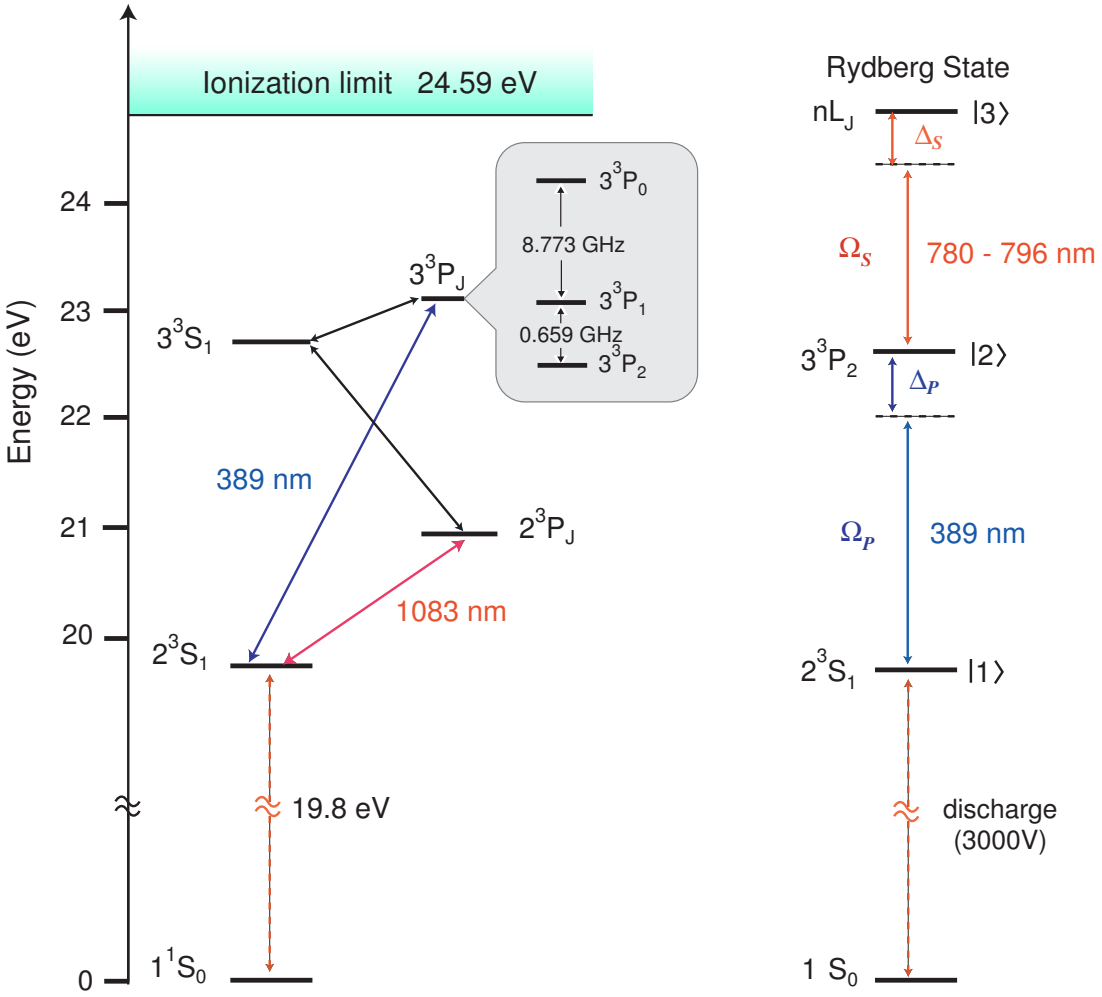

Figure 3.1: Energy level diagram for the triplet states of helium (left) and the transition scheme to the Rydberg states (right). Ω_P and Ω_S are the Rabi frequencies of the pump and Stokes lasers, respectively. Δ_P and Δ_S are their detunings

The transition from this effective ground state 2^3S_1 to a Rydberg state nL_J via the intermediate state 3^3P_2 is achieved by a two-step laser excitation at $\lambda = 389$ nm and $\lambda = 780 - 796$ nm, respectively. Once a beam of metastables is produced, the created He^* atoms should stay in the metastable state while passing through the interaction and the detection regions. However, it was experimentally observed that the loss of He^* atoms caused from collisions with the background gas is a severe problem when the pressure exceeds 10^{-5} Torr for more than a few cm along the beam path [48]. Thus, a vacuum system that guarantees a sufficiently long mean free path is required [38]. This chapter describes the production of our He^* beam, and both our vacuum and detection systems. Furthermore, the stabilization of the laser systems will be discussed.

3.2 Vacuum Systems

All experiments are performed in a beam apparatus consisting of three distinct vacuum chambers: a source chamber to produce He^* atoms, an interaction chamber to excite these metastables to Rydberg states with different laser beams, and a detection chamber to measure the spatial distribution of the helium atoms. The sketches of our vacuum system are shown in Figure 3.2.

The source chamber is a welded aluminum cube of 30 cm side length, while the interaction chamber is a similar cube with 25 cm sides. A skimmer and a slit separate these two chambers. To handle the gas flow from the source chamber to the detection chamber, a moderate size differential pumping system was

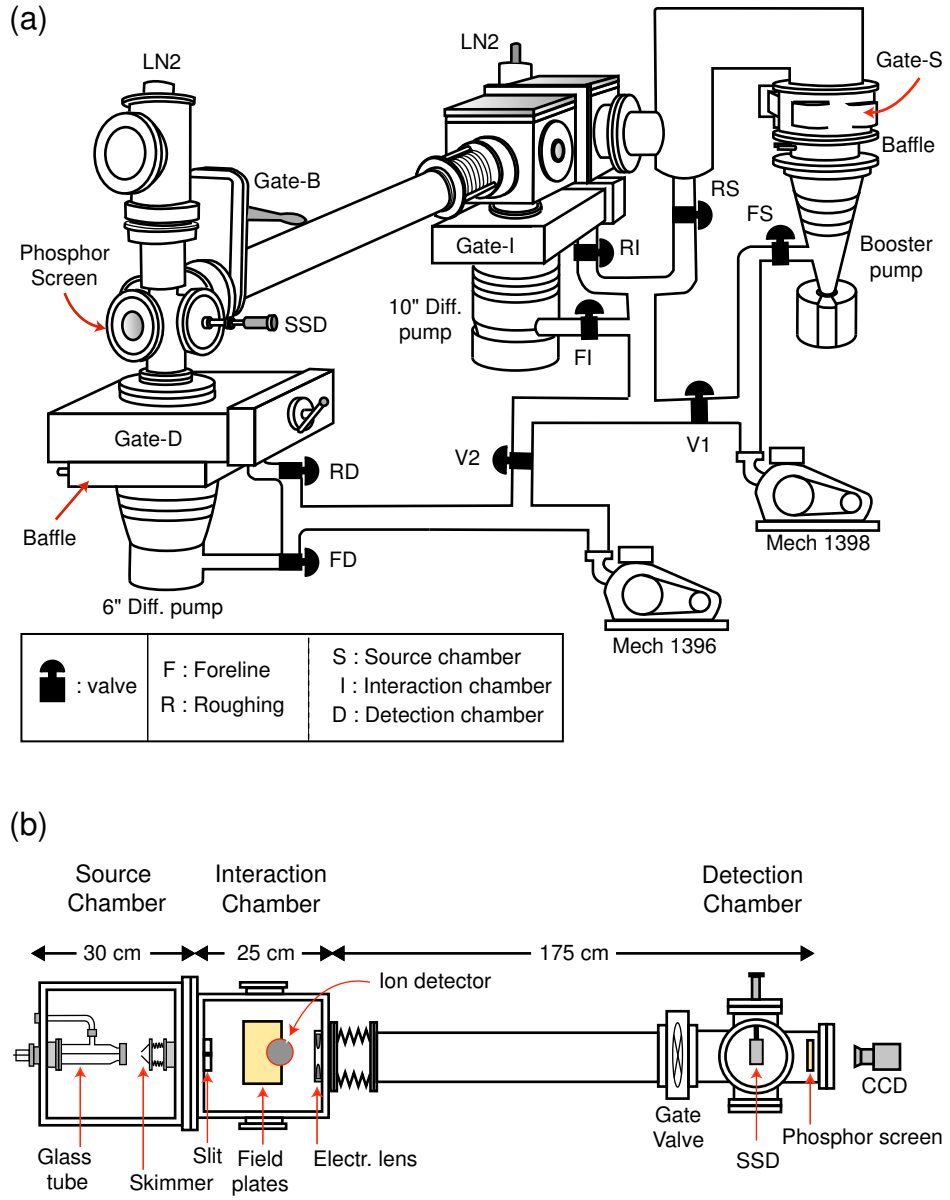

Figure 3.2: Vacuum system : (a) Three-dimensional drawing, (b) Top view

constructed using three diffusion pumps: an Edwards 9B3 booster pump with a pumping speed of 850 l/sec even at elevated pressure, a NRC/Varian HS-10 ten-inch diffusion pump (4200 l/sec), and a CVC/Bendix PBA-100A six-inch diffusion pump (1500 l/sec). Especially, the Booster pump is positioned in the source line because it operates efficiently at high flow rates and in the high-pressure range ($\sim 10^{-5}$ Torr). Two mechanical pumps back these three diffusion pumps: a Welch Duo-seal 1398 (1500 l/min) and a Welch Duo-seal 1396 (2800 l/sec). The vacuum chamber can be isolated from the diffusion pumps with gate valves: For the source and detection chambers CVC/VCSP-61B six-inch gate valves (**Gate-S** and **Gate-D** in Figure 3.2) are used, and a ten- inch gate valve (**Gate-I**, Model VRC 9457B-301) is used for the interaction chamber. In addition, there is a gate valve to isolate the interaction and the detection chambers.

In order to protect the vacuum chamber from oil contamination, the 6″ and the Booster pump are separated from the vacuum chamber by a water cooled baffle which condenses the oil vapor so it can drop back into the diffusion pump region. Cooling water is supplied to all the diffusion pumps and water baffles. The pressure in the three different vacuum chambers is monitored with ion gauges (Kurt J.Lesker G100K and G075K), and the foreline pressure is also measured with Veeco thermocouple gauges. A fail safe system operates and shuts off the diffusion pumps in one of the following cases: the foreline pressure exceeds 50 mTorr, the speed of the cooling water flow falls below the set point, or the temperature of the diffusion pump raises above the usual operation point.

The general procedure to achieve high vacuum in a system consisting of mechanical roughing pumps and diffusion pumps is well described in many vacuum books [49, 50, 51]. Usually, the diffusion pumps do not have to be turned off when the vacuum chamber is brought to air if the gate valve is closed. In Figure 3.2, for example, closing the gate valves **Gate-B**, **Gate-D**, and roughing valve **RD** isolates the detection chamber so that only the detection chamber can be vented to air while keeping all the diffusion pumps on.

To evacuate the chamber, after the vent valve (not shown in Figure 3.2) has been closed, the roughing valve **RD** is opened in order to first pump down the chamber with the mechanical pump. Once the pressure drops below 100 mTorr the roughing valve **RD** is closed and the gate valve **Gate-D** is opened. In experimental reality, any imperfection of the gate valve can cause undesired airflow through a gap in the gate valve. Thus we turn off the diffusion pump and have it cool down ($\sim$ 3 hours) whenever we open the vacuum chamber. In addition, all the roughing valves (**RS**, **RI**, **RD**) are closed during operation. Source and interaction chamber are always brought to air together because they are connected through a skimmer.

The procedure to vent the chambers is the following: First, both chambers are isolated from the detection chamber by closing the gate valve **Gate-B**, and both the booster pump and the 10″-diffusion pump are turned off and allowed to cool down for about 3 hours. Second, closing the valves **FS**, **V1**, and **V2** (**FI**: always open) ensures isolation from both mechanical pumps and the detection vacuum loop. Third, the chambers are vented to air. In order

to pump down again, after closing the vent valve, **FS** and **V1** are opened simultaneously but slowly in order to prevent a sudden change of pressure which can cause serious damage to the glass tube in the source chamber. When the foreline pressure reaches 100 mTorr, the diffusion pumps can be turned on. After the pressure in the interaction chamber falls below 10^{-5} Torr, the gate valve **Gate-B** can be opened so that the system is also pumped down through the detection loop. The achieved pressures in our system are 10^{-5} Torr, 2×10^{-6} Torr, and 8×10^{-7} Torr for the source, interaction, and detection chambers, respectively.

3.2.1 Metastable Helium Source

The source chamber contains a Pyrex glass tube and a skimmer, as shown in Figure 3.3. The design of our helium source is based on that of Fahey *et al.* [52]. As shown in Figure 3.3, helium gas is guided from the He tank into a Pyrex glass tube inside the source chamber through plastic tubing. The inlet pressure of the helium flow into the glass tube is about 50 Torr. Both sides of the glass tube are sealed (applying Aremco Inc. Ceramabond 503) with pieces machined out of a rod (diameter $1''$) of boron-nitride (BN), which combines poor electrical conductivity with good thermal conductivity. There is a small size nozzle (diameter 150 μm, length 1 mm) in the front side BN seal which is cooled by liquid nitrogen in order to reduce the initial transverse velocity spread of the helium atoms flowing through the nozzle by about a factor of two as compared to the water-cooled case [53].

A thin glass tube (diameter 5 mm) is fed through the back side seal so that

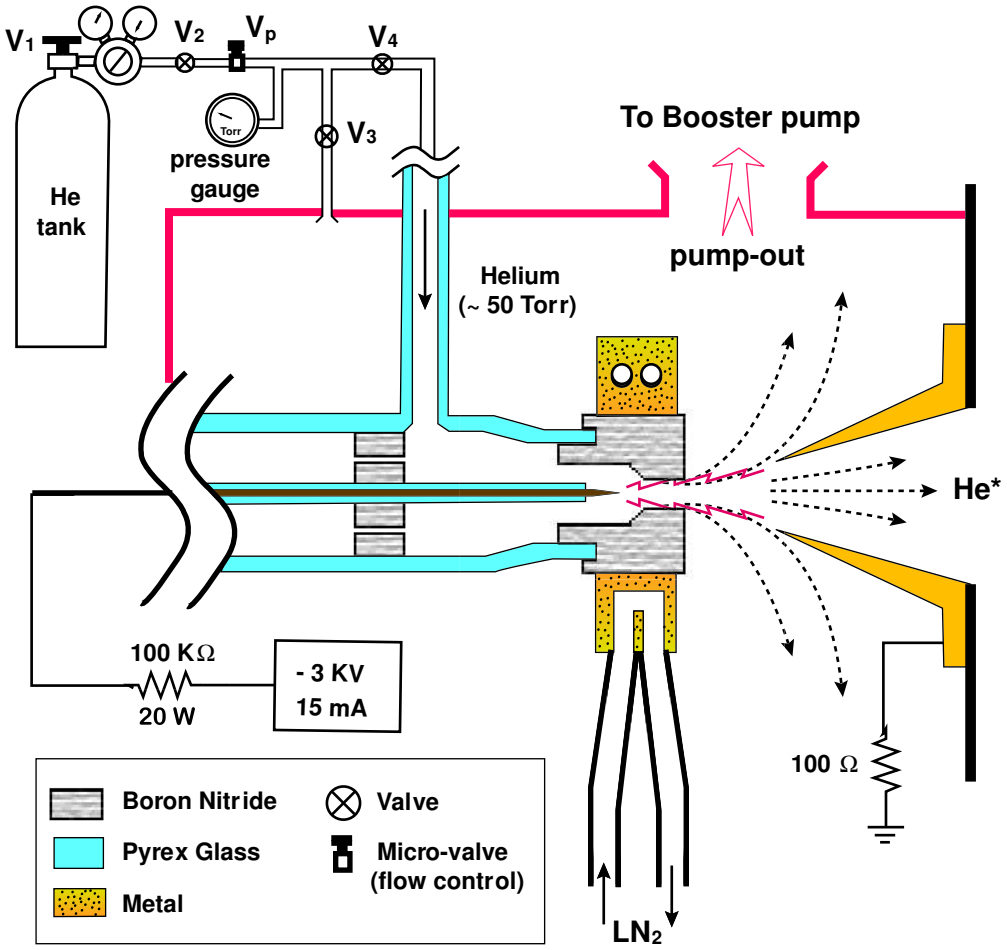

Figure 3.3: Metastable Helium source

a tungsten needle can be positioned along the axis of the glass tube such that the tip of the needle is located close ($\sim$ 1 mm) to the nozzle. Approximately $1 \sim 2$ cm downstream from the nozzle, there is a skimmer which is connected to the wall separating the source chamber from the interaction chamber with a bellows. The skimmer has a 1 mm hole and is mounted on a stage that is adjustable in three dimensions.

The ignition procedure of the discharge is started by allowing helium gas

into the glass tube by opening the valves $\mathbf{V}_2$ and $\mathbf{V}_1$. Valve $\mathbf{V}_2$ should always be opened ahead of valve $\mathbf{V}_1$ in order to protect the He tank from contamination. By adjusting the micro-valve $\mathbf{V}_p$ the flow of helium is set to around $50 \sim 70$ Torr on the pressure gauge. A pressure above 200 Torr can cause serious damage to the glass tube. Thus, it is recommended to close both valve $\mathbf{V}_3$ and $\mathbf{V}_4$ before the pressure gauge shows a safe value below 200 Torr. Once that is the case, the micro-valve $\mathbf{V}_p$ is adjusted further until the inlet pressure reaches an adequate value. Now, valve $\mathbf{V}_4$ can be opened. The purpose of the valve $\mathbf{V}_3$ is to get rid of the gas in the plastic tube region (He tank $\sim$ glass tube) quickly through the source chamber rather than through the nozzle of the glass tube. Therefore, valve $\mathbf{V}_3$ should always be closed except when pumping out the gas from the plastic tubing.

In practice, it takes about 10 min until the helium flow is stabilized in the system. After helium gas is supplied into the glass tube through valve $\mathbf{V}_4$, the pressure difference between the inside ($\sim$ 50 Torr) and the outside ($\sim 10^{-5}$ Torr) of the glass tube produces a supersonic expansion of the helium gas through the boron-nitride nozzle. Now a voltage of (-3 kV) is applied to the tungsten needle. The voltage difference between the needle and the skimmer, which is at ground potential, creates an electric field. Usually, the DC discharge starts. The discharge current can be varied up to (20 mA) on the power supply. If a higher current is applied, the ballast resistor (100 kΩ, 20 W, Model No. OHMITE B20J100K) that is used to ensure stable operation can be burned. The higher the current, the faster is the velocity of the He atoms in the beam [53]. The optimum current can be found by maximizing the

source efficiency on the detectors (ion signal or phosphor screen), it is around $8 \sim 10$ mA in our source.

Sometimes the discharge does not come out through the nozzle and stays inside the glass tube. This usually happens if the pressure inside the glass tube is too low. In order to solve this problem, the inlet pressure can be slightly increased by adjusting the micro-valve $\mathbf{V}_p$ (up to $\sim$ 100 Torr). Once the discharge comes out, the inlet pressure has to be reduced ($\sim$ 50 Torr) because the metastable He atoms get quenched in higher pressure.

If the discharge still does not run, several things should be checked: First, if the back-up pressure of the booster pump decreases because there is no gas flow from the source chamber through the nozzle one can suspect that the nozzle is blocked. In this case, the inlet pressure would also be higher than usual. Second, the ballast resistor could have been burned. As long as the resistor works, one can see the discharge glow inside the glass tube if the inlet pressure is decreased ($<$ 50 Torr). In general, keeping the nozzle and the needle clean will ensure better running of the discharge. In addition, the position of the skimmer can be optimized by aligning the skimmer stage and maximizing the brightness of the atomic beam on the phosphor screen. Under steady running conditions, the source produced 10^{14} metastables/sec/sr [54].

Longitudinal Velocity Distribution

A time of flight (TOF) measurement was done by Mary.J.Bellanca [54] using a chopper inside the vacuum system. A He-Ne laser beam hit a photodiode located just behind the chopper wheel and thus generated a trigger signal for

the TOF measurement. The detector was positioned about (2 m) downstream from the nozzle of the glass tube. The current signal from the Keithley 486 Pico-ammeter was converted to a voltage signal with a 100 kΩ resistor, and then subsequently amplified by a SR560 Low-Noise Pre-Amplifier. The signal shown in Figure 3.4 was taken with a Tek210 Digital Oscilloscope. The average longitudinal velocity and the spread Δv were calculated from a Gaussian fit (dotted line). The first peak is created by UV-photons. Its area is about 35% of the second peak, which is generated by metastable helium atoms. It was observed that a higher inlet pressure increases the area of the first peak and the amount of UV-photons, respectively.

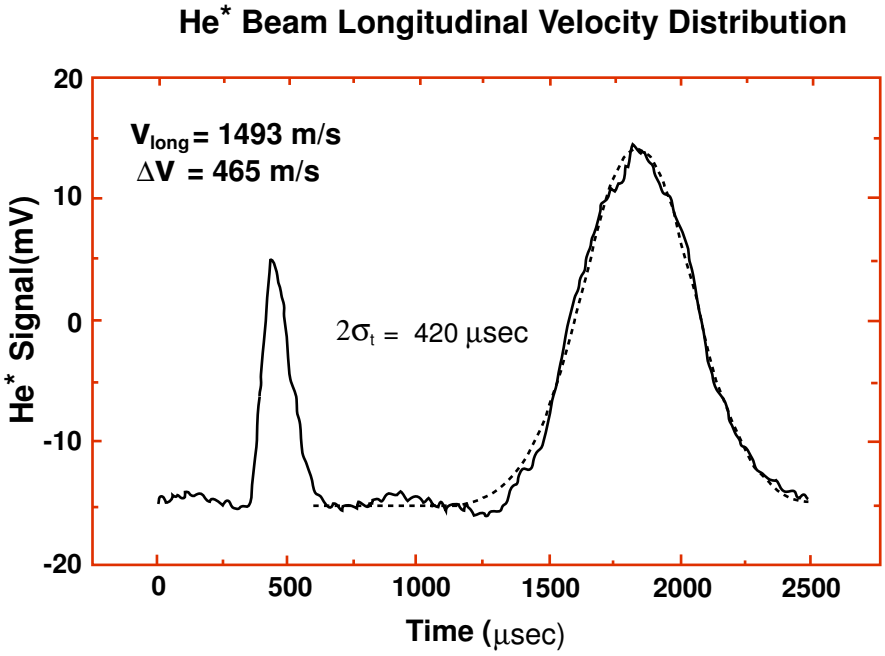

Figure 3.4: Time-of-flight velocity distribution. [54]

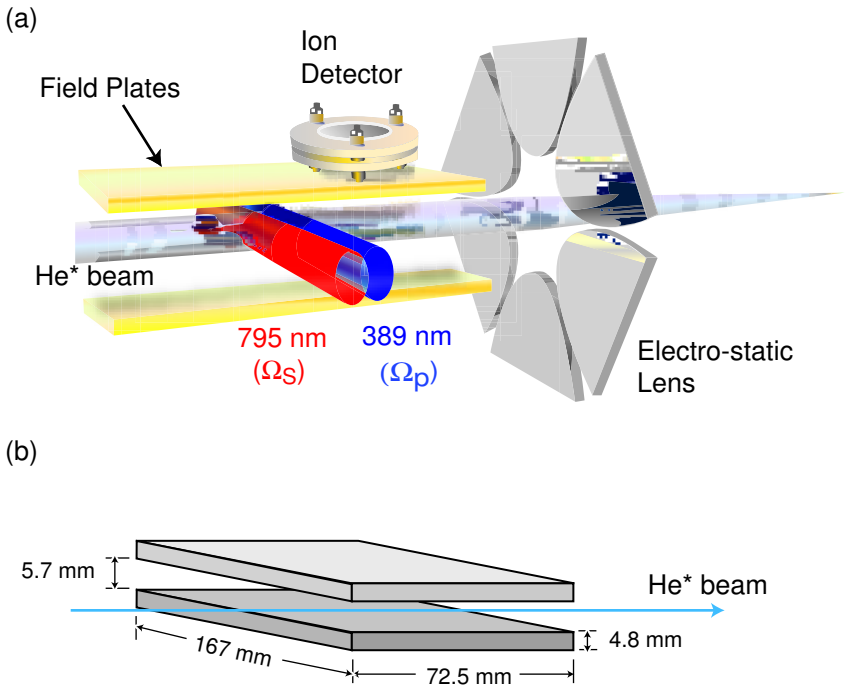

Figure 3.5: Experimental configuration of the interaction chamber: (a) Three-dimensional drawing, (b) Dimensions of field plates

3.2.2 Interaction Chamber

The interaction chamber contains two field plates, an ion detector, and an electrostatic lens which is located ($\sim$ 4 cm) downstream from the plates (Figure 3.5). In addition, a slit is placed ($\sim$ 5 cm) up-stream from the field plates (not shown in Figure 3.5, see Figure 3.2(b)). Its position along the transverse direction can be altered from outside the vacuum chamber with a flexible feed-through.

Both sides of the interaction chamber contain a window, each with a diameter of 2 inches, so that our exciting laser beams can traverse the atomic beam

orthogonally. The windows are anti-reflection coated for both 389 and 795 nm to minimize intensity losses. A number of BNC connectors are embedded in the vacuum blank-offs of the interaction chamber for supplying voltages to the electrostatic lens, the upper- and lower- field plates, and the MCPs (micro-channel plates) of the ion detector. The anode of the ion detector is also connected to a scope with a BNC cable. Details about our ion detector will be discussed in the next section.

3.2.3 Detection Systems

In order to observe the ion signal produced by the Rydberg atoms and the spatial distribution of the atomic beam we employ three different detection systems: an ion detector, a phosphor screen detector, and a stainless steel detector. All detectors are based on the combination of MCPs with an anode or a phosphor screen. MCPs are thin discs of lead glass which contain many tube-shaped channels that serve as multiplier tubes. The MCP we use (BURLE Model MCP 25/12/12 D 40:1) has a maximum electron multiplication factor of 4×10^3 for the maximum bias voltage (1000 V).

Ion Detector

Atoms that were excited to the Rydberg state can be ionized when colliding with the background gas in the vacuum chamber. The produced ions will be attracted towards the MCP because the front side of the MCP is at a potential of -2000 V as shown in Figure 3.6(a). When the ions hit the MCP, an electron shower is created. These electrons get accelerated to the second MCP by the

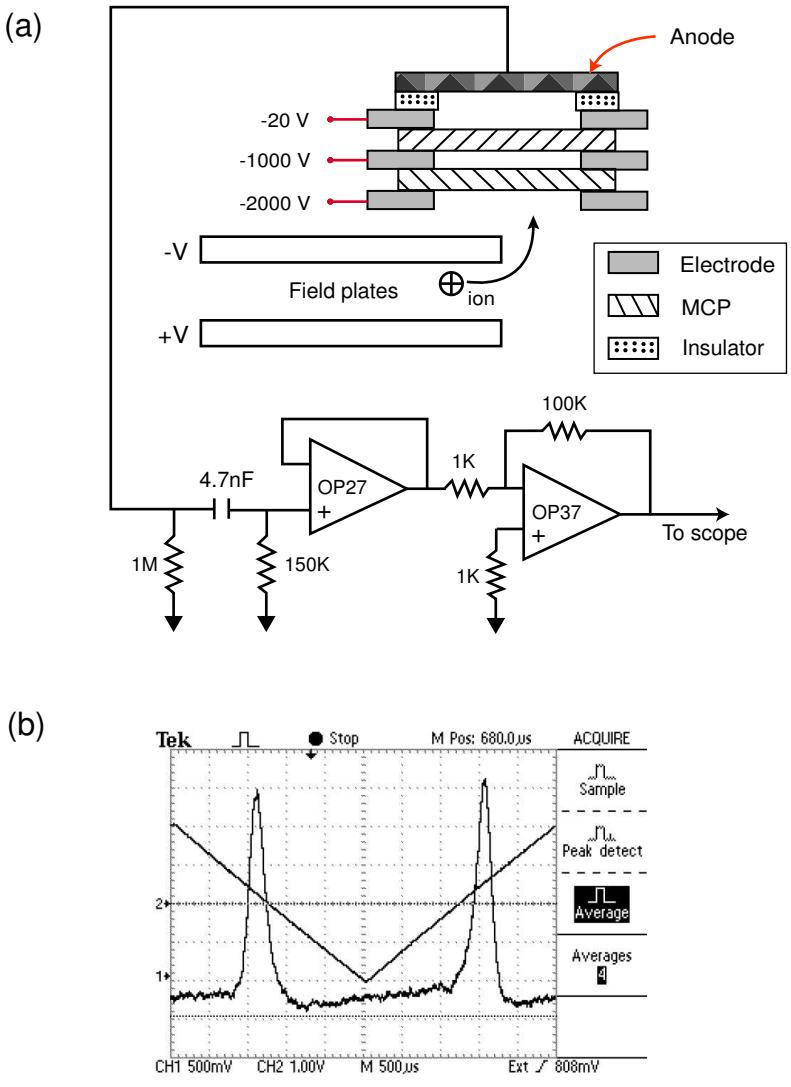

Figure 3.6: a) Ion detector with amplification circuit, (b) Ion signal: lower field plate scan - 5 V, upper-field (−10 V), Rydberg state - 26S, Electric field - 30 V/cm

potential difference, and the amplification process repeats. The MCP pair in our system has a combined gain of $\sim 10^6$. An anode collects the electrons produced by the second MCP so that a current can be measured in the circuit. Subsequently, the current signal passes through an amplification circuit and is converted to a voltage signal. The voltage signal which is proportional to the number of produced ions can be observed with an oscilloscope (Tektronix, Model TDK210) if the atomic transition to the Rydberg state is on resonance during the scan of the electric field. The signal shown in Figure 3.6(b) was observed for the transition to the 26S Stark level at an electric field of 30 V/cm while scanning the lower field plate.

Phosphor Screen Detector (PSD)

The PSD provides us with a real time image of the spatial distribution of He^* atoms because the intensity of the fluorescence of the screen is related to the flux of the atoms. A CCD camera (Dage-MTI CCD100) is used to monitor the phosphor screen through a flanged window (Figure 3.7). The PSD thus enables us to optimize our alignment: We can observe the beam height and direction, we can maximize the atomic beam flux by adjusting the skimmer, and we can set the 389 nm laser frequency because the radiative pushing effect can only be observed if the frequency scans the correct transition. However, the sensitivity of the PSD to the atomic flux is non-linear and non-uniform (measured in Ref.[21]) because the areas that are exposed to a higher flux age faster. We can even observe completely burned spots in the more frequently exposed area of the surface of the phosphor screen (Model P20).

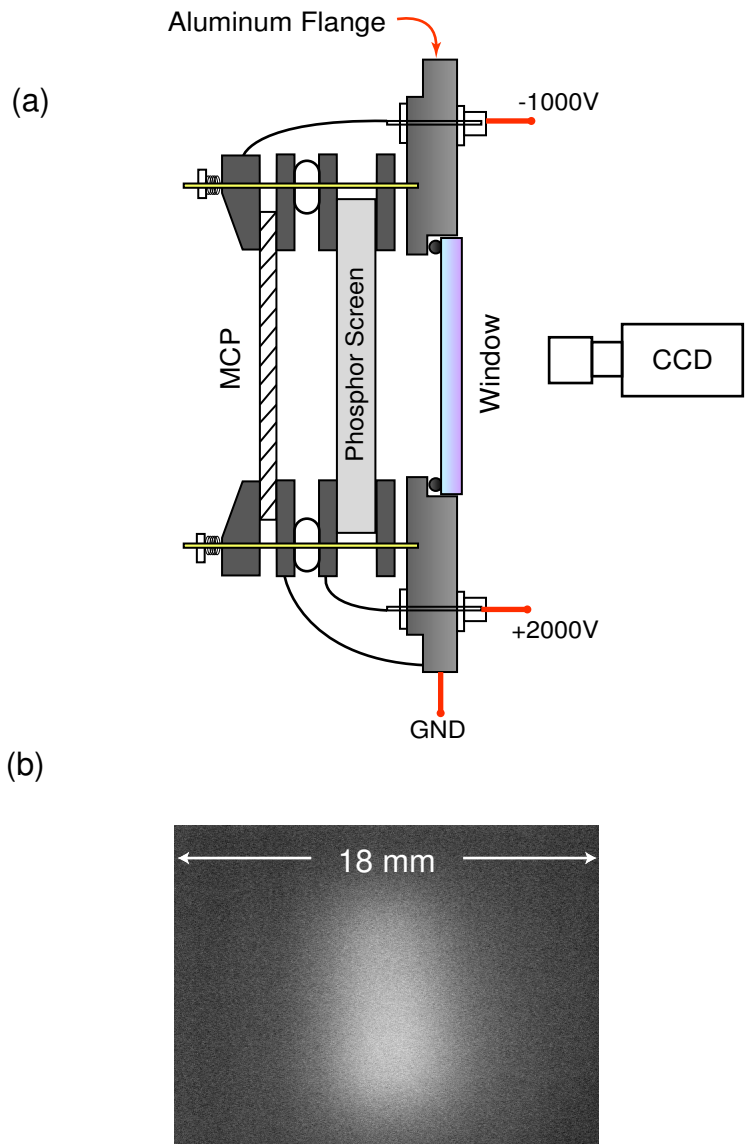

Figure 3.7: (a) Phosphor Screen Detector (PSD) for detection of spatial distribution of atomic beam detection, (b) Typical image from CCD at Phosphor (1700 V), MCP (−900 V), Inlet pressure (50 Torr)

Stainless Steel Detector (SSD)

To obtain an absolute measurement of the atomic beam profile, a stainless steel detector is a better choice. A top view of our SSD detector and a typical signal created by our He^* beam are shown in Figure 3.8. After passing trough the slit ($\sim$ 300 μm), the He^* atoms strike the stainless steel plate where electrons can be liberated with an efficiency of 70% of [56], because the energy of the metastable atoms ($\sim 20\ eV$) is larger than the work function of the metal ($4.7 \sim 5.6$ eV) [55]. By contrast, the kinetic energy (0.05 eV at 1600 m/s) of the ground state atoms is too low to overcome the work function of the metal. Once the electrons are liberated they are accelerated towards the MCP by the potential difference between the stainless steel plate and the MCP. A Keithley Model 486 picoammeter measures the electron current at the anode. The slit position can be altered with a linear motion vacuum feedthrough (Huntington Mechanical Laboratories, Inc. 2 inch feedthrough, Model L-2111-2), so that a position dependent current signal can be measured. Thus, an accurate transverse beam profile can be recorded because the current is proportional to the flux of the He^* atoms. Figure 3.8(b) shows such a profile.

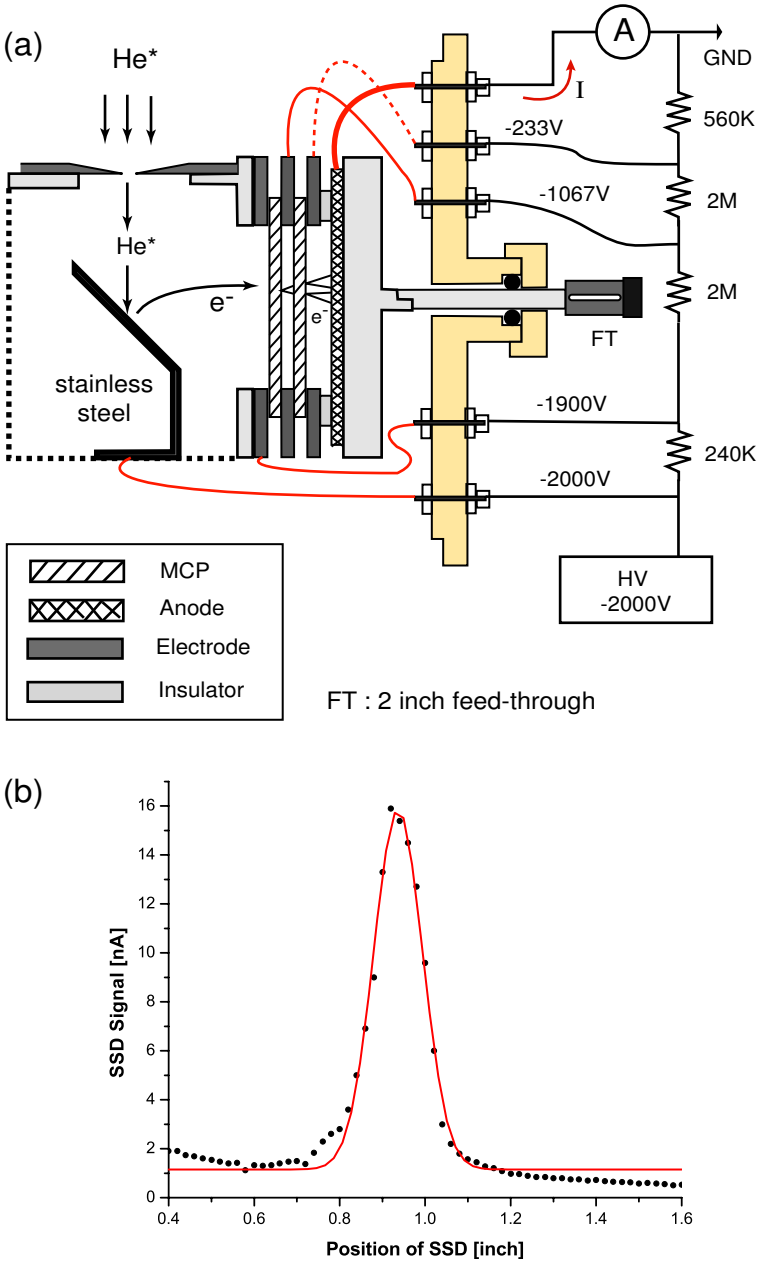

Figure 3.8: (a) Stainless Steel + MCP Detector(SSD), (b) Current signal measured by a Keithley Model 486 pico-ammeter

3.3 The Laser Systems

Figure 3.1 shows the relevant transitions for the production of Rydberg atoms. Two independent Ti:Sapphire laser systems provide the light for the pump (λ = 389 nm) and the Stokes ($\lambda 785 - 815$ nm) beam. The 389 nm light is generated by frequency doubling the output of a Schwartz Electro-Optics (SEO) Ti:Sapphire laser, which is pumped by a diode-pumped, frequency doubled Nd:YVO_4 laser (Coherent Model Verdi V10) with up to 10.5 W output power at 532 nm. The red light is provided from a TekhnoScan Ti:Sapphire laser (Model TIS-SF-07e) which is pumped by an Argon-Ion laser (Coherent Model Innova 300). To stabilize the laser frequencies, three different kinds of locking system are used: the Pound-Drever-Hall technique [57], the Hänsch-Couillaud technique [45], and Saturation Absorption Spectroscopy (SAS) [58, 73].

3.3.1 Blue ($\lambda = 389$ nm) Laser System

The schematics of the blue laser system are presented in Figure 3.9 and Figure 3.10. A ring configuration is chosen in order to avoid the spatial hole burning effect. In a standing wave geometry, spatial hole burning results in power losses because the molecules in the active region do not contribute to the build-up of the laser field if they are positioned in the nodes of the standing wave. In order to enforce uni-directional operation, an optical diode was placed (**OD** in Figure 3.9) in the ring cavity. In addition, stable single-frequency operation is obtained by using several mode selective elements, namely a bire-

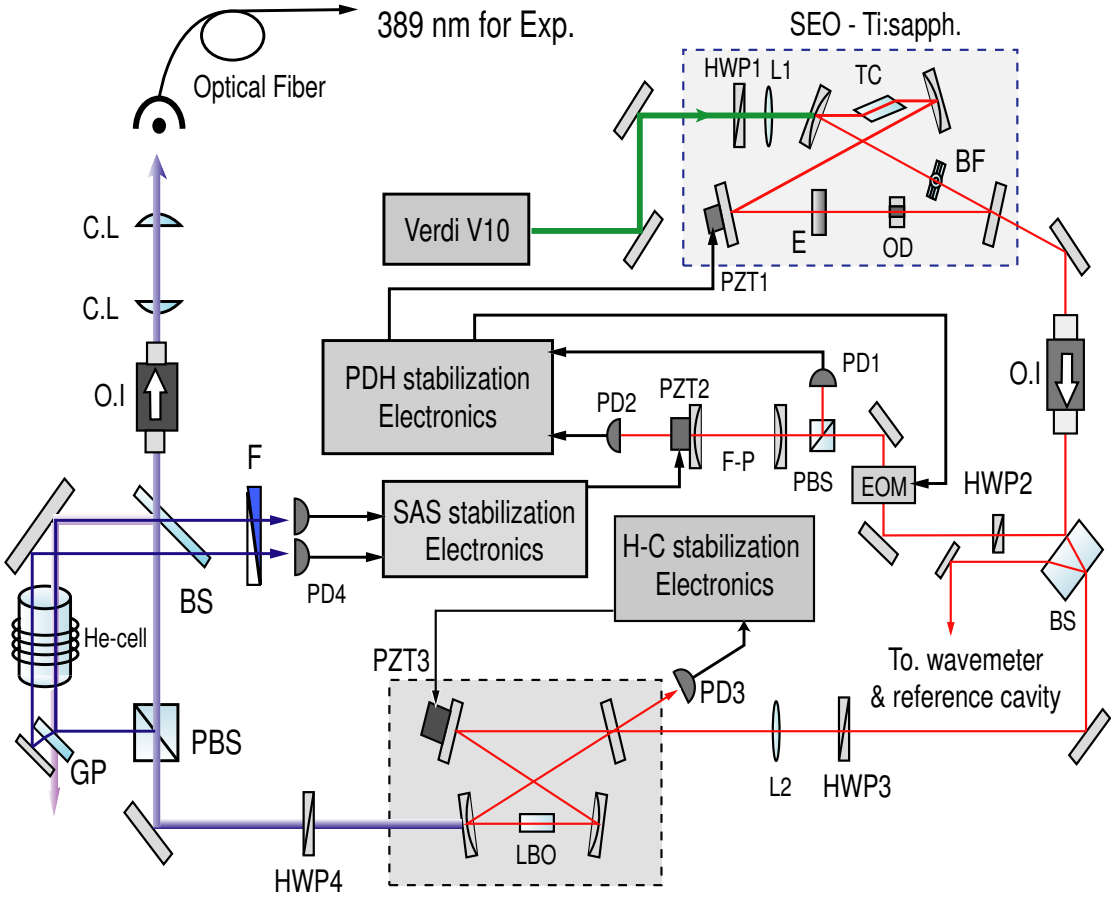

CL : Cylindrical lens O.I : Optical Isolator BS : Beam splitter F : Density Filter
PBS : Polarization beam splitter GP : Glass plate PZT : Piezo-electric transducer
PD : Photo diode detector F-P : Fabry-Perot cavity HWP : Half-wave plate
OD : Optical diode TC : Ti-sapphire crystal BF : Birefringent filter
EOM : Electro-optic modulator SAS : Saturation absorption spectroscopy
PDH : Pound-Drever-Hall H-C : Hansch-Couillaud L : Lens E : Etalon

Figure 3.9: Optical scheme of the blue laser system

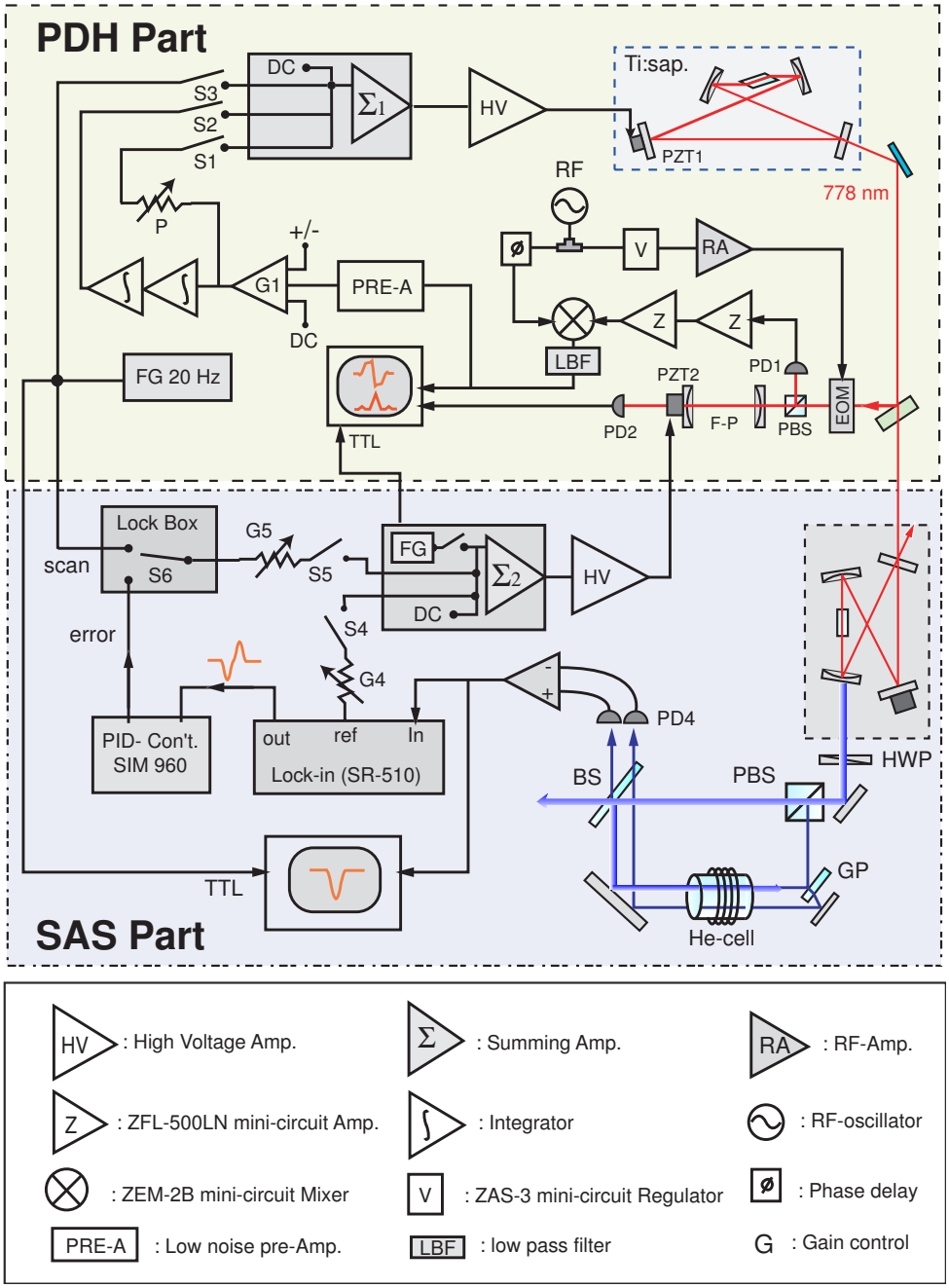

Figure 3.10: Stabilization electronics for the blue laser system.(Hänsch-Couillaud part in Section 2.6.1 and 2.6.2)

fringent filter and an etalon. In our laser system, one can tune the etalon (**E**) to change the wavelength in a relatively small range ($10^{-4} \sim 10^{-5}$ nm). At a wavelength of 778 nm, a change of 10^{-3} nm corresponds to roughly 500 MHz in frequency. If a larger amount of adjustment is required the birefringent filter can be tuned. When all elements are properly aligned the output power of our laser reaches up to 3.1 W in single mode operation at 777.8 nm.

The locking system to stabilize the laser frequency consists of three main parts. In this section, the stabilization electronics for Pound-Drever-Hall (PDH) and Saturation Absorption Spectroscopy (SAS) are explained. Hänsch-Couillaud method is presented in Section 2.6.1 and 2.6.2.

Pound-Drever-Hall Locking

The SEO Ti:Sapphire laser is first stabilized employing the Pound-Drever-Hall locking scheme [57]. Therefore, a part of the main laser beam is split off with a beam splitter and further divided into three beams. One goes to a wavemeter that allows to coarsely monitor the frequency of the laser, one is sent to a reference Fabry-Perot cavity to monitor the mode structure of the laser, and the third is used to generate the Pound-Drever-Hall error signal as follows: An electro-optical modulator (**EOM**) modulates the phase of the central carrier frequency ω_c of the laser with the frequency Ω (= 64 MHz) and produces two sidebands at $\omega_c \pm \Omega$. The radio frequency (= 64 MHz) is supplied to the **EOM** from the oscillator (**RF**) via an RF-amplifier (**RA**) [Figure 3.10].

The modulated beam is then incident on the Fabry-Perot (**FP**) cavity. Two photodetectors detectors (fast Si PIN photodetector, **PD1** and **PD2**)

are used to measure both the transmission through the FP cavity and the reflection from the cavity. The reflected signal from **PD1** passes through an RF amplifier (Mini-Circuits ZFL500LN) and is compared to the RF input at 64 MHz in a mixer (Mini-circuits ZEM2B) which serves as a phase detector. When the carrier frequency is resonant to one of the **FP** cavity modes, there is no reflection at the carrier frequency and the phase-modulated sidebands have equally reflected amplitudes but opposite phases. Thus, the two sidebands interfere destructively and the signal on **PD1** will be zero.

When the carrier frequency is slightly detuned from cavity resonance, the amplitude of the reflected beam depends on where the resonance is. The two sidebands experience a different amount of reflection so that the beating signal on **PD1** will be non-zero even if their phases are still opposite. The **PD1** signal is measured with a phase sensitive lock-in detection system consisting of amplifier, mixer, reference signal, phase shifter, and integrator or low pass filter. Lock-in detection is used to measure both magnitude and phase of the signal by extracting only the part that is at the same frequency as the reference frequency out of the noise. The output of the mixer that multiplies the sinusoidal **PD1** signal with the sinusoidal reference signal of frequency Ω, is a signal that contains two frequencies: the sum and the difference of the two multiplied frequencies of the signals. There can be a phase difference between the **PD1** signal and the reference signal because of the response characteristics of the EOM and the cavity.

The phase shifter compensates for this phase difference. If the two incoming frequencies are exactly the same, the mixer produces both a DC (zero-

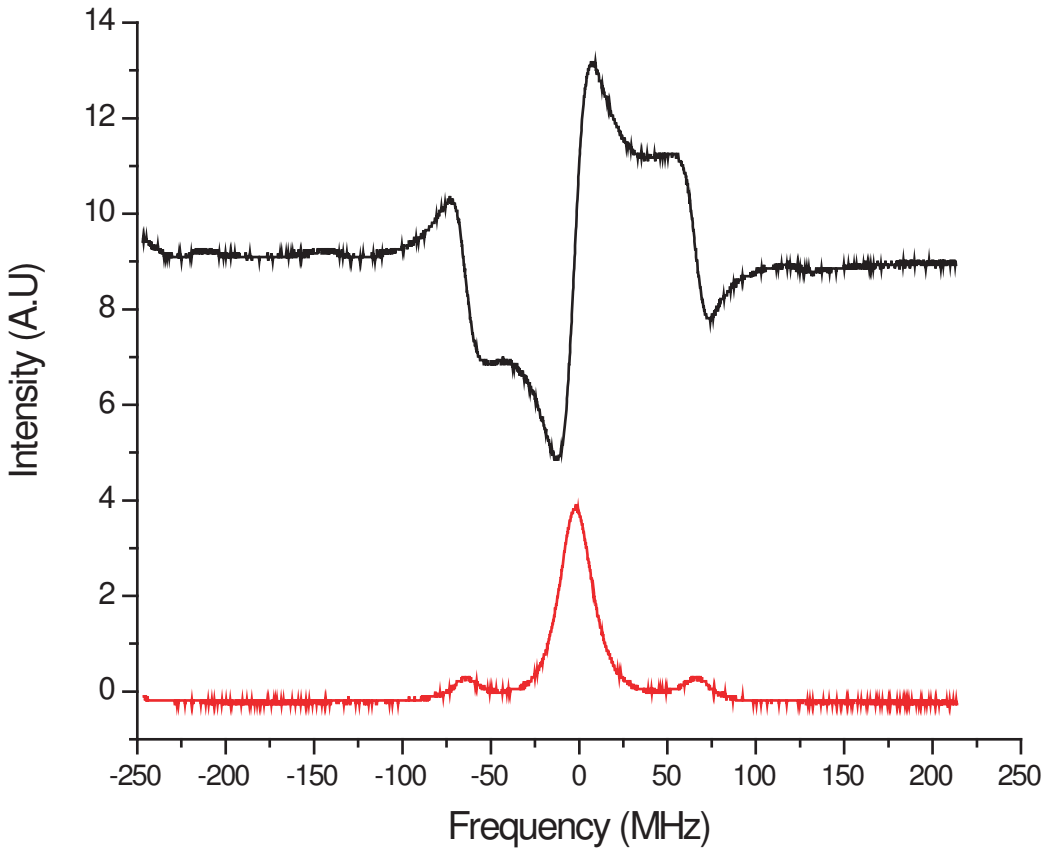

Figure 3.11: Pound-Drever-Hall (PDH) signals: error signal (top) and transmission signal (bottom)

frequency) and an AC (2Ω-frequency) output. An integrator or low-pass filter will only let the DC-component pass which is then used as an error signal for the feedback loop. Both error and transmission signal are shown in Figure 3.11. The error signal is fed to a low-noise amplifier, and the gain and cut-off frequency are optimized. After choosing the correct polarity (+/−) and DC-offset, the error signal is separately sent through a two stage (f_{3dB} = 2 Hz and 0.5 Hz) integral and a proportional loop and afterwards recombined in

a summing junction. The output of the summing junction is amplified with a high voltage amplifier and applied to **PZT1** [in Figures 3.9 and 3.10] in order to adjust the laser cavity length back to resonance with the small mirror attached to **PZT1**.

Saturation Absorption Spectroscopy (SAS)

While the laser frequency can be stabilized on a short time scale when locked to a Fabry-Perot cavity, a small and comparably slow temperature drift can change the cavity length without any compensation. Therefore the FP cavity should also be locked to a stable reference in order to achieve long-term stability. Since we want to drive the transition $2^3S_1 \rightarrow 3^3P_2$ at $\lambda = 389$ nm with the beam produced by second harmonic generation (see Chapter 2) the best reference is this transition itself. Employing the saturation absorption spectroscopy (SAS) technique, we thus lock the PDH cavity to the atomic transition. Therefore, a polarization beam splitter cube (**PBS**) is used to take a small part of the output of the frequency-doubling cavity for the SAS setup.

The beam is split into two weak beams (probe and reference) and a strong counterpropagating pump beam that overlaps with the probe beam in the He-cell. The strong pump beam saturates the transition $2^3S_1 \rightarrow 3^3P_2$ at $\lambda = 389$ nm so that the pump beam is weakly absorbed resulting in a sharp dip (called *Lamb dip*) in the Doppler absorption profile. In our SAS setup, the saturation parameter of the pump beam is $s \sim 10$ ($s = I/I_s,\ I_s = 3.31$ mW/cm^2, [2]), while that for the probe beam is $s \sim 1$. The balance of the intensities of the probe and the reference beams at the photodiode detector (**PD4**) is adjusted

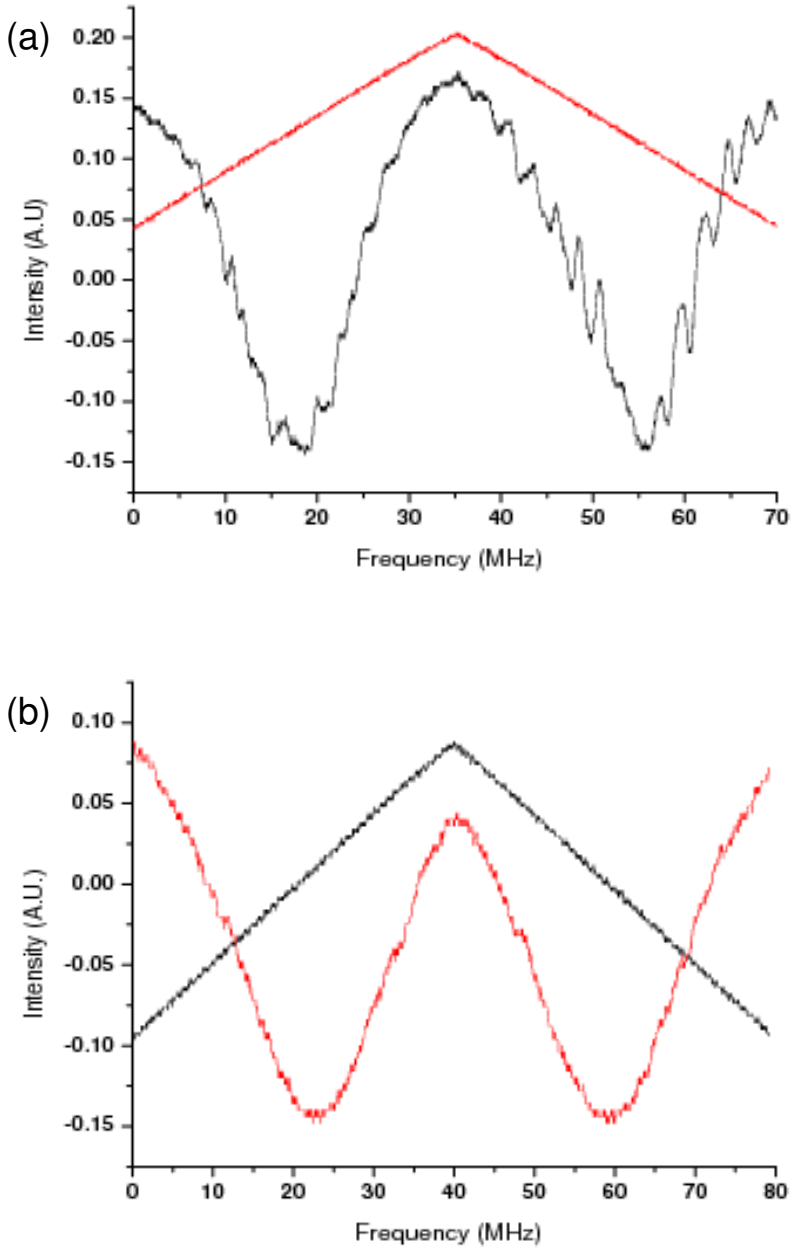

Figure 3.12: Saturated absorption spectroscopy (SAS) signals for $2^3S_1 \rightarrow 3^3P_2$ transition at $\lambda = 389$ nm. (a) without locking the laser to the PDH error signal, (b) with locking the laser to the PDH error signal

with a variable filter (**F**) as represented in Figure 3.9. The half-waveplate (**HWP4** in Figure 3.9) can be used to adjust the intensities of the pump and the probe beams. An optical isolator was positioned right after the SAS setup to avoid feedback to the SAS setup.

In order to produce the error signal, the absorption signal from **PD4** is fed to a lock-in amplifier (SRS Model SR510) and modulated by a 1 kHz reference signal. This reference signal also modulates the PDH cavity through the summing box Σ_2 when the switch **S4** is closed. The mechanism to generate the DC error signal with the lock-in detection has already been explained in the section on the generation of the PDH error signal. The absorption and the error signal are shown in Figure 3.13(b). The error signal was taken at a slow scan rate ($\leq$ 1Hz). After aligning the SAS setup we need to find the correct transition peaks.

Locking the blue laser to the correct transition

The first step to move the laser frequency to the correct transition is to tune the birefringent filter (**BF**) and the etalon (**E**) [see Figure 3.9]. If the frequency is tuned to the correct value, the fluorescence in the RF-discharged He-cell can be observed. In our system, we used to observe the fluorescence at the values (777.9505 - 777.9515 nm) with the wavemeter (WA-1500). In order to find the absorption peak, the laser cavity is scanned with the function generator (20 Hz) by closing the switch **S3** and adjusting the DC-offset (Figure 3.10). Once the absorption signal appears as shown in Figure 3.12(a), the cavity has to be tuned towards the higher wavelength side until one cannot see another

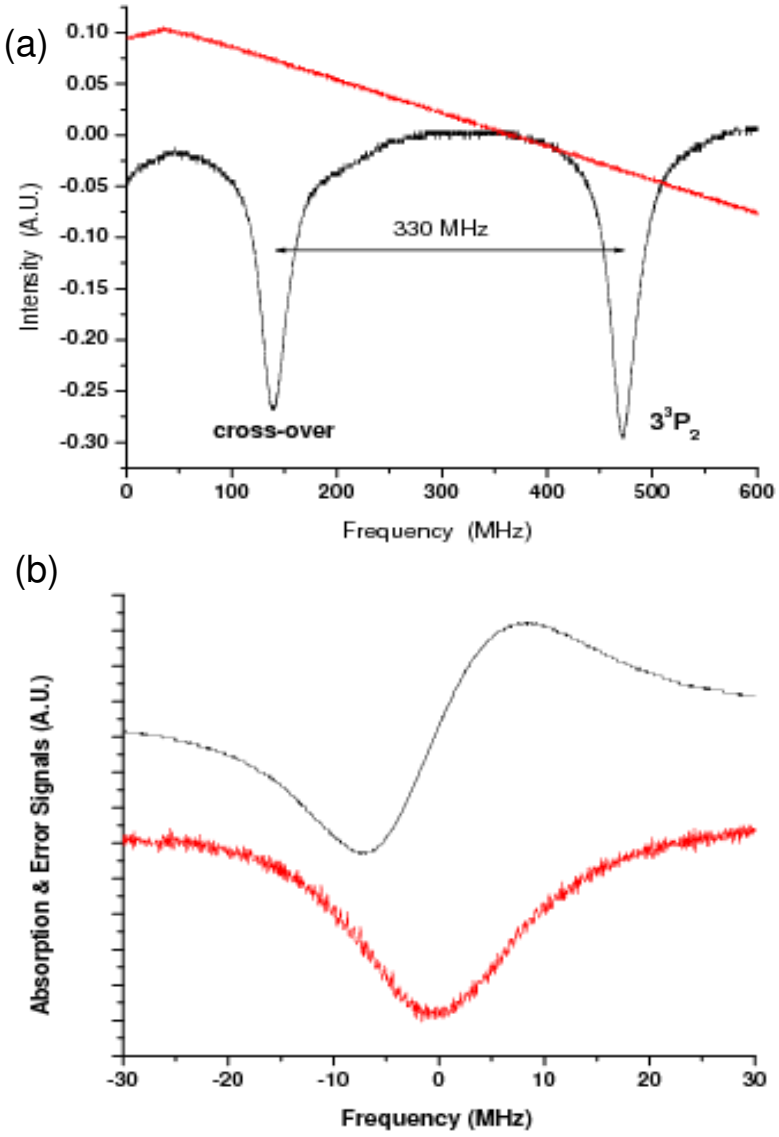

Figure 3.13: SAS signals for (a) $2^3S_1 \rightarrow 3^3P_2$ transition and crossover between 3^3P_2 and 3^3P_1 (b)$2^3S_1 \rightarrow 3^3P_2$ transition and error signal

absorption signal when further increasing the wavelength. This is the case because the frequency of the correct transition ($2^3S_1 \rightarrow 3^3P_2$) is the lowest frequency among all transitions ($2^3S_1 \rightarrow 3^3P_J$, J = 0,1,2) as shown in Figure 3.1. This procedure should be done without locking the laser to the PDH cavity, but with the frequency-doubling cavity locked. If the doubling cavity unlocks while the laser cavity is scanned, it can be relocked with the reset switch of the integrator.

The next step of the whole locking procedure is to lock the laser cavity to the PDH cavity as follows: First, the switch **S3** is opened after observing the peak shown in Figure 3.12(a). The laser cavity will stay close to the correct transition peak. Second, the scan of the PDH cavity is turned off by switching off the internal function generator in the summing box Σ_2 (Figure 3.10). Third, the switches **S1** and **S2** are closed and the gain of the two-stage integrator is adjusted simultaneously until the transmission signal from **PD2** jumps up to the former height of the transmission peaks on the scope screen. Subsequently, the locking must be optimized in order to minimize the laser line-width by minimizing the deviation of the locking signal from the resonance position (zero). This is done by optimizing the integral and proportional gains.

After the laser cavity has been locked to the PDH cavity, the next step is to lock the PDH cavity to the atomic transition, namely the SAS. The laser frequency should already be very close to the correct transition. Switch **S6** (Figure 3.10) is set to scan and switch **S5** is closed, then the DC-offset of the summing box Σ_2 is changed until the absorption signal shown in Figure

3.12(b) can be observed again. If the gain **G5** is increased the crossover peak $2^3S_1 \rightarrow 3^3P_2$ and 3^3P_1, which is 330 MHz apart from the transition ($2^3S_1 \rightarrow 3^3P_2$), can be observed as shown in Figure 3.13(a).

3.3.2 Red ($\lambda = 780 - 796$ nm) Laser System

The red laser system is also based on a Ti:Sapphire laser (Tekhnoscan Model TIS-SF-07e), but is pumped by an Argon-Ion laser (Coherent Innova 310). The output of this laser is around 1W at a pump power of 10 W. The relatively low power compared to the blue laser system that is pumped with the same amount of power might be caused by several factors: First, the pumping efficiency might be lower because the spectral and the mode quality of the argon-ion laser are not as good as those of the Verdi V10. Second, the ring geometry is different, as the red laser system contains more mirrors and mode-selective elements which can reduce the output power. Third, the quality of Ti:Sapphire crystal is also not as good as that in the blue laser system.

The Tekhnoscan laser system includes an electronic control unit which enables us to control the frequency selecting elements without opening the cavity. Furthermore, part of the output beam is sent to the photodiode **PD1** to track intensity variations (Figure 3.14). The error signal is produced from the **PD1** signal and is fed to **PZT1**, **PZT2**, and **PZT3** to keep the cavity at the length that yields the same intensity. Thus, the laser cavity is locked to the intensity peak measured by **PD1**. In addition, **PZT4** was added to the small mirror to gain fast control of the laser cavity. The same feedback

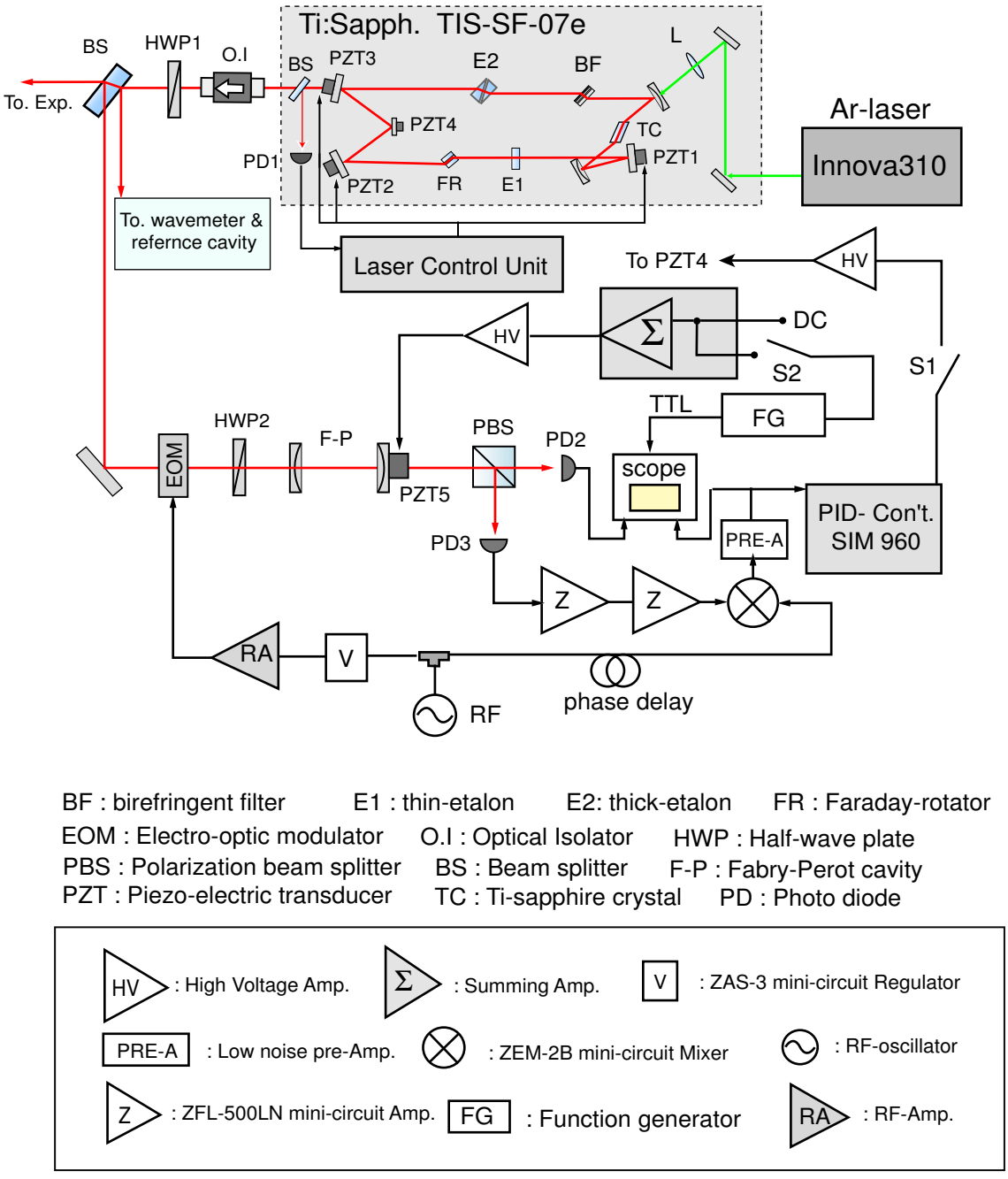

BF : birefringent filter E1 : thin-etalon E2: thick-etalon FR : Faraday-rotator
EOM : Electro-optic modulator O.I : Optical Isolator HWP : Half-wave plate
PBS : Polarization beam splitter BS : Beam splitter F-P : Fabry-Perot cavity
PZT : Piezo-electric transducer TC : Ti-sapphire crystal PD : Photo diode

HV : High Voltage Amp. Σ : Summing Amp. V : ZAS-3 mini-circuit Regulator
PRE-A : Low noise pre-Amp. : ZEM-2B mini-circuit Mixer : RF-oscillator
Z : ZFL-500LN mini-circuit Amp. FG : Function generator RA : RF-Amp.

Figure 3.14: Red laser system.

method as in the blue laser system is used to produce a PDH error signal, and the laser cavity can be locked to the PDH cavity by applying the error signal to **PZT4**. Therefore, either intensity or frequency locking can be used in this laser system.

Chapter 4

Rydberg Atoms

4.1 Introduction

Rydberg atoms are atoms with a single valence electron in highly excited electronic states, named after Swedish physicist Johannes R. Rydberg (1854 - 1919). Their unique properties, e.g. their orbital radius which scales with the square of the principal quantum number n and thus may extend over more than thousands of Bohr radii, make it possible to investigate many atomic properties that cannot be observed with ground state atoms [60, 61]. Furthermore, they can serve as very sensitive field probes that enable us to resolve extremely small perturbations experimentally. Extensive reviews of many aspects of Rydberg atoms are given in Ref. [61].

The goal of this chapter is to describe the advantage of using Rydberg atoms in our experiment. With this in mind the general properties of Rydberg atoms will be briefly reviewed. The effect of external electric fields on Rydberg atoms will be described since the calculation of the Stark shifted energy levels

is important in this experiment

4.2 General Properties of Rydberg Atoms

The role of Rydberg atoms in atomic spectroscopy is described by White [62]. The wavelength for the Balmer series of atomic hydrogen ($n > 2$) is given by the formula [61]:

$$\lambda = \frac{bn^2}{n^2 - 4} \tag{4.1}$$

where $b = 3645.6\,\overset{o}{A}$. This formula gives the wavelengths of the transitions from states with high n to the state with principal quantum number $n = 2$. The significance of the frequency of a transition was realized by Hartley [63], and Eq.(4.1) can be expressed in terms of the wavenumber ν, the inverse of the wavelength in vacuum [61],

$$\nu = \left(\frac{1}{4b}\right)\left(\frac{1}{4} - \frac{1}{n^2}\right) \tag{4.2}$$

In 1890, Rydberg classified the different series of alkali atoms into sharp(s), principal(p), and diffuse(d) series [64]. The wavenumber of the different series can be expressed as [60, 61].

$$\nu_l = \nu_{\infty l} - \frac{R_y}{(n - \delta_l)^2} \quad \text{for} \quad \mathrm{l = s, p, d} \tag{4.3}$$

where the constants $\nu_{\infty l}$ and δ_l are the series limit and the quantum defect, respectively. The constant R_y is called Rydberg constant because it was Rydberg who first realized that this constant is a universal constant for all different kinds of atoms. In addition, Rydberg observed that the wavenumbers of lines

connecting the s and p series, for example, are given by [61, 64]

$$\pm\,\nu = R_y \left[\frac{1}{(m-\delta_s)^2} - \frac{1}{(n-\delta_p)^2} \right] \tag{4.4}$$

where the (+) sign and n represent a sharp series, while the (-) sign and m describe a principal series.

The physical significance of highly excited states became clear when Bohr proposed his model of the hydrogen atom in 1913 [62]. According to the Bohr theory, an electron of charge $-e$ and mass m_e in a circular orbit of radius r around a positive charge Ze follows Newton's law. Combining this with the quantization of angular momentum, $m_e v r = n\hbar$ ($\hbar$: Planck's constant divided by 2π), yields [61]

$$r = \frac{n^2\hbar^2}{Ze^2 m_e k} \tag{4.5}$$

with $k = 1/4\pi\varepsilon_o$, ε_o being the permittivity of free space. For the Hydrogen atom the lowest orbit ($n = 1$) has been assigned a special name, *Bohr radius*, and a symbol a_0. The energy E_n of a state n is obtained by adding its kinetic and potential energies [61],

$$E_n = -\frac{k^2 Z^2 e^4 m_e}{2n^2\hbar^2} = -\frac{m_e c^2 \alpha^2 Z^2}{2n^2} \tag{4.6}$$

where α is the fine structure constant. Since the binding energy is negative, the electron is bound to the proton. The allowed transition frequencies are the differences in the energies given in the above Eq.(4.6) divided by Planck's constant. Comparing this result to the Rydberg formula which is the generalized form of Eq.(4.4) , Bohr showed that the Rydberg constant could be expressed as

$$R_y = \frac{k^2 e^4 m_e}{2\hbar^2} = \frac{m_e c^2 \alpha^2}{2} \tag{4.7}$$

To include the effect of nuclear motion, the electron mass m_e needs to be replaced by $m_e(1+m_e/M)$ (M : nuclear mass) because the Rydberg constant R_y depends on the mass of the nucleus for a given atom. The expression given in Eq.(4.7) is valid for a nucleus of infinite mass.

Property	Formula	n-dependence
Binding energy	$E_n = -R_y/(n-\delta_l)^2$	n^{-2}
Energy difference	$E_n - E_{n-1}$	n^{-3}
Orbital radius $\langle r \rangle$	$\sim \frac{1}{2}[3(n-\delta_l)^2 - l(l+1)]$	n^2
Geometric cross section	$\pi \langle r \rangle^2$	n^4
Dipole moment	$\langle n, l \left\vert er \right\vert n, l+1 \rangle$	n^2
Polarizability	$2e^2 \sum_{n \neq n'} \frac{\vert\langle nlm\vert z\vert n'l'm'\rangle\vert^2}{E_{nlm} - E_{n'l'm'}}$	n^7
Radiative lifetime	$\left(\frac{e^2}{3\hbar c^3 \pi \varepsilon_0} \sum_{n<n'}^{l=l'\pm 1} \frac{l_{\max}}{2l'+1} \omega^3 \left\vert \langle n'l' \left\vert r \right\vert nl \rangle \right\vert^2\right)^{-1}$	n^3
Fine structure		n^{-3}

Table 4.1: General properties of Rydberg Atoms [60, 61]

As given by the equations (4.5) and (4.6) the energy decreases as $1/n^2$ and the orbital radius increases as n^2. In order to realize the importance of these

effects, consider an atom in a relatively low Rydberg state $n = 10$ and compare it to a ground state atom. An hydrogen atom in the ground state is bound by R_y and has an orbital radius a_0. In contrast, the binding energy of the Rydberg atom energy is given by $0.01R_y$ and the orbital radius corresponds to 100 Bohr radii ($100a_0$). As a consequence, the valence electron in a Rydberg atom is in a loosely bound orbit. Thus, an opportunity to study the properties of an atom in a relatively strong field is provided because Rydberg atoms can be easily ionized even by small electric fields. The other unique aspect of Rydberg states comes from their relatively large orbit. The electric dipole moment is proportional to the size of orbital radius, so that Rydberg atoms have both a very large dipole moment and a huge polarizability. Due to this bizarre property, Rydberg atoms are very sensitive to external electric fields. Table 4.1 shows several selected properties of Rydberg atoms and their dependence on the principal quantum number n.

4.3 Schrödinger Equation for Hydrogen Atoms

For developing Rydberg atom wave functions, it is a good starting point to review general features of the hydrogen atom. The Schrodinger equation for the electron of a hydrogen atom, written in atomic units [see Appendix A.1], is [60, 65]

$$\left(-\frac{\nabla^2}{2} - \frac{1}{r}\right)\Psi(\mathbf{r}) = E\Psi(\mathbf{r}) \tag{4.8}$$

From now on, atomic units are used unless otherwise mentioned. In atomic units $e = \hbar = m = 1$ (m : electron mass), $\alpha = 1/137$ and $\alpha c = 1$ (α : fine

structure constant), and also $Z = k = 1$, where $k = 1/4\pi\varepsilon_0$. In a spherical coordinate system ∇^2 can be expressed as

$$\nabla^2 = \frac{\partial^2}{\partial r^2} + \frac{2}{r}\frac{\partial}{\partial r} + \frac{1}{r^2 \sin\theta}\frac{\partial}{\partial\theta}\left(\sin\theta\frac{\partial}{\partial\theta}\right) + \frac{1}{r^2\sin^2\theta}\frac{\partial^2}{\partial\phi^2} \tag{4.9}$$

If we separate the wave function $\Psi(\mathbf{r})$ into a radial and an angular part,

$$\Psi(\mathbf{r}) = Y_{lm}(\theta,\phi)\frac{f(E_n,l,r)}{r} \tag{4.10}$$

then the solutions of the angular part are the spherical harmonics $Y_{lm}(\theta,\phi)$ defined in terms of the associated Legendre polynomials $P_l^m(\cos\theta)$

$$Y_{lm}(\theta,\phi) = \sqrt{\frac{(l-m)!}{(l+m)!}\frac{2l+1}{4\pi}}P_l^m(\cos\theta)\,e^{im\phi} \tag{4.11}$$

where l is a non-negative integer and m takes integral values between $-l$ and l. The radial equation, which gives the energy values, can be written by

$$\left(-\frac{1}{2}\frac{d^2}{dr^2} - \frac{1}{r} + \frac{l(l+1)}{2r^2}\right)f(E_n,l,r) = Ef(E_n,l,r) \tag{4.12}$$

The solutions can be expressed in terms of associated Laguerre polynomials L_{n+l}^{2l+1} [65, 66],

$$f(E_n,l,r) \equiv rR_{nl}(r) = -\frac{\sqrt{(n-l-1)!}}{(n+l)!^{3/2}\sqrt{2n}}\left(\frac{2}{n}\right)^{l+3/2}e^{-\frac{r}{n}}r^{l+1}L_{n+l}^{2l+1}\left(\frac{2r}{n}\right) \tag{4.13}$$

and the corresponding energy eigenvalues are given by

$$E_n = -\frac{R_y}{n^2} \tag{4.14}$$

This result shows that the energy of a hydrogenic energy eigenstate depends only on n, such that states with equal n but different l are degenerate. The

Rydberg constant R_y given in Eq.(4.7) becomes simply 1/2 in atomic units. In our experiment helium atoms are used. In non-hydrogenic atoms, the excited valence electron in a Rydberg state does not only interact with the nucleus, but it is also affected by the core electrons. Considering this effect the Coulomb potential can be modified to the form $-\frac{1}{r} + V_c(r)$, where $V_c(r)$ describes the deviation from $-\frac{1}{r}$ and can include the atomic fine structure as well as core-polarization effects. For large r, the deviation term $V_c(r)$ approaches to zero. For many practical purposes, therefore, it is not necessary to know the exact form of $V_c(r)$, because the wave function of the valence electron far away from the core can be approximated from the well-known hydrogenic wave function except for the phase shift that arises in the core. Considering the effect of the deviation $V_c(r)$, we need to introduce the concept of quantum defect [67].

4.4 Quantum Defect

As described above, the main difference between non-hydrogenic atoms and hydrogen atoms is the influence of the core electrons on the valence electron. When the electron is far from the ionic core, as it is in the case of a high angular momentum l-state, it sees a net charge due to the screening of the core charge by the core electrons and behaves like a hydrogen atom.

However, if the electron penetrates the core, the core electrons no longer shield the nucleus to the same degree. Especially the energies of the low l-states of non-hydrogenic atoms will be depressed with respect to their hydrogenic

$l - value$	a	b	c	d
0	0.296609	-0.038840	0.004960	0.000000
1	0.068320	0.017870	-0.017190	0.000000
2	0.002869	0.006220	0.000000	0.000000
3	0.000240	-0.002090	0.000000	0.000000

Table 4.2: Rydberg-Ritz coefficients for the calculation of the quantum defect of triplet Rydberg helium atoms, but neglecting spin-orbit splitting. The data is obtained from [76].

counterparts by this reduction of shielding caused by core penetration. Taking this into acount, Eq.(4.14) can be corrected [67]

$$E_n = -\frac{R_y}{(n-\delta_l)^2} \tag{4.15}$$

The quantity δ_l is called quantum defect and depends on the angular momentum l. In general, δ_l is a function of n which can be described by the Rydberg-Ritz formula [68]:

$$\delta_l = a + bE_n + cE_n^2 + dE_n^3 + \cdots \tag{4.16}$$

where $a, b, c, d, \cdots$ are the Rydberg-Ritz coefficients for the calculation of the quantum defect [see Table 4.2]. For non-penetrating orbits, core polarization causes similar but much smaller energy shifts.

4.5 The Stark Effect on the Hydrogen Atom

The Stark effect in Rydberg atoms has been an interesting subject since the research on the Stark structure of Rydberg states of alkali metals by Zimmerman *et al.*[69]. Because the valence electron in Rydberg atoms sees the ionic core like a positive net charge, it can be a useful starting point to consider the Stark structure of the hydrogen atom. The Hamiltonian describing the interaction of the atom with an uniform electric field **F** directed along the z-axis is [69]

$$H_F = -\mathbf{p} \cdot \mathbf{F} = Fz \tag{4.17}$$

where **p** is the electric-dipole operator. If we neglect electron and nuclear spin, the Schrödinger equation for the hydrogen atom in a static electric field is given by [69]

$$\left(-\frac{1}{2}\nabla^2 - \frac{Z}{r} + Fz\right)\Psi(\mathbf{r}) = E\Psi(\mathbf{r}) \tag{4.18}$$

Eq.(4.18) is separable in parabolic coordinates ξ, η, φ which are defined by the relations [66]

$$\begin{aligned} \xi &= r + z, \\ \eta &= r - z, \\ \varphi &= \arctan(y/x) \end{aligned} \tag{4.19}$$

Using Eq.(4.19), the operator ∇^2 can be expressed as

$$\nabla^2 = \frac{4}{\xi+\eta}\frac{d}{d\xi}\left(\xi\frac{d}{d\xi}\right) + \frac{4}{\xi+\eta}\frac{d}{d\eta}\left(\eta\frac{d}{d\eta}\right) + \frac{1}{\xi\eta}\frac{d^2}{d\varphi^2} \tag{4.20}$$

We assume that the solution of the Schrödinger equation (4.18) can be written in the form,

$$\Psi(\xi,\eta,\varphi)=\Phi_1(\xi)\,\Phi_2(\eta)\,e^{\pm im\varphi}\quad,\quad Z_1+Z_2=Z\,(m\geq 0) \tag{4.21}$$

where Z_1 and Z_2 are separation constants which may be thought as the positive charges binding the electron in the ξ and η coordinates.

Substituting Eqs.(4.20) and (4.21) into Eq.(4.18), we extract two separate equations for $\Phi_1(\xi)$ and $\Phi_2(\eta)$

$$\begin{aligned}\frac{d}{d\xi}\left(\xi\frac{d\Phi_1}{d\xi}\right)+\left(\frac{1}{2}E\xi+Z_1-\frac{m^2}{4\xi}-\frac{1}{4}F\xi^2\right)\Phi_1 &= 0,\\ \frac{d}{d\eta}\left(\eta\frac{d\Phi_2}{d\eta}\right)+\left(\frac{1}{2}E\eta+Z_2-\frac{m^2}{4\eta}+\frac{1}{4}F\eta^2\right)\Phi_2 &= 0,\end{aligned} \tag{4.22}$$

These ordinary differential equations (4.22) can be directly integrated or they may be treated by means of a perturbation procedure. In the low electric field region, the perturbation theory starting from the zero field solutions will give a satisfactory result . In the case of $F=0$ in Eq.(4.22), the normalized solution has the form of [66]

$$\begin{aligned}\Phi_1 &= \frac{\sqrt{n_1!}}{(n_1+m)!^{3/2}}e^{-\frac{1}{2}\varepsilon\xi}\xi^{\frac{1}{2}m}\varepsilon^{\frac{1}{2}(m+1)}L^m_{n_1+m}(\varepsilon\xi),\\ \Phi_2 &= \frac{\sqrt{n_2!}}{(n_2+m)!^{3/2}}e^{-\frac{1}{2}\varepsilon\eta}\eta^{\frac{1}{2}m}\varepsilon^{\frac{1}{2}(m+1)}L^m_{n_2+m}(\varepsilon\eta),\end{aligned} \tag{4.23}$$

with $\varepsilon=\sqrt{-2E}$. $L^m_{n_i+m}(x)$ ($x=\varepsilon\xi$ or $\varepsilon\eta$) is the Laguerre polynomial [65, 66], and $n_i = Z_i n-(m+1)/2$ $(i=1,2)$. The relation between the quantum numbers $n,|m|$, and the parabolic quantum numbers $n_1,\ n_2$ is given by

$$n=n_1+n_2+|m|+1 \tag{4.24}$$

Here, $n_1,\ n_2$ represent the numbers of nodes in the wave functions given in Eq.(4.23). The perturbation procedure takes the separation parameters Z_i as the eigenvalues instead of the energy E. The eigenvalue Z_i, in the case of $F = 0$, can be expressed in terms of the electric quantum number n_i and the magnetic quantum number m [66].

$$Z_i^{(0)} = \left(n_i + \frac{m+1}{2}\right)\varepsilon \tag{4.25}$$

If $F \neq 0$, the first order perturbation term $Z_i^{(1)}$ can be obtained by the integral of the perturbation potential evaluated over the unperturbed eigenfunctions given in Eq.(4.23).

$$Z_i^{(1)} = \pm\frac{1}{4}F\varepsilon^{-2}\left(6n_i^2 + 6n_i m + m^2 + 6n_1 + 3m + 2\right) \tag{4.26}$$

The signs $+, -$ are for $i = 1, 2$ respectively. Eqs (4.25) and (4.26), together with the relation $Z = Z_1 + Z_2$, leads to the first order perturbed term for the energy:

$$E = -\frac{1}{2}\varepsilon^2 = -\frac{1}{2}\frac{Z^2}{n^2} + \frac{3}{2}\frac{Fn}{Z}\left(n_1 - n_2\right) \tag{4.27}$$

In the next order of perturbation theory, a quadratic term in the electric field appears in addition to the linear Stark effect in Eq.(4.27). This can be calculated by second order perturbation theory and the resulting energy is given by [65, 66].

$$\begin{aligned} E &= E^{(0)} + E^{(1)} + E^{(2)} \\ &= -\frac{Z^2}{2n^2} + \frac{3}{2}F\left(\frac{n}{Z}\right)\left(n_1 - n_2\right) \\ &\quad -\frac{1}{16}F^2\left(\frac{n}{Z}\right)^4\left[17n^2 - 3\left(n_1 - n_2\right)^2 - 9m^2 + 19\right] \end{aligned} \tag{4.28}$$

Silverstone [70] calculated to higher order, but the first and second order shifts are adequate for many applications. For example, E. Luc-Koenig *et al.* [71] showed that the energy levels of the hydrogen atom exhibit linear Stark shifts from zero field to the point at which field ionization occurs. On the other hand, Peter M. Koch observed that even the second order energy levels are not valid for a certain precise measurement [72].

4.6 Stark Effect in Helium Atoms

For helium atoms, the hydrogenic case only can apply for high l values, and the Stark shifts produced by relatively weak fields are proportional to the square of the electric field intensity [66]. The quantum mechanical calculations for Rydberg atoms in electric fields was described by Zimmerman *et al.*, in 1979 [69]. For an atom in an external field, the total Hamiltonian is given by [69]

$$H = H_0 + Fz + H_{fs} \tag{4.29}$$

where H_0 is the Hamiltonian of the unperturbed system, and H_{fs} the energy shift of the states due to fine-structure. It is experimentally important for the heavier atoms, but the fine structure in the Rydberg levels of He is small and can be neglected for high n states [73]. The diagonal elements of this Hamiltonian matrix are the zero-field energies, which can be calculated with the formula (4.15) using known quantum defect values [74]. It means that unperturbed energies are diagonal in a spherical basis, not a parabolic basis. Therefore, it is essential not only to transform the representation from spherical, to parabolic, basis, but also to generalize the parabolic states to

non-integral order [75]. Since there is no advantage in employing a parabolic representation for He as was used in the alkali atoms [69], the Stark problem for He was treated in a spherical basis. The electric field contribution to the Stark effect is represented in the off-diagonal elements in the basis provided by the eigenvector $|nlm\rangle$ of the zero-field Hamiltonian [69].

$$\langle nlm\,|Fz|\,n'l'm'\rangle = \delta\,(m,m')\,\delta\,(l,l\pm1)\,F\,\langle lm\,|\cos\theta|\,l'm'\rangle\,\langle nl\,|r|\,n'l'\rangle \quad (4.30)$$

where, the unit of Eq.(4.30) is explicitly ea_0($= 1$ in atomic unit, a_0 : Bohr radius) and $\delta\,(m,m') = 0$ unless $m = m'$. The angular part solution is analytically given by a spherical harmonics [69]

$$\begin{aligned}\langle l,m\,|\cos\theta|\,l-1,m'\rangle &= \sqrt{\frac{l^2-m^2}{(2l+1)\,(2l-1)}},\\ \langle l,m\,|\cos\theta|\,l+1,m'\rangle &= \sqrt{\frac{(l+1)^2-m^2}{(2l+3)\,(2l+1)}}\end{aligned} \quad (4.31)$$

The main task of computation is to evaluate the radial matrix elements $\langle nl\,|r|\,n'l'\rangle$. In the method described in Ref. [69], numerical integration of the radial equation at the quantum-defect shifted energy gave the most satisfactory results. After all matrix elements are evaluated, the resulting matrix is diagonalized. The resulting energy levels plotted as a function of field strength is called a Stark map. For ^{4}He at n=26, such a map, shown in Figure 4.1, displays the shifts of the s, p states due to their quantum defects. For the manifold (region **A**, $l > 3$), the external field lifts the degeneracy of the zero-field energy levels. In addition, anti-crossings are clearly observable in the areas such as **B**. Since a non-hydrogenic He core breaks the Coulomb symmetry and couples the Stark levels, anti-crossing effects dependent on the coupling strengths arise [77].

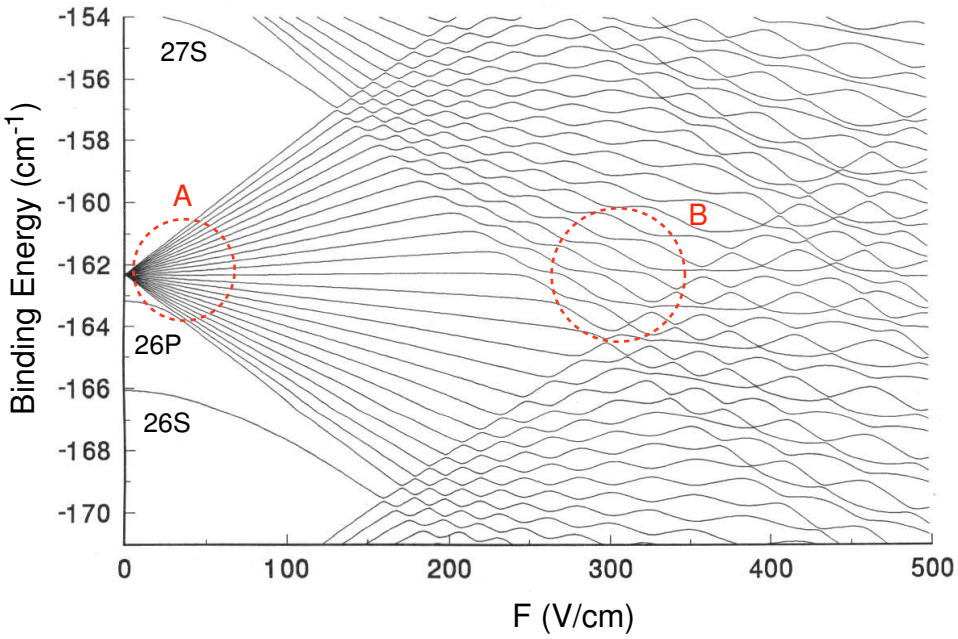

Figure 4.1: Electric field dependence of the excitation spectra for n=26 (Stark map) [76]

We did spectroscopy experiments to observe these energy levels. In our experiments, the 389 nm laser was locked to the transition from the state 2^3S_1 to the state 3^3P_2 and the wavelength of the red laser was moved between 796.41 nm and 796.81 nm [see Figure 3.1]. In order to observe the transition signals, the red laser was also locked after being tuned to the desired wavelength. Then the lower-field plate was scanned with function generator (amplitude V_{PP} : 10 V , frequency : 100 Hz) and the applied voltage to the upper field-plate was slowly moved [the geometry of the field plates is presented in Figure 3.5(b)].

The ion-signals are observed when the frequency of the red laser is on resonance with a transition to one of the Stark energy levels. Because of the

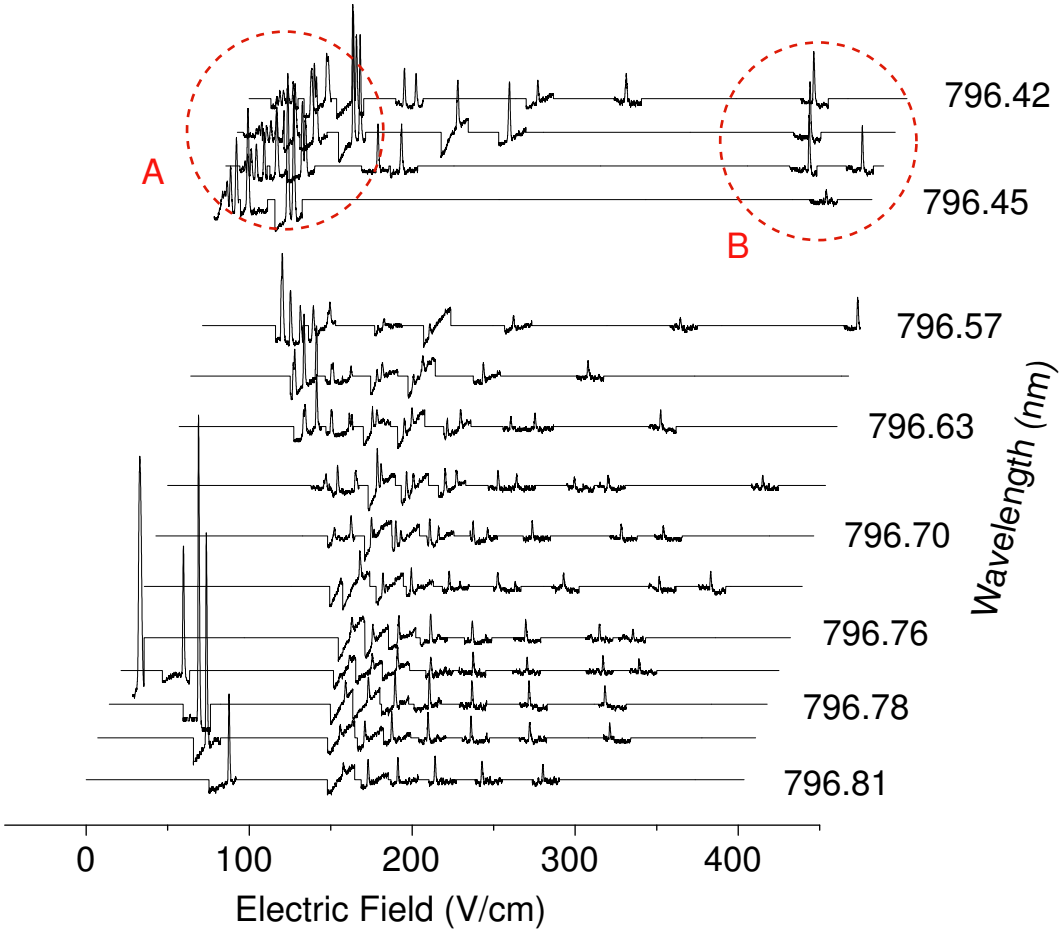

Figure 4.2: Experimentally obtained Stark map for n=26

mode-hops of the red laser at some wavelengths, it was impossible to observe the resonance peaks for all the regular spacings of wavelength as shown in Figure 4.2. The strongly deppressed s-state is clearly observed. The manifolds and their anti-crossings are represented by A and B, respectively, with dot-circle.

4.7 Oscillator Strengths and Lifetimes

The relative intensities of the Stark manifold spectral peaks are determined by the probability that an atom will undergo a transition from the state nlm to $n'l'm'$ [66]. To calculate the strength of a certain transition it is convenient to introduce the oscillator strength defined as [66, 78]

$$f_{n'l'm',nlm} = 2\frac{m}{\hbar}\omega_{n'l',nl}\left|\langle n'l'm'\left|z\right|nlm\rangle\right|^2 \tag{4.32}$$

where $\omega_{n'l',nl} = (E_{n'l'} - E_{nl})/\hbar$. This equation shows that the oscillator strength corresponding to a transition $nlm \rightarrow n'l'm'$ depends on the orientation of the z-axis, that is, on the direction of polarization. For the sum of the oscillator strengths for all transitions from a definite state n of the atom, the Thomas-Reiche-Kuhn rule applies [65, 66, 78]

$$\sum_{n'l'm'} f_{n'l'm',nlm} = Z \tag{4.33}$$

where Z is the total number of electrons in the system. This is a very general rule which holds for any atom or molecule, with or without external fields, for any polarization direction. In free space, the radiative decay rate of an atom cannot depend upon the magnetic quantum number m. Therefore, it is useful

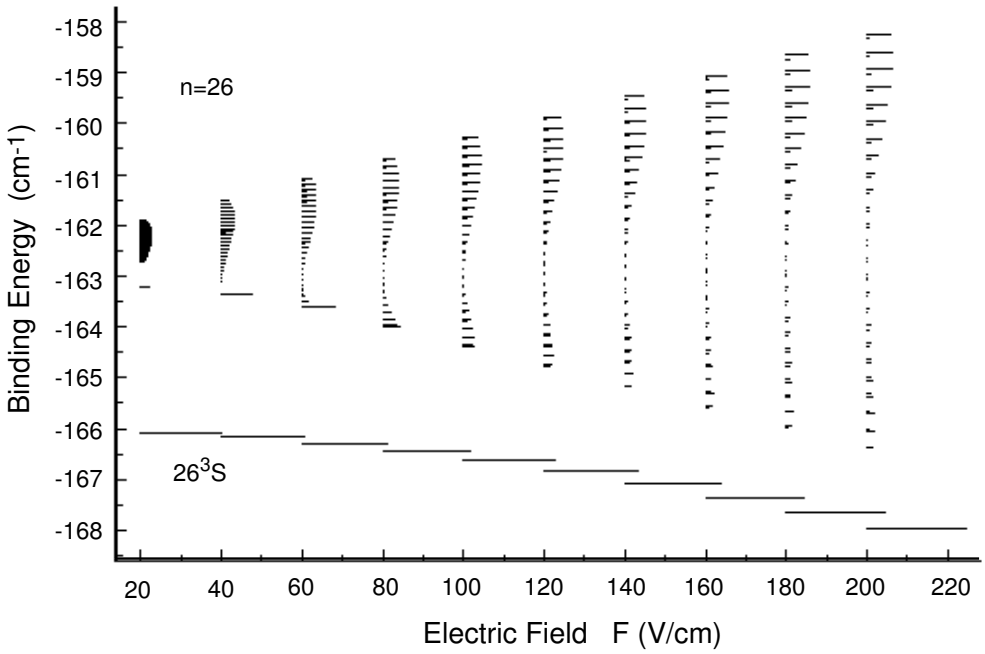

Figure 4.3: He triplet Stark intensities

to define an average oscillator strength of the transition $nl \rightarrow n'l'$, which is independent of polarization and m, as [61, 66]

$$\bar{f}_{n'l',nl} = \frac{2}{3}\frac{m}{\hbar}\omega_{n'l',nl}\frac{l_{\max}}{2l+1}\left|\langle n'l'\left|r\right|nl\rangle\right|^2 \tag{4.34}$$

where $l_{\max}$ is the larger of l and l'. $2l+1$ is the degree of degeneracy of the initial state. If we reverse the roles of l and l', it is straightforward to show that

$$\bar{f}_{n'l',nl} = -\frac{2l'+1}{2l+1}\bar{f}_{nl,n'l'} \tag{4.35}$$

The average oscillator strength (4.34) also follows a sum rule [61, 66]

$$\sum_{n'}\bar{f}_{n'l-1,nl} \;\; = \;\; -\frac{1}{3}\frac{l(2l-1)}{2l+1}$$

$$\sum_{n'} \bar{f}_{n'l+1,nl} = \frac{1}{3}\frac{(l+1)(2l+3)}{2l+1} \tag{4.36}$$

With this result, it is possible to calculate the sum of the oscillator strengths of all the transitions from a certain level nl to the levels of a fixed orbital quantum number. From (4.36) it is apparent that

$$\sum_{n'l'} \bar{f}_{n'l',nl} = 1 \tag{4.37}$$

where $l' = l \pm 1$. Eq.(4.36) shows that among the transitions $nl \rightarrow n'l-1$ the ones which lead to lower energies predominate, whereas the strongest $nl \rightarrow n'l+1$ transitions are to higher energies.

For the application to the atom optics we are interested in the Stark state with the highest transition probability. This can be estimated through the distribution of oscillator strengths among a manifold of Rydberg Stark states. The numerical calculation for the intensity of excitation of $n = 26$ Stark states from 3^3P_2 state is shown in Figure 4.3.

Comparing the theoretical calculation with the experimental result [see Figure 4.4] leads to a different behavior. The strongest transition occurs at near zero field and decreases with increasing the electric fields, which is opposite to the calculation. We propose that the difference comes from the slope of $26S$ levels. Since the energies behave quadratically with field, the range of field values lying within the resonance width decreases as the field increases. Therefore the fraction of atoms that are resonant decreases with field. This does not lead to line broadening with field because changing the electric field value does not bring relatively more atoms into resonance at higher electric fields.

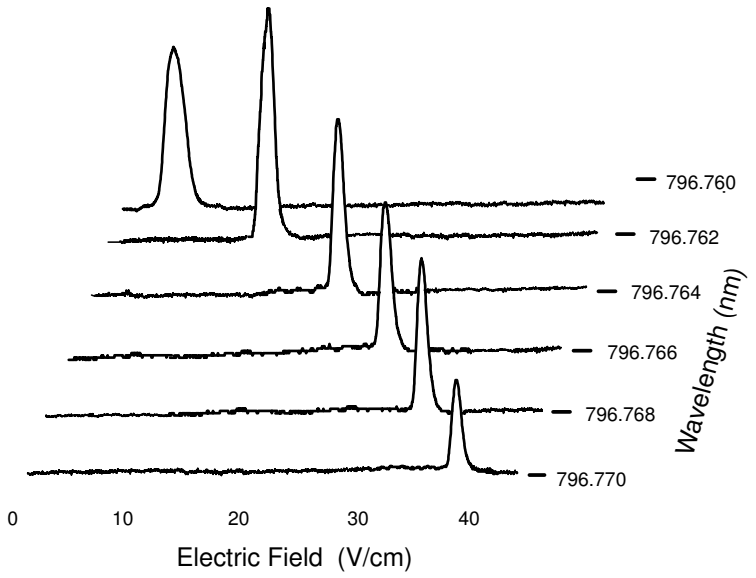

Figure 4.4: Transition strength for n=26S Stark states

The Einstein A coefficient, which defines the spontaneous decay rate of the nl state to the lower lying $n'l'$ state, also can be expressed in terms of the average oscillator strength [61, 66]

$$A_{n'l',nl} = -\frac{2e^2\omega^2_{n'l',nl}}{mc^3}\bar{f}_{n'l',nl} \tag{4.38}$$

In general, the radiative lifetime, τ_{nl}, of the nl state is defined by the inverse of the total spontaneous decay rate [61].

$$\tau_{nl} = \left[\sum_{n'l'} A_{n'l',nl}\right]^{-1} \tag{4.39}$$

We can also define the branching ratio $b_{n'l',nl}$ for the decay from the state nl to a particular state $n'l'$ as

$$b_{n'l',nl} = \frac{A_{n'l',nl}}{\sum\limits_{n'l'} A_{n'l',nl}} = \tau_{nl}A_{n'l',nl} \tag{4.40}$$

Chapter 5

Coherent Manipulation of Atoms

5.1 Introduction

Coherent excitation of atoms to well-defined quantum states has been a crucial issue in atomic and molecular experiments [80]. In our experiment, we want to achieve a highly efficient population transfer from the metastable state 2^3S_1 of helium to Rydberg states. Then the atomic beam can be focused because of the large interaction of the Rydberg helium atoms in an inhomogeneous electrostatic field. Incoherent excitation does not transfer a significant fraction of atoms to the excited state. The possibility of coherent population transfer with high efficiency by suitably delayed pulses was first predicted in 1984 by Oreg *et al.* [81] and the technique to achieve a complete population transfer to the excited states, such as the Stimulated Raman Adiabatic Passage (STIRAP) method, was introduced by Bergmann and coworkers [82]. This chapter describes different techniques that can be used to transfer population. Starting with two-state systems, we consider the efficiency of each

method of population transfer. Then the three-state STIRAP technique is described.

5.2 Population Transfer in a Two Level System

For the case of a two-state atomic system in incoherent radiation, the rate of change in an atomic population was first predicted by Einstein [83]. The changes induced by radiation are caused by absorption, stimulated emission, and spontaneous emission. If sufficiently intense radiation near the atomic resonance frequency is applied to a ground atomic state so that stimulated emission dominates spontaneous emission, then the excited state population at time t is

$$P_{ex}(t) = \frac{1}{2}\left\{1 - \exp\left[-B\int_0^t u(t')dt'\right]\right\} \tag{5.1}$$

where B is the Einstein B (absorption) coefficient and $u(t)$ is the spectral energy density. This equation shows that the excited state population reaches, at most, the saturation value of 50 %, which is the best transfer efficiency in the incoherent radiation regime [*incoh.exc.* line in Figure 5.1].

However, when unexcited atoms are exposed to a coherent radiation field, Eq.(5.1) is no longer valid and one has to obtain the probability $P_n(t) = |C_n(t)|^2$ of finding the system in state $|n\rangle$ at time t by calculating the probability amplitude $C_n(t)$ starting from the time-dependent Schrödinger equation

$$\frac{d}{dt}C_n(t) = -\frac{i}{\hbar}\sum_m H_{mn}(t)\, C_m(t) \tag{5.2}$$

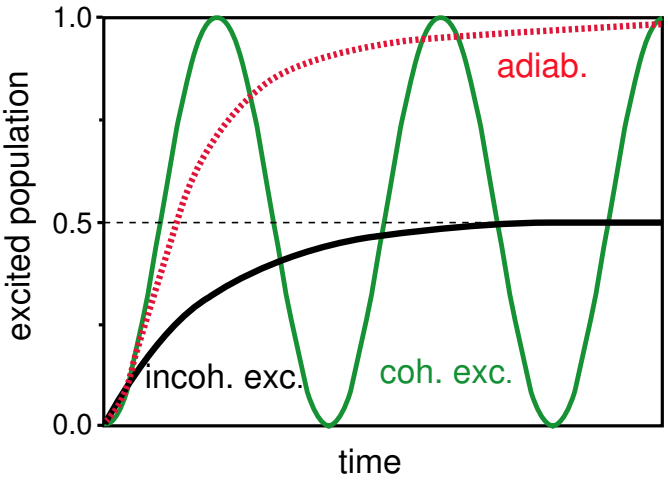

Figure 5.1: Evolution of the population of the upper state in a two state system [80].

where the Hamiltonian matrix elements H_{mn} represent the interaction between the atom and radiation field.

As shown in Figure 5.2, consider the case of idealization of the radiation as a monochromatic field $\mathbf{E}(\mathbf{r},t) = \mathbf{E}_0 \cos(\mathbf{k}\cdot\mathbf{r} - \omega t)$ with frequency ω and amplitude $|\mathbf{E}_0|$. The relevant quantity to determine the rate of population transfer produced by coherent excitation between ground state $|g\rangle$ and excited state $|e\rangle$ is the strength of the interaction, namely the Rabi frequency [2, 84]:

$$\Omega = -\frac{e\,|\mathbf{E}_0|}{\hbar}\,\langle e\,|r|\,g\rangle \tag{5.3}$$

In Eq.(5.2), an atom-field interaction Hamiltonian is given by [85]

$$H = H_0 + H' = \hbar \begin{pmatrix} \omega_g & 0 \\ 0 & \omega_e \end{pmatrix} + \hbar \begin{pmatrix} 0 & \Omega\cos\omega t \\ \Omega\cos\omega t & 0 \end{pmatrix} \tag{5.4}$$

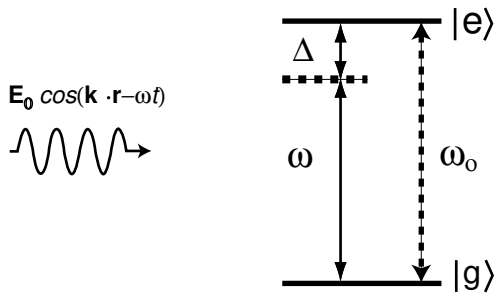

Figure 5.2: Atom-Field Interaction. ω_0 is the Bohr frequency corresponding to the frequency difference ω_g and ω_e , which are the frequencies of the ground and excited states, respectively.

where ω_g and ω_e are the atomic energy frequencies corresponding to the two relevant states $|g\rangle$ and $|e\rangle$, respectively. If we solve (5.2) with this Hamiltonian under the rotating wave approximation, the excitation probability can be deduced [85]

$$P_{ex}(t) = \frac{1}{2}\left(\frac{\Omega}{\Omega_{eff}}\right)^2 [1 - \cos(\Omega_{eff}t)] \tag{5.5}$$

where the effective Rabi frequency is defined by

$$\Omega_{eff} \equiv \sqrt{\Omega^2 + \Delta^2} \tag{5.6}$$

and Δ denotes the frequency detuning from resonance ($\Delta = \omega - \omega_0$). As we can see from (5.5), the oscillations in population become more rapid with increasing $|\Delta|$ and in general, the population will never be transferred completely to the excited state unless $\Delta = 0$. However, for the resonance case, that is $\Delta = 0$, the population oscillates between 0 and 1 with Rabi frequency Ω as shown in Figure 5.1 (*coh.exc* line). Thus, for $\cos(\Omega t) = -1$, the population is completely inverted. In a real experiment, one usually deals with an inhomogeneously

broadened system such as a thermal gas. Since the atoms have a certain velocity distribution they see the frequency of the applied field by the Doppler effect. This causes a detuning effect so that the maximum population of the ensemble in the excited state is always less than 1. In addition, the atoms may experience different intensities across the field so that they cannot fulfill the complete transfer simultaneously due to the different values of Ωt. These experimental limitations require an averaging over the theoretical excitation probabilities, resulting in a less efficient population transfer than in the case of interaction between single stationary atoms and fields of constant intensity.

Another robust method for achieving efficient population transfer is adiabatic rapid passage (ARP). In this technique, the frequency of the external field is slowly tuned across the atomic resonance from below resonance ($\Delta \ll \Omega$) to above resonance ($\Delta \gg \Omega$) or in reverse. The time scale of this frequency sweep must be slower than the Rabi frequency ($T \gg \Omega^{-1}$), but faster than spontaneous emission ($T \ll \Gamma^{-1}$) , here Γ is the decay rate of the upper state. For a quantitative analysis of this process, we can turn to the adiabatic theorem of quantum mechanics. In the rotating frame the time dependent Hamiltonian in (5.4) can be expressed as [2, 86]

$$H_{eff} = \frac{\hbar}{2} \begin{bmatrix} 0 & \Omega \\ \Omega & -2\Delta \end{bmatrix} \tag{5.7}$$

The basis for this Hamiltonian is given by $|g, n+1\rangle$, where the atom is in the ground state and the field contains $n+1$ photons, and $|e, n\rangle$, where the atom is in the excited state and the field contains n photons.

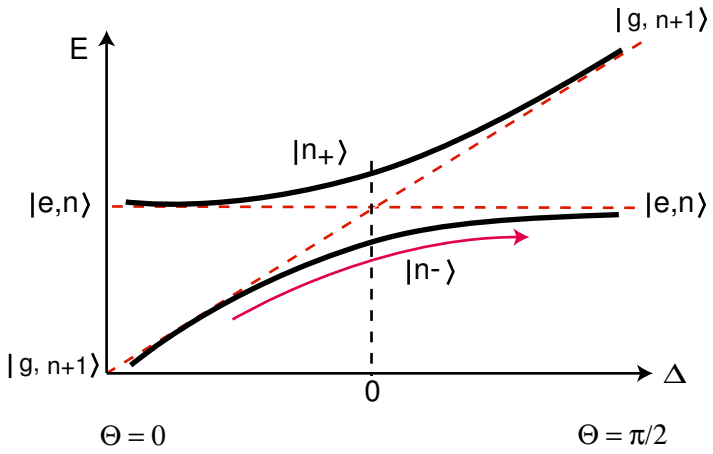

Figure 5.3: Graph of eigenvalues of the dressed states as a function of detuning (Δ)

The eigenvalues of (5.7) are:

$$E_{\pm} = \frac{\hbar}{2}\left(\Delta \pm \sqrt{\Omega^2 + \Delta^2}\right) \tag{5.8}$$

and the corresponding eigenvectors are:

$$\begin{aligned} |n+\rangle &= \sin\Theta\,|g, n+1\rangle + \cos\Theta\,|e, n\rangle \\ |n-\rangle &= \cos\Theta\,|g, n+1\rangle - \sin\Theta\,|e, n\rangle \end{aligned} \tag{5.9}$$

where the mixing angle Θ is defined as

$$\Theta = \frac{1}{2}\tan^{-1}\left(\frac{\Omega}{\Delta}\right) \tag{5.10}$$

Therefore the energy separation of these eigenstates is just the effective Rabi frequency Ω_{eff}(5.6). Figure 5.3 shows the energies of the eigenstates as a function of the detuning given in Eq.(5.8). When $\Theta = 0$ ($\Delta < 0$), the eigenstate $|n-\rangle$ becomes $|g, n+1\rangle$. If we increase the interaction strength Ω

and cross the resonance ($\Delta = 0$), then the state $|n-\rangle$ evolves into a mixture of $|g, n+1\rangle$ and $|e, n\rangle$. After passing through the resonance Ω starts to decrease and Δ moves to a positive detuning, so that Θ goes to $\pi/2$, that is, $|n-\rangle$ ends up in the state $|e, n\rangle$. This process requires the adiabatic condition [87, 88]:

$$\sqrt{\Omega^2 + \Delta^2(t)} \gg \left| \frac{d}{dt}\Theta(t) \right| \tag{5.11}$$

Finally the excited state can be populated up to an efficiency of 100 % through adiabatic following on the lower branch in Figure 5.3 [89]. The eigenstates of the Hamiltonian given in (5.7) are known as the *dressed states*, since the laser field dresses the bare atomic states.

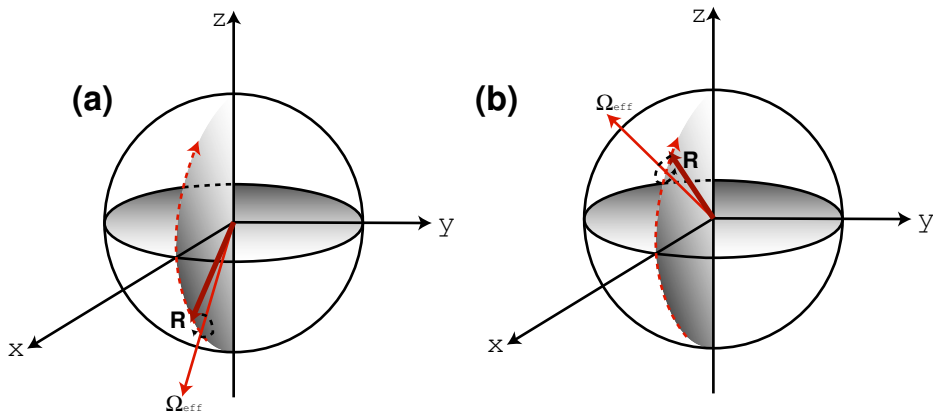

Figure 5.4: Bloch sphere description of adiabatic rapid passage

Another description for adiabatic passage is based on the Bloch vector model. Consider atoms in the ground state (south pole of the Bloch sphere) and a laser detuned to the far red, that is, $|\Delta| \gg \Omega$. The Bloch vector $\mathbf{R}$, initially parallel to the effective Rabi frequency vector Ω_{eff}, will precess around Ω_{eff} at frequency Δ. Now suppose we sweep the detuning Δ, changing

the direction of Ω_{eff}, through resonance slowly compared to $|\Omega_{eff}|$. The Bloch vector $\mathbf{R}$ will then adiabatically follow Ω_{eff} and end up parallel to Ω_{eff} in the excited state (north pole of the Bloch sphere) [Figure 5.4]. Additionally, this process must be completed in a time shorter than the radiative lifetime of the excited state, and that's why this process known as adiabatic rapid passage.

5.3 Theory of the Three-state STIRAP

In the STIRAP procedure, three states, labeled $|1\rangle$, $|2\rangle$, and $|3\rangle$, are linked by two successive interactions, $|1\rangle - |2\rangle$ and $|2\rangle - |3\rangle$ by pump and Stokes fields [Figure 5.5]. When two coherent fields are pulsed and ordered in counterintuitive sequence, in which the Stokes field precedes the pump field, complete population transfer from the initial state $|1\rangle$ to the final state $|3\rangle$ can be produced.

The simple analysis of STIRAP begins with the time-dependent Schrodinger equation (5.2) for a three-level atom. Under the rotating-wave approximation (RWA), the Hamiltonian of the interaction between the non-degenerate three states and two coherent radiation fields is [85]:

$$H(t) = \frac{\hbar}{2} \begin{pmatrix} 0 & \Omega_P(t) & 0 \\ \Omega_P(t) & 2\Delta_P & \Omega_S(t) \\ 0 & \Omega_S(t) & 2\left(\Delta_P - \Delta_S\right) \end{pmatrix} \tag{5.12}$$

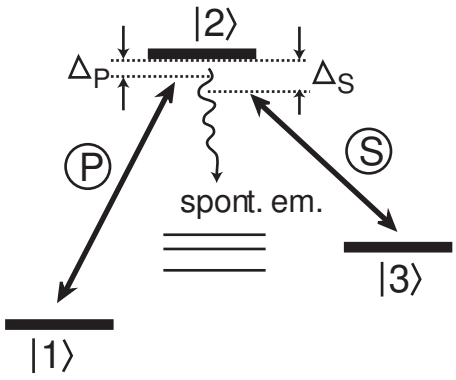

Figure 5.5: Three-level excitation scheme. The initially populated state $|1\rangle$ and the final state $|3\rangle$ are coupled by the pump laser P and the Stokes laser S via an intermediate state $|2\rangle$ [80].

Here $\Omega_P(t)$ and $\Omega_S(t)$ are the Rabi frequencies of the pump and Stokes fields determining the coupling strength between the related states, while the detunings are defined by $\hbar\Delta_P = (E_2 - E_1) - \hbar\omega_P$, $\hbar\Delta_S = (E_2 - E_3) - \hbar\omega_S$ (ω_P and ω_S are the frequencies of pump and Stokes fields, respectively as shown in Figure 5.5.)

In the case of STIRAP, the two-photon resonance condition between states $|1\rangle$ and $|3\rangle$ should be fulfilled, that is, $\Delta_P = \Delta_S = \Delta$. Solving the eigenvalue equation for (5.12) yields the three energies of the dressed states which are the eigenstates of the atom-field interaction system, namely [85];

$$\begin{aligned} \omega^+(t) &= \Delta + \sqrt{\Delta^2 + \Omega_P^2(t) + \Omega_S^2(t)} \\ \omega^0(t) &= 0 \\ \omega^-(t) &= \Delta - \sqrt{\Delta^2 + \Omega_P^2(t) + \Omega_S^2(t)} \end{aligned} \tag{5.13}$$

The corresponding eigenstates $|a^+\rangle$, $|a^0\rangle$, and $|a^-\rangle$ are represented by the linear

combination of the bare states $|1\rangle$, $|2\rangle$, and $|3\rangle$ [85]:

$$\begin{aligned}
\left|a^{+}\right\rangle &= \sin\theta\sin\varphi\,|1\rangle + \cos\varphi\,|2\rangle + \cos\theta\sin\varphi\,|3\rangle \\
\left|a^{0}\right\rangle &= \cos\theta\,|1\rangle - \sin\theta\,|3\rangle \\
\left|a^{-}\right\rangle &= \sin\theta\cos\varphi\,|1\rangle - \sin\varphi\,|2\rangle + \cos\theta\cos\varphi\,|3\rangle
\end{aligned} \tag{5.14}$$

where the time-dependent mixing angles $\theta(t)$ and $\varphi(t)$ are defined by the relationship

$$\begin{aligned}
\tan\theta(t) &= \Omega_P(t)/\Omega_S(t) \\
\tan 2\varphi(t) &= \sqrt{\Omega_P^2(t) + \Omega_S^2(t)}/\Delta
\end{aligned} \tag{5.15}$$

One of the dressed states in (5.14) has no component of the state $|2\rangle$, and is thus only a coherent superposition of the initial state $|1\rangle$ and the final state $|3\rangle$. For atoms in the state $|2\rangle$ there are several decay channels due to spontaneous emission, and these are the main reason for population loss. Efficient population transfer is possible if these losses can be minimized or avoided. In that respect the state $|a^0\rangle$, known as a *trapped state*, turns out to be an appropriate vehicle for the most efficient population transfer. Note that the state vector $|\Psi\rangle$, which describes the time evolution of a system, can be expanded in terms of the bare $\{|1\rangle, |2\rangle, |3\rangle\}$ or dressed $\{|a^-\rangle, |a^0\rangle, |a^+\rangle\}$ states. As long as the state vector $|\Psi\rangle$ is bound to the trapped state $|a^0\rangle$, the intermediate state $|2\rangle$ is not involved in the process of population transfer and will never be populated throughout the whole interaction time. Therefore, we need to know how to tie the state vector $|\Psi\rangle$ to the state $|a^0\rangle$.

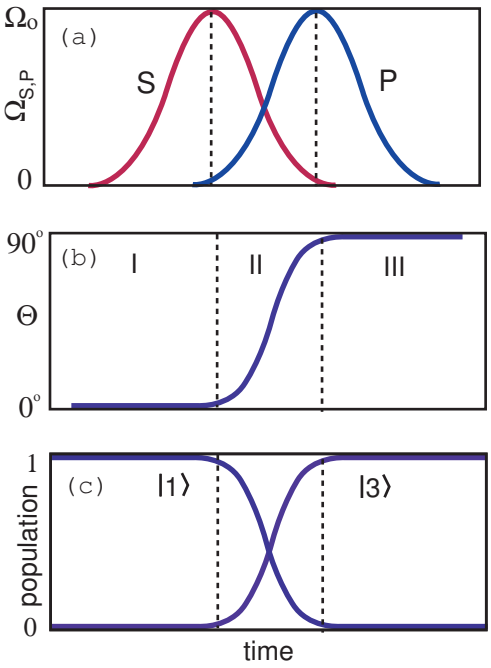

Figure 5.6: Time dependence of the pump and Stokes Rabi frequencies $\Omega_{S,P}$, the mixing angle Θ, and the populations in three-state STIRAP [80]

In Figure 5.6, the atoms are exposed to the Stokes field first and see the pump field later:

$$\begin{aligned} \frac{\Omega_P(t \to 0)}{\Omega_S(t \to 0)} &\to 0 \qquad \text{(region I)} \\ \frac{\Omega_S(t \to \infty)}{\Omega_P(t \to \infty)} &\to 0 \qquad \text{(region III)} \end{aligned} \tag{5.16}$$

In this case, the mixing angle $\theta(t)$ defined by (5.15) rises from $\theta(t \to 0) = 0$ to $\theta(t \to \infty) = \pi/2$. From Eq. (5.14) we see, that the state $|a^0\rangle$ evolves from the initial state $|1\rangle$ $(t \to 0)$ to a superposition of states $|1\rangle$ and $|3\rangle$ in the region **II** and finally to the state $|3\rangle$ as $t \to \infty$. Consequently, the population can be completely transferred from the initial state $|1\rangle$ to the final state $|3\rangle$ by means

of an adiabatic link of those states.

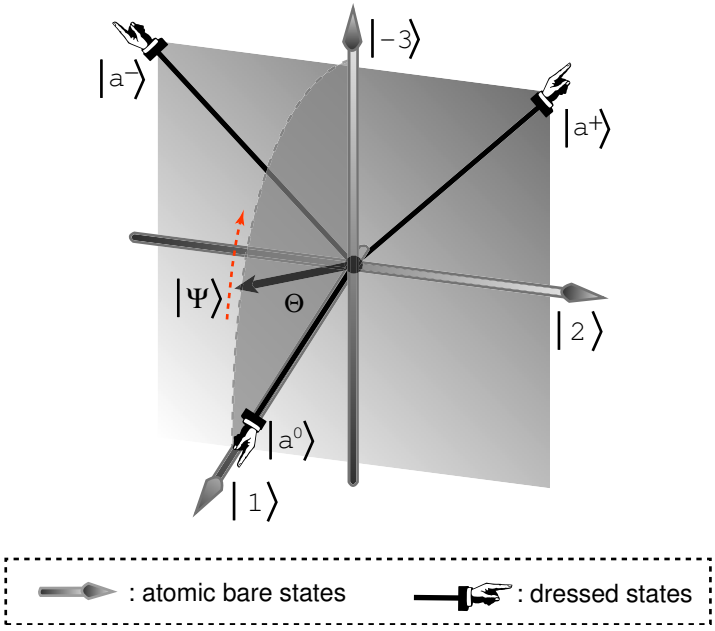

Figure 5.7: Vector picture of STIRAP. $|1\rangle$, $|2\rangle$, and $|3\rangle$ are atomic bare states. $|a^0\rangle$, $|a^-\rangle$, and $|a^+\rangle$ are the dressed states. $|\Psi\rangle$ is the state vector and Θ represents the mixing angle [80, 90]

A vector picture of this STIRAP process is also shown in Figure 5.7. At the very early times, atomic beam only sees a very weak Stokes field first. The atomic system is not perturbed by the field, so we can think the state vector $|\Psi\rangle$ is lined up to the atomic bare state $|1\rangle$ and the dressed state $|a^0\rangle$, that is, $|\langle a^0 | \Psi \rangle| = 1$. At this point the bare states $|2\rangle$ and $|3\rangle$ are coupled by the Stokes field so that these two states start to be split while state $|1\rangle$ stays without any interaction. When the Stokes field reaches its maximum intensity, the energy splitting between states $|2\rangle$ and $|3\rangle$ will also be maximum.

Even the atomic beam start to see a weak pump field in this time, the atoms does not make the transition because the energy level of the other states are shifted too far-off resonance to make the transition with a weak pump field. Therefore, the state vector $|\Psi\rangle$ still stays along the states $|1\rangle$ and $|a^0\rangle$ but there is just a small amount of deviation due to the weak pump beam. After passing through the maximum intensity of the Stokes field, the atomic beam sees an increasing pump- and a decreasing Stokes- intensity. In other words, the mixing angle Θ increases. The state vector $|\Psi\rangle$ departs from the state $|1\rangle$ and moves toward state $|-3\rangle$ followed the evolution of state $|a^0\rangle$ adiabatically. As long as the coupling is based on sufficient Rabi frequencies, the motion of the state vector $|\Psi\rangle$ keeps close to the state $|a^0\rangle$ and this results in complete population transfer from the initial state $|1\rangle$ to the final state $|3\rangle$. By contrast, insufficient coupling causes the state vector $|\Psi\rangle$ to deviate from the state $|a^0\rangle$ and populates the leaky state $|2\rangle$.

5.4 Conditions for Adiabatic Following

For efficient population transfer, the adiabatic condition needs to be fulfilled as mentioned above. In the basis of the dressed states, the Schrödinger equation for the state vector $|\Psi\rangle$ is expressed in the following form [90]:

$$ih\frac{\partial}{\partial t}\begin{pmatrix} c^{+}(t) \\ c^{0}(t) \\ c^{-}(t) \end{pmatrix} = \frac{\hbar}{2}\begin{pmatrix} \Omega_{eff}\cot\varphi & 2i\dot{\theta}\sin\varphi & 2i\dot{\varphi} \\ -2i\dot{\theta}\sin\varphi & 0 & -2i\dot{\theta}\cos\varphi \\ -2i\dot{\varphi} & 2i\dot{\theta}\cos\varphi & -\Omega_{eff}\tan\varphi \end{pmatrix}\begin{pmatrix} c^{+}(t) \\ c^{0}(t) \\ c^{-}(t) \end{pmatrix} \tag{5.17}$$

Here $|\Psi\rangle = c^{+}|a^{+}\rangle + c^{0}|a^{0}\rangle + c^{-}|a^{-}\rangle$ and $\Omega_{eff} = \sqrt{\Omega_P^2 + \Omega_S^2}$. The condition for adiabatic following requires that the system should remain in $|a^0\rangle$ after the passage if it is initially prepared in $|\Psi(0)\rangle = |a^0\rangle$, that is, $c^0(0) = 1$. Thus the coupling between state $|a^0\rangle$ and either the states $|a^+\rangle$ or $|a^-\rangle$ should remain negligible during the passage. If the off-diagonal elements of the Hamiltonian in Eq.(5.17) are zero, then there is no coupling between the coefficients c^0 and $c^{\pm}$. Especially, we can set the experimental condition to the one-photon resonance, $\Delta = 0$. Then, we have $\varphi = \pi/4$ by the Eq.(5.15). Now the coupling term $2i\dot{\theta}\sin\varphi$ is negligible, provided that $\dot{\theta}$ is much smaller than the field-induced energy splitting Ω_{eff}, that is, $\dot{\theta} \ll \Omega_{eff}$. Using Eq.(5.15), we deduce the condition for adiabatic following explicitly in terms of Rabi frequencies:

$$\left|\dot{\theta}\right| = \left|\frac{\dot{\Omega}_P\Omega_S - \Omega_S\dot{\Omega}_P}{\Omega_P^2 + \Omega_S^2}\right| \ll \Omega_{eff} \tag{5.18}$$

As long as this condition is satisfied during the passage, non-adiabatic coupling of the state $|a^0\rangle$ to the states $|a^{\pm}\rangle$ is small, and efficient population transfer is possible. Consider the atomic beam passing through the spatially overlapped area of two Gaussian shaped Stokes and pump fields during the time period T, and take a time average of $\dot{\theta}$ during this time period T. We have $\left\langle\dot{\theta}\right\rangle_{av} = \pi/2T$.

Combining this result with Eq.(5.18) leads

$$\Omega_{eff}T \gg 1 \tag{5.19}$$

It has been suggested that $\Omega_{eff}T > 10$ is appropriate for efficient population transfer based on the results of several experiments and simulations [90].

5.5 STIRAP Results

Consider the decay rate Γ_i which describes the decay from level i primarily due to spontaneous emission. In the presence of decay, one has to account for irreversible population loss by including complex energies in the Hamiltonian in Eq.(5.12) which then becomes under the two-photon resonance ($\Delta_P = \Delta_S$) condition

$$H(t) = \frac{\hbar}{2}\begin{pmatrix} 0 & \Omega_P(t) & 0 \\ \Omega_P(t) & 2\Delta - i\Gamma_2 & \Omega_S(t) \\ 0 & \Omega_S(t) & -i\Gamma_3 \end{pmatrix} \tag{5.20}$$

It is necessary to know the Rabi frequencies for the corresponding transitions to obtain numerical values for the probability of the excitation of a He^* atom into a Rydberg state. The Rabi frequency is related to the peak intensity of the applied light field by $\Omega = \frac{\mu}{\hbar}\sqrt{\frac{2I}{\varepsilon_0 c}}$ (μ : transition dipole moment) as well described in Chapter 1, and the conversion relations for the He^* transitions $2^3S_1 \rightarrow 3^3P_2 \rightarrow 26^3S_1$ are presented in Table 5.1.

Transitions	$2^3S_1 \rightarrow 3^3P_2$	$3^3P_2 \rightarrow 26^3S_1$
$m = 0$	$\Omega_P(0) = 1.78 \times 10^2\sqrt{I_P}$ MHz	$\Omega_S(0) = 0.117 \times 10^2\sqrt{I_S}$ MHz
$m = \pm 1$	$\Omega_P(1) = 1.54 \times 10^2\sqrt{I_P}$ MHz	$\Omega_S(1) = 0.1 \times 10^2\sqrt{I_S}$ MHz

Table 5.1: Conversions from intensities to Rabi frequencies (I_P and I_S are expressed in W/cm^2)

The time evolution of the numerically calculated population is illustrated in Figure 5.8 for the Rabi frequencies $\Omega_P(0) = 35$ MHz and $\Omega_S(0) = 40$ MHz. The atomic velocity was chosen to be 1500 m/s, the beam waist for both laser beams was assumed to be 1mm, and the delay time between the two beams was 1.4 μs. The $\Omega_P(t)$ and $\Omega_S(t)$ time dependence are represented by Gaussian pulses : $\Omega_P(t) = \Omega_P(0)\exp\left[-(t/10^{-6} - 6)^2\right]/2$ and $\Omega_S(t) = \Omega_S(0)\exp\left[-(t/10^{-6} - 4.6)^2\right]/2$. The decrease in the number of atoms after reaching the maximum probability 1 is the effect of the decay rate Γ.

The effect of the intermediate-level detuning Δ on the efficiency of the STIRAP was also numerically calculated and is shown in Figure 5.9. The transfer efficiency decreases as the detuning increases because of the deteriorating adiabaticity, as can be seen from Eqs.(5.15) and (5.17)

Using the configuration shown in Figure 3.5, the magnitude of the STIRAP signal was monitored with our ion detector while the field plates were scanned through the Stark energy levels (Figure 5.10). The pump (blue) and Stokes (red) laser beams were focused onto the atomic beam with cylindrical lenses

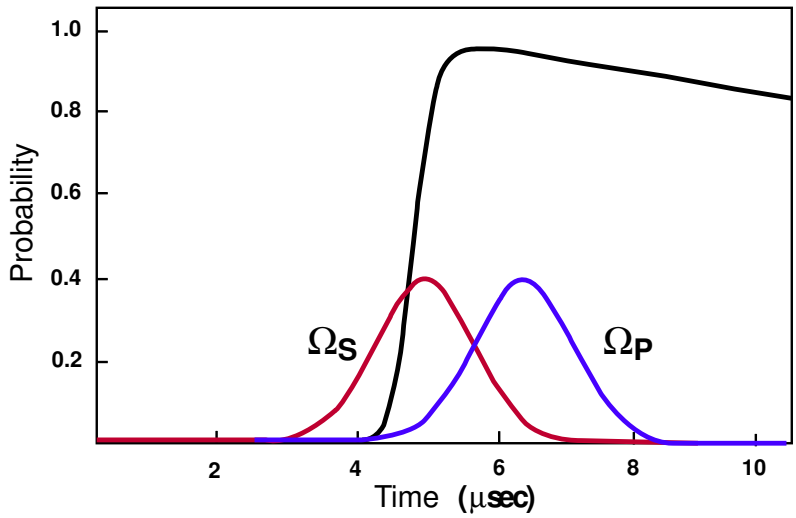

Figure 5.8: Time evolution of the numerically calculated population in a Rydberg state. The curves labelled Ω_P and Ω_S represent the time dependence of the pump field and the Stokes field, respectively.

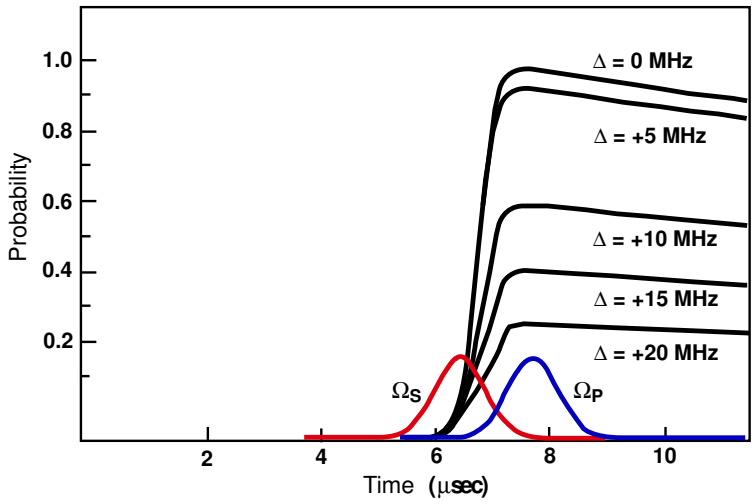

Figure 5.9: Excitation probability for different detunings of the two-photon excitation.

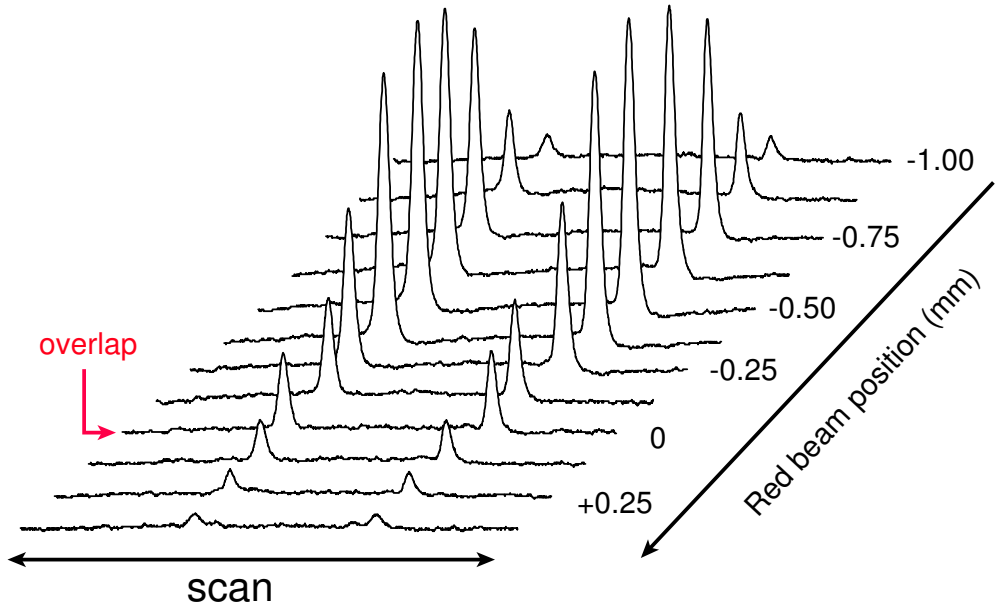

Figure 5.10: Ion signal from the Rydberg states against the Red (Stokes) beam position. Negative (positive) position corresponds to the Red (Blue) beam coming ahead and the overlap position is zero.

(f = 400 mm for red and f = 800 mm for blue) to a Gaussian waist of 400 μm and 600 μm, respectively. The long axes aligned perpendicular to the atomic beam axis were 1.5 mm (red) and 2.0 mm (blue). The focal position of the red beam with respect to that of the blue beam was varied along the atomic beam axis. We use a co-propagating beam configuration using a dichroic mirror which is high-reflection coated for the red beam and anti-reflection coated for the blue beam. The Rabi frequencies Ω_P and Ω_S were matched approximately at the value of 35 $\sim$ 40 MHz. In experimental reality the maximum population transfer was achieved when the separation of the two beams was $\sim$ 0.4 mm. This corresponds to an interaction time of $\sim$ 0.25 μs for an atomic velocity

of 1500 m/s, and we get $\Omega_{eff}T = 13 \pm 2$. Thus, the adiabatic condition given in Eq.(5.19) was fulfilled. From Figure 5.10 it is obvious that the efficiency in the STIRAP configuration is much higher than in the overlapping beam configuration.

5.6 Autler-Townes(AT) Effect

Since Autler and Townes first observed the splitting of an absorption line in OCS (carbonyl sulphide) into a doublet when applying an rf-field in 1955 [91], the AT effect has been extensively studied in atoms and molecules [92, 93]. In this experiment, a strong 389 nm pump laser induces an AT splitting, and we can measure the separation of the doublet, which corresponds to the Rabi frequency of the pump laser, by employing the red laser as a probe.

5.6.1 Theory of the Autler-Townes Effect

Systems in a strong optical field are best described in the dressed atom picture [94]. The total Hamiltonian consists of three parts: the atomic part, which gives the atomic energy levels, the radiation part whose eigenvalues are $E_n = (n + 1/2)\,\hbar\omega_l$ (ω_l : radiation field frequency), and the atom-field interaction part [2].

Consider the energy level diagram of the atomic and the radiation part as shown in Figure 5.11. If we express the states associated with these two parts as $|\text{atom} , \text{photon}\rangle$, then the states **A**, **B**, and **C**, for example, can be represented by $|1 , n-1\rangle$, $|2 , n-1\rangle$, and $|1 , n\rangle$, respectively. State **A** in the

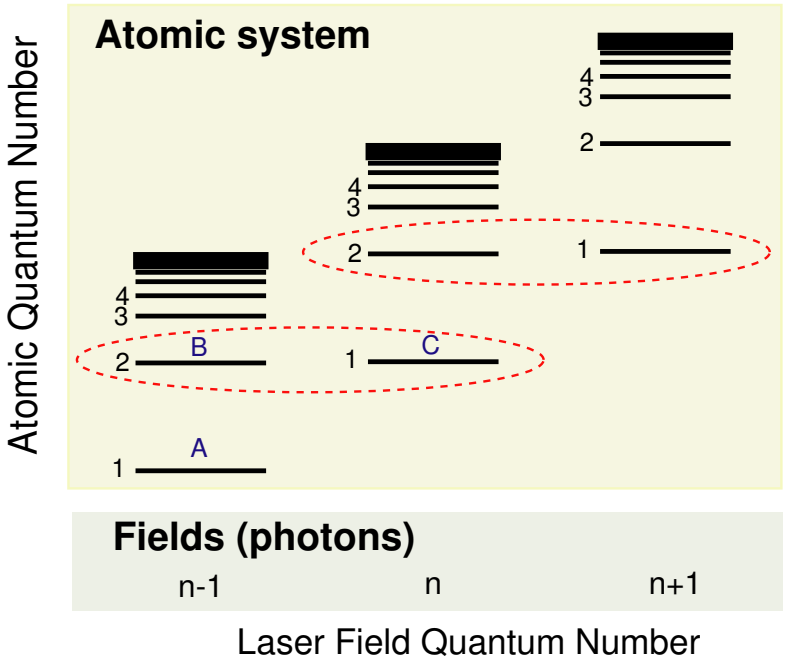

Figure 5.11: Atom-Field system energy diagram. Ref. [2]

(n-1)-photon column is raised to state **C** in the n-photon column by one photon of energy $\hbar\omega_l$. In Figure 5.12(a), the 389 nm laser field couples two atomic states $|1\rangle$ and $|2\rangle$ with a detuning Δ. Therefore, a closely spaced pair of one excited state $|2, n-1\rangle$ and one ground state $|1, n\rangle$ separated by $\hbar\Delta$ is formed, as shown in Figure 5.12(b). The atom-field interaction part couples the states $|2, n-1\rangle$ and $|1, n\rangle$ through the off-diagonal matrix elements of the Hamiltonian, and splits the energy levels farther apart to $\left(\Omega_{eff} = \sqrt{\Omega_P^2 + \Delta^2}\right)$.

Consider the three-level ladder system shown in Figure 5.12(a). The states $|1\rangle$ - $|2\rangle$ are coupled by a strong 389 nm pump field, and a weak field couples the states $|2\rangle$ - $|3\rangle$. Then the dressed states are given by

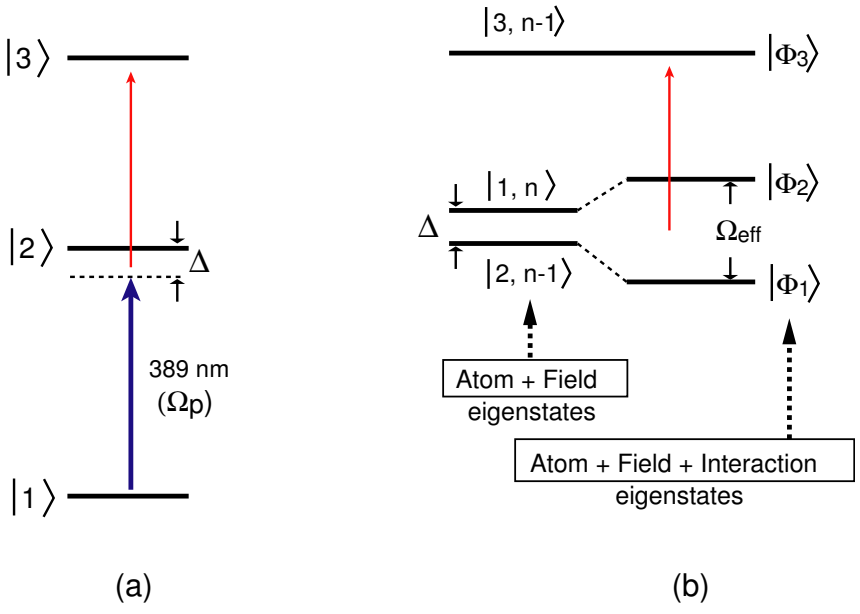

Figure 5.12: Autler-Townes effect in dressed picture

$$
\begin{aligned}
|\Phi_1\rangle &= \cos\theta\,|1,n\rangle - \sin\theta\,|2,n-1\rangle \\
|\Phi_2\rangle &= \sin\theta\,|1,n\rangle + \cos\theta\,|2,n-1\rangle \\
|\Phi_3\rangle &= |3,n-1\rangle
\end{aligned}
\tag{5.21}
$$

The mixing angle θ is defined by $\tan 2\theta = \Omega_P/\Delta$ the same way as in Eq. (5.10) and the eigenvalues of these dressed states depend on the Rabi frequency of the $|1\rangle$ - $|2\rangle$ transition, Ω_P, and on the detuning Δ:

$$
\begin{aligned}
\varepsilon_1 &= -\frac{\hbar}{2}\left(\Delta + \sqrt{\Omega_P^2 + \Delta^2}\right) \\
\varepsilon_2 &= -\frac{\hbar}{2}\left(\Delta - \sqrt{\Omega_P^2 + \Delta^2}\right) \\
\varepsilon_3 &= \delta
\end{aligned}
\tag{5.22}
$$

where δ is the detuning of the probe field. Eqs.(5.21) and (5.22) shows that a

probe field induced transition between the state $|\Phi_3\rangle$ and the dressed state $|\Phi_j\rangle$ occur when the probe detuning δ is chosen to satisfy the resonance condition $\delta = \varepsilon_j$ for $j = 1, 2$. Note that because $\varepsilon_2 > \varepsilon_1$, resonance with $|\Phi_2\rangle$ occurs for shorter δ than resonance with $|\Phi_1\rangle$, i.e., the $|\Phi_2\rangle$ resonance peak appears at the red-side of probe detuning.

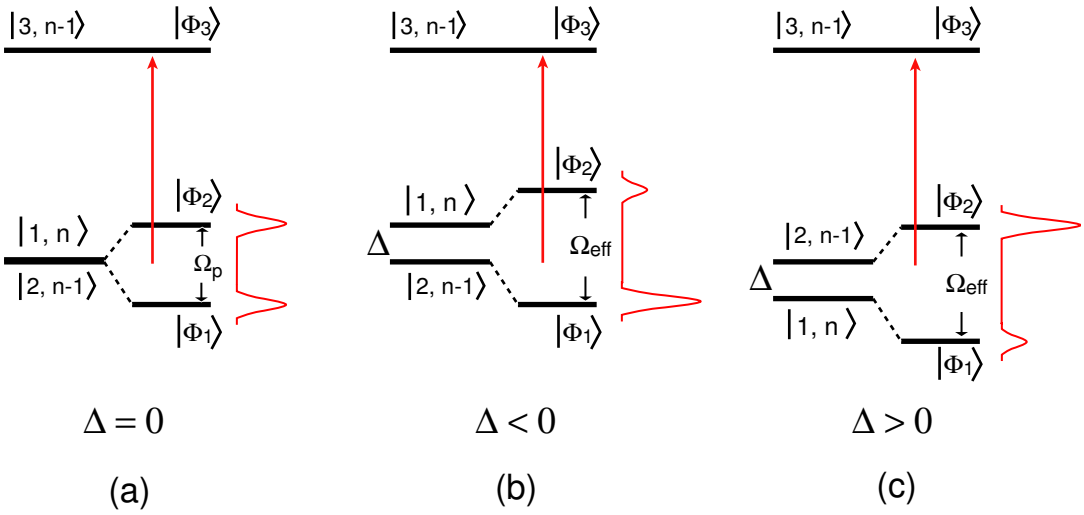

Figure 5.13: Detuning dependence of the Autler-Townes splitting. (a) resonance (b) red-detuning (c) blue-detuning.

For a zero detuning of pump field (see Figure 5.13(a)), the separation between two peaks, $\varepsilon_2 - \varepsilon_1$, is the Rabi frequency Ω_P. Thus the minimum separation of the doublet peaks corresponds to the Rabi frequency of the pump field. For large negative Δ ($\theta \approx \pi/2$) the resonance with state $|\Phi_1\rangle$, which is here predominantly level $|2, n-1\rangle$ as shown in Figure 5.13(b), occurs for $\delta \approx 0$, while resonance with state $|\Phi_2\rangle$ (predominantly level $|1, n\rangle$) occurs for $\delta \approx \Delta$. When Δ is large and positive ($\theta \approx 0$) as shown in Figure 5.13(c), the resonance at $\delta \approx 0$ is associated with state $|\Phi_2\rangle$.

5.6.2 Observed Autler-Townes Effect

The experiments were performed in the same setup with the STIRAP experiment. The He$*$ atomic beam axis crosses the axes of two co-propagating laser beams at right angles. The axes of the two laser beams coincide, but the sizes of two laser beams are different: the waists were 1 mm, 0.4 mm, and the heights 2 mm, 1.5 mm, for blue and red, respectively. The power of the pump field was 40 mW ($\Omega_P \sim 35$ MHz) and the probe field power was 50 mW ($\Omega_S \sim 3$ MHz). To detune the pump field we tilt the direction of pump beam instead of tuning the laser frequency itself [see Appendix C].

The excitation signals were obtained by monitoring the ion signal while both laser frequencies were locked to the corresponding transitions while the field plates were scanned through the Stark energy levels. Figure 5.14 shows the experimental results.

As discussed in the previous section, each of two peaks appearing in the ion signals can be attributed to a transition induced by the probe field between the 2^3S_1 Rydberg state and one of two dressed states $|\Phi_1\rangle$ or $|\Phi_2\rangle$. Since the dressed states are constructed as superposition of state 2^3S_1 and 3^3P_2 with relative composition that depends on the strength of the pump field as parameterized by a mixing angle θ, the intensities of the doublet peaks depends on the detuning of the pump field.

When the power of the probe field were increased up to 300 mW, whose Rabi frequency is comparable to that of the pump field, the coupling effect to the Rydberg states needs to be considered and this effect causes more complicated dressed states. As shown in Figure 5.15, the third satellite peak,

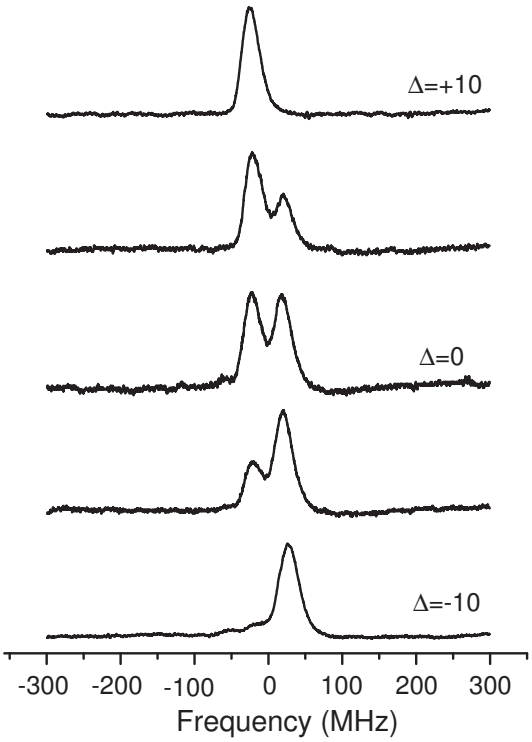

Figure 5.14: Experimental measurement of Autler-Townes splitting

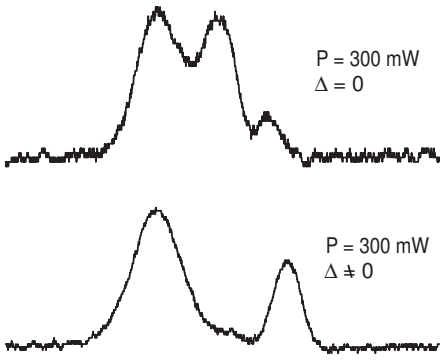

Figure 5.15: Strong Probe beam effect

which is other than $|\Phi_1\rangle$ and $|\Phi_2\rangle$, appears for $\Delta = 0$. When the pump field was detuned the dressed energy levels were shifted and it seems that $|\Phi_2\rangle$ was shifted to the side of the state at satellite peak.

Chapter 6

Focusing the Helium Atomic Beam

6.1 General Background

Atomic beams can be manipulated in inhomogeneous electric fields due to the interaction of the electric field gradient with the induced electric dipole moment of the atoms [95]. The dipole force acting on an atom in an inhomogeneous electric field $\mathbf{E}$ can be expressed as [96]

$$\mathbf{F} = (\mathbf{p} \cdot \nabla)\mathbf{E} = \frac{\alpha}{2} \nabla |\mathbf{E}|^2 \tag{6.1}$$

where $\mathbf{p}$ and α are the dipole moment and the polarizability of the atom, respectively. From $\mathbf{F} = -\nabla U$, the Stark potential energy of a ground-state atom is given by

$$U = -\frac{\alpha}{2} |\mathbf{E}|^2 \tag{6.2}$$

This shows that the force on ground state atoms exposed to an electric field gradient is always directed towards the stronger field, and it is thus impossible to focus an atomic beam with a thin electrostatic lens with a rotational symmetry around the atomic beam axis [97]. To focus ground state atoms in both

transverse directions, therefore, at least two lenses in an alternating gradient configuration are required [95]. Consider the atomic beam propagating in the z-direction. The focusing (defocusing) in the first lens is in the same direction as the defocusing (focusing) in the second lens. Thus the focusing in both transverse directions (x- and y- directions) is achieved, but there is imperfect ratio of focusing in two directions because of unequal magnification through two lenses. In order to compensate unequal magnification the third lens is required [98]. Using an electrostatic lens with three focusing elements in an alternating gradient configuration, the imaging of a neutral atomic beam has been demonstrated [95, 98]. Due to the small polarizability α (on the order of 10^{-39} Fm^2), at least a few kV of electric potential had to be applied to an electrostatic lens in these experiments.

In our experiment, we take advantage of the relatively large polarizability of Rydberg atoms, which scales with the principal quantum number as $\sim n^7$ (Table 4.1). Thus, moderate electric field gradients are sufficient to focus a beam of Rydberg atoms in the same configuration as used in Ref. [95, 98].

6.2 Electrostatic Hexapole Lens

In order to focus Rydberg helium atoms, we designed an electrostatic hexapole lens, which consists of six electrodes instead of using three pairs of electrodes along the beam axis as shown in Figure 6.1. This configuration produces a field gradient that increases linearly with the distance from the center of the hexapole.

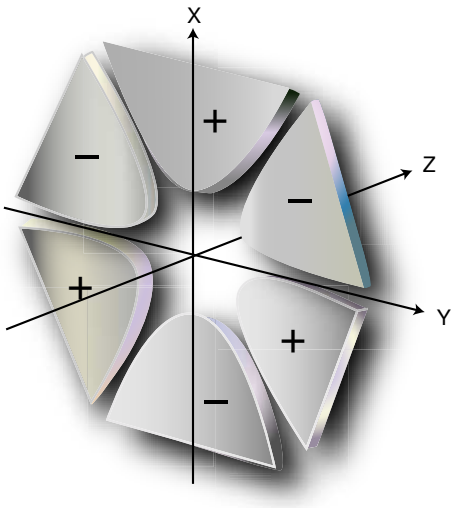

Figure 6.1: Electrostatic hexapole lens. The atomic beam propagates in the z-direction.

In cylindrical coordinates, the electrostatic potential can be expressed as the following multipole expansion [99]:

$$U(r,\theta) = -E_0 r_0 \left[\sum_{n=1}^{\infty} \frac{a_n}{n} \left(\frac{r}{r_0} \right)^n \cos(n\theta) + \sum_{n=1}^{\infty} \frac{b_n}{n} \left(\frac{r}{r_0} \right)^n \sin(n\theta) \right] \tag{6.3}$$

where E_0 is the central field, r_0 is a scaling length, and a_n (b_n) are the expansion coefficients. $r = \sqrt{x^2 + y^2}$ is the radial distance from the symmetric center, and $\theta = \tan^{-1}\left(\frac{y}{x}\right)$. The $n = 1$ terms in Eq.(6.3) represent a constant electric field, while the $n = 2$ and $n = 3$ terms are the quadrupole and hexapole fields. To achieve the symmetric magnitude of the field under reflection on the x- and y- axes, we can set $b_n = 0$. For hexapole fields ($n = 3$), Eq.(6.3) can be simplified to

$$U(r,\theta) = -U_0 \left(\frac{r}{r_0} \right)^3 \cos 3\theta \tag{6.4}$$

where $U_0 = E_0 r_0 \frac{a_3}{3}$. Assuming that the induced dipole moment $\mathbf{p}$ is parallel

to the electric field and independent of the field strength leads to the force acting on a dipole **p** in the hexapole field from Eq.(6.4)

$$\mathbf{F} = -\frac{6pU_0}{r_0^3}\mathbf{r} \tag{6.5}$$

Thus, the magnitude of the radial force is proportional to the distance from the beam axis. That is, the trajectory of the atoms is governed by an equation for harmonic motion with the spring constant $k = \frac{6pU_0}{r_0^3}$. Figure 6.2 shows the plot of equipotential lines for the hexapole electric field.

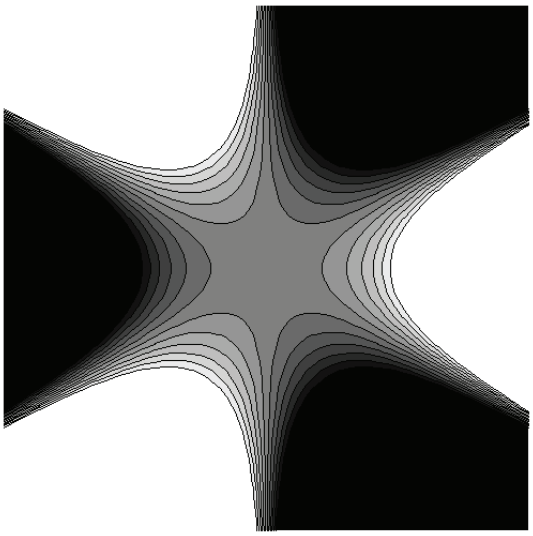

Figure 6.2: Equipotential lines for the hexapole electric field

Consider an atom with mass m and velocity v passing through the electrostatic lens during a time interval Δt $(= s/v)$ as shown in Figure 6.3. Momentum conservation yields

$$F\Delta t = mv\sin\alpha \tag{6.6}$$

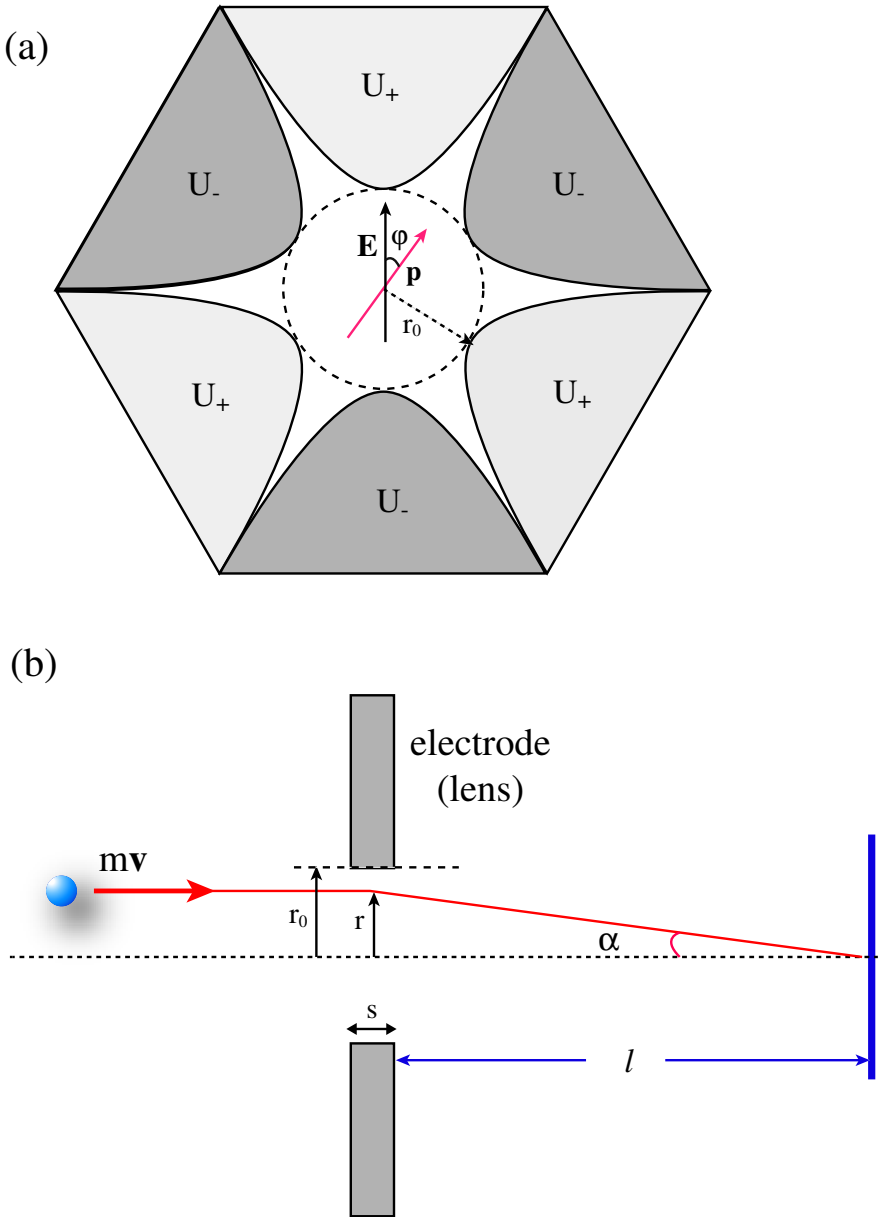

Figure 6.3: (a) Cross section of the hexapole lens (b) Atomic trajectory passing through the hexapole lens

Using Eqs.(6.5) and (6.6), the focal-plane position l can be expressed as

$$l = \frac{mv^2 r_0^3}{6spU_0}, \tag{6.7}$$

where r_0 and s are the internal radius and length of the hexapole lens, respectively. U_0 is the hexapole rod voltage. Eq.(6.7) shows that the focal position does not only depend on atomic properties (m, v, p) but also on the lens parameters (s, r_0, U_0).

Considering Figure 6.3(a) and Eq.(6.1) gives

$$\cos\varphi \propto \frac{6pU_0}{r_0^3}, \tag{6.8}$$

where φ is the angle between the electric dipole moment $\mathbf{p}$ and the electric field $\mathbf{E}$. Thus, the direction of $\mathbf{p}$ when passing the hexapole lens determines if the beam is diverging or conversing.

6.3 Experimental Results

To ensure an effective interaction between Rydberg atoms and the field created by the electrostatic lens, the distance between the interaction region and the lens had to be chosen carefully. Considering the lifetime ($\tau \sim 40\ \mu s$) and the longitudinal velocity ($v_l \sim 1500\ m/s$) of the He^* atomic beam in the n=26 Rydberg state, for example, it is obvious that the distance must be less than 6 cm. Once the Rydberg signal has been observed with the ion detector, the electric potentials, U_+ and U_- in Figure 6.3(a), are adjusted to find the values which give the brightest image on the phosphor screen detector. An image taken during the experiment and intensity profiles of the image along

two transverse directions (x and y axes) are illustrated in Figure 6.4. The image in Figure 6.4(a) shows the atomic beam profile when the red beam was turned off. Figure 6.4(b) is the image when the Rydberg atoms were created by the two- photon transition, where the applied potentials were $U_+ = 211$ V and $U_- = 0$ V. The intensity profiles of the focused He^* beam are plotted in the horizontal (x-axis) and vertical (y-axis) directions as shown in Figure 6.4(c) and (d). The values in FWHM (Full Width at Half Maximum) along the x- and y-axes are about 0.6 mm and 3 mm, respectively.

We assume that the asymmetric shape of the focused spot is caused by the profile of thermal atomic beam passing through the field plates (dimensions in Figure 3.5). Even if the image of the atomic beam in Figure 6.4(a) has a longer side along the y-axis due to the rectangular shape of slit (0.5 mm $\times$ 2 mm longer side in the y-axis), most of the atoms which are vertically spread by no more than the height of the field plates ($\sim$ 5.7 mm) and might thus be cut in the outlet of the field plates. But the spread in the x-axis is opened due to the open-side of the field plates. Thus, the shape of the atomic beam passing through the electrostatic lens can be almost rectangular whith a height of $\sim$ 5.7 mm and a width much larger than its height. The overall spot size may also depend on the velocity distribution which causes the chromatic aberrations as explained the above. Therefore, a laser cooled atomic beam can guarantee a brighter (a colder temperature) spot through minimizing chromatic aberrations and the spread of the atomic beam. Figure 6.4(e) explains why the focused spot is not located in the center of the atomic beam. A surface plot of the focused beam is presented in Figure 6.5.

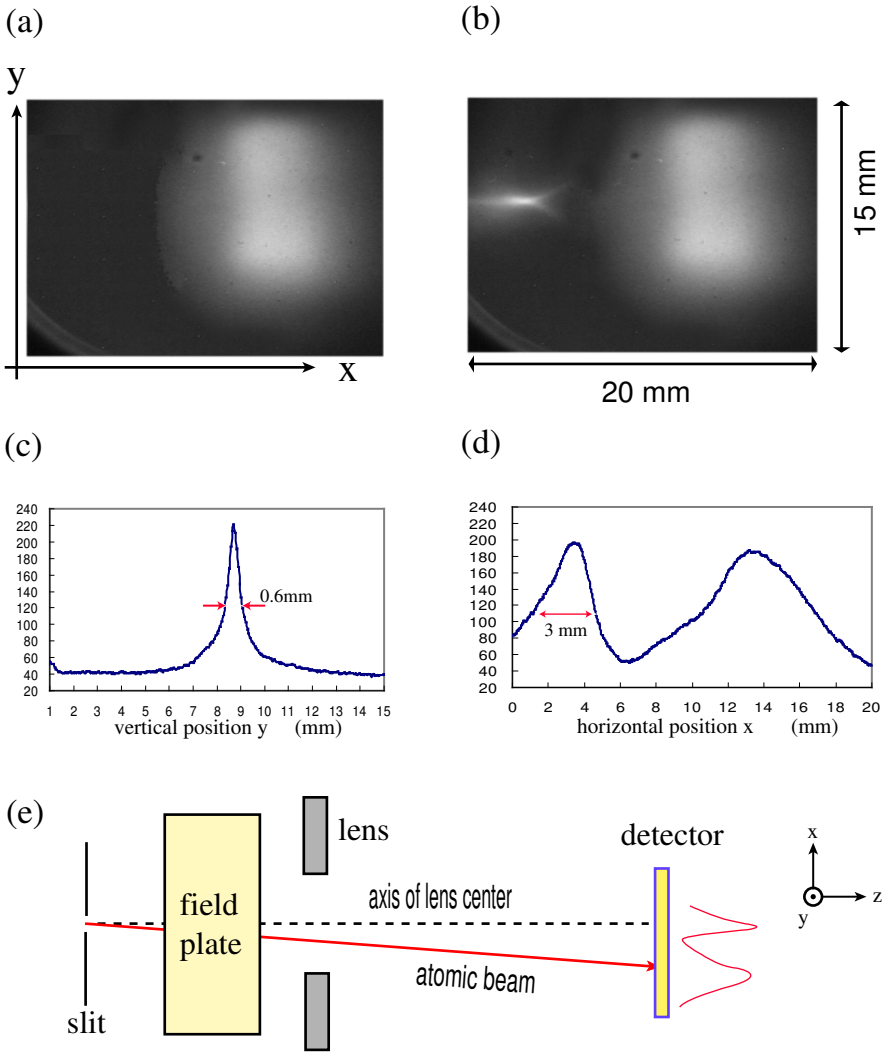

Figure 6.4: Experimental results on the focusing of He* atomic beam: (a) Red laser-off (b) Red laser-on (c) plot of the focused beam along the y- direction (d) plot of the focused beam and the atomic beam along the x-direction (e) atomic beam geometry

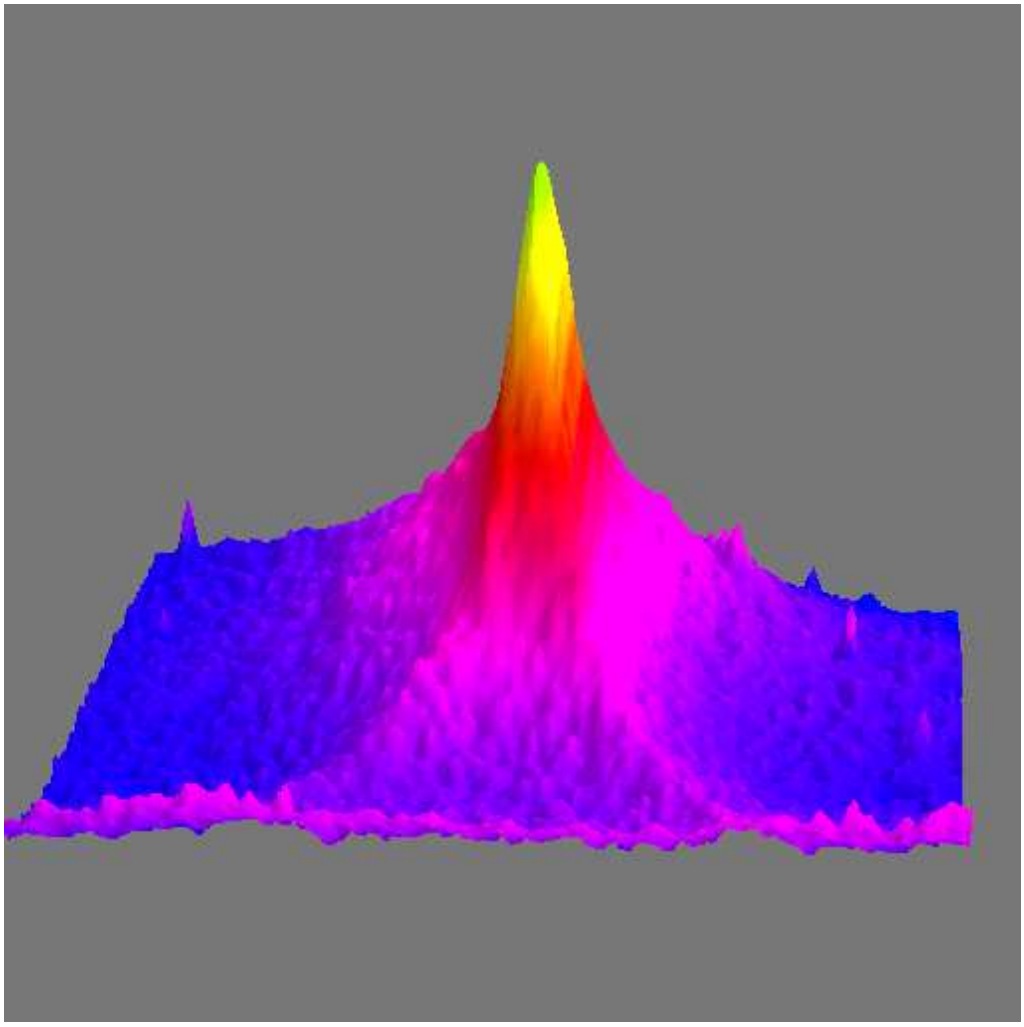

Figure 6.5: Profile of focused atomic beam

Chapter 7

Conclusion

Precise control of atomic beams on the near-atomic scale is a crucial matter in atom optics research. The goal of this experiment was to produce and focus a high flux He^* atomic beam. In order to do so, we used the STIRAP excitation technique to efficiently create Rydberg atoms and take advantage of the strong dipole interaction between electric fields and the Rydberg atoms.

Due to their different oscillator strengths, the Rydberg states give different transition strengths, and thus we investigated the transition strengths for the n = 26 Stark energy levels. Ultimately, the STIRAP excitation to the 26^3S_1 Rydberg state was the best choice to achieve an efficient population transfer.

The Autler-Townes effect has been observed resulting in a measurement of the Rabi frequencies of the lasers. Since STIRAP critically depends on the Rabi frequencies. this measurement helped to optimize the choice of the the Rabi frequencies and the beam sizes of the two laser beams for efficient STIRAP excitation.

We have built an electrostatic hexapole lens to focus the Rydberg He atomic

beam, and we observed a focused bright spot on our phosphor screen detector. This result promises future control of the beam position since various combinations of different voltages can be applied to each of the hexapole electrodes to move the focal point of the lens.

As a future plan, the He^* atomic beam can be used to do neutral atom lithography in a direct deposition mode, where He^* atoms with a high internal energy are focused by the electrostatic lens to an extremely fine spot and deposited onto a substrate, or in a lithography mode, where the focused He^* atoms are used to expose a suitable resist material. With all these potential applications, it is apparent that Rydberg atom optics using a He^* atomic beam can provide some new tools for manipulation of matter on the near-atomic scale.

Appendix A

Atomic Units

Quantity	Definition in atomic units	Value
Charge (e)	Charge of the electron	$1.60218 \times 10^{-19}\ C$
Mass (m)	Mass of the electron	$9.108 \times 10^{-28}\ g$
Length (a_0)	Radius of Bohr orbit ($\hbar^2/me^2$)	$5.2917 \times 10^{-9}\ cm$
Velocity (v_0)	Electron velocity in Bohr orbit ($e^2/\hbar = \alpha c$)	$2.1877 \times 10^{8}\ cm/s$
Energy (e^2/a_0)	Twice the ionization energy of H	$27.2112\ eV$
Frequency	$v_0/a_0 = me^4/\hbar^3 = 4\pi R_y$	$4.1341 \times 10^{-16}\ sec^{-1}$

Table A.1: Taken from Ref.[66]. (H : hydrogen)

Appendix B

Spectroscopy Data for $2^3S_1 \rightarrow 3^3P_2$ Transition

Quantity	Value
Excited state lifetime (τ)	106.83 ns
Transition Linewidth ($\Gamma/2\pi$)	1.49 MHz
Saturation Intensity ($I_s = \pi hc/3\lambda^3\tau$)	3.31 mW/cm^2
Capture velocity ($v_c = \Gamma/k$)	0.58 m/s
Recoil velocity ($v_r = \hbar k/M$)	25.6 cm/s
Doppler limit ($v_D = \sqrt{k_B T_D/M}$)	27.25 cm/s

Table B.1: Doppler Temperature $T_D = \hbar\Gamma/2k_B$, mass M = 6.646×10^{-27} kg, $k = 2\pi/\lambda$ ($\lambda = 388.98$ nm), all data taken from Ref.[2].

Appendix C

Calibration for Optical Molasses

A configuration of counterpropagating laser beams which is known as *optical molasses* [2] has been used for laser cooling of atoms. The total radiation pressure force on an atom in the low intensity regime ($I/I_s < 1$, I_s : saturation intensity) is given by [2]

$$F(v) = \hbar k \frac{\Gamma}{2} \frac{I/I_s}{1 + [\frac{2(\Delta - \mathbf{k}\cdot\mathbf{v})}{\Gamma}]^2} - \hbar k \frac{\Gamma}{2} \frac{I/I_s}{1 + [\frac{2(\Delta + \mathbf{k}\cdot\mathbf{v})}{\Gamma}]^2} \tag{C.1}$$

where Δ is the detuning of the laser frequency from the atomic resonance, and the *Doppler shift* ($\mathbf{k}\cdot\mathbf{v}$) depends on the propagating direction of the laser light ($\mathbf{k}$) and the direction of atomic motion ($\mathbf{v}$).

The plot in Figure C.1(a) shows that $F(\hbar k\Gamma)$ is nearly linear with velocity for $|v| < \Gamma/2k$, so it is convenient to define a *capture velocity* as shown in Table B.1. For example, the capture velocity is calculated as $v_c = 4\Gamma/2k$ for $\Delta = 4\Gamma$ and this corresponds to $9.2v_r$ for the 389 nm transition. This can be easily calculated by the relation:

$$\frac{\Gamma}{k} = \frac{\Gamma}{2\pi/\lambda} = \lambda \cdot (\frac{\Gamma}{2\pi}) = (389 \times 10^{-9}\ \text{m})(1.49 \times 10^{6}\ /\text{s}) = 0.58\text{m/s} \tag{C.2}$$

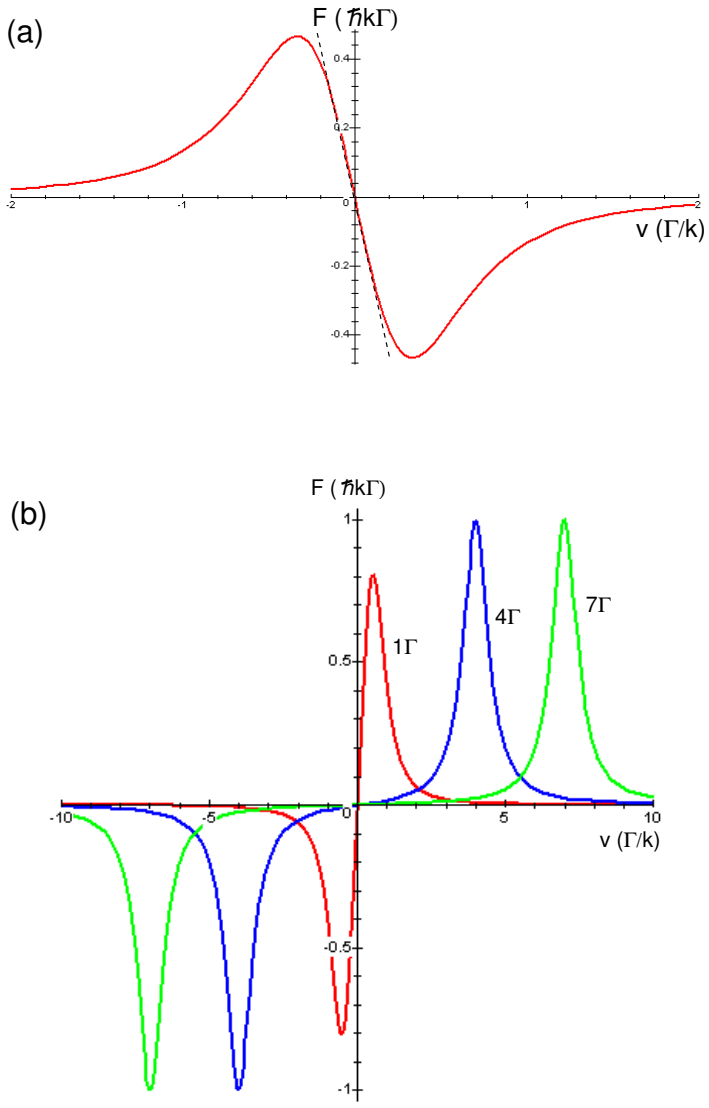

Figure C.1: Plot of total radiation pressure force *vs.* velocity for (a) red detuning and (b)three different blue detunings

This value corresponds to 2.3 v_r because the recoil of one 389 nm photon leads to a change of 25.6 cm/s in atomic velocity [see Table B.1]. We can also estimate the Doppler shift created by one photon recoil as

$$\Delta\omega_D = 2\pi \cdot \nu_D = kv_r = (2\pi)\frac{25.6 \text{ cm/s}}{0.0389 \times 10^{-3} \text{ cm}} = (2\pi) \cdot 658 \text{ kHz} \qquad \text{(C.3)}$$

If our atomic beam with a longitudinal velocity v_l of $\sim$ 1500 m/s passes through the 389 nm laser beam orthogonally and is deflected by 3 mm on the screen located 2 m downstream from the interaction region, then this corresponds to a shift of 2.25 m/s in transverse velocity. From Eq.C.3, the corresponding Doppler shift is $(2\pi) \times 5.8$ MHz, which is 3.9 Γ or 8.8 v_r.

The numerical plot for the bluemolasses is also given in Figure C.1(b). Figure C.2 shows the deflection results for the different angles between the atomic beam axis and the propagation direction of the laser beam. Using the results of this deflection measurement we can utilize the detuning effect by adjusting the propagation direction of the laser beam instead of tuning the laser frequency itself.

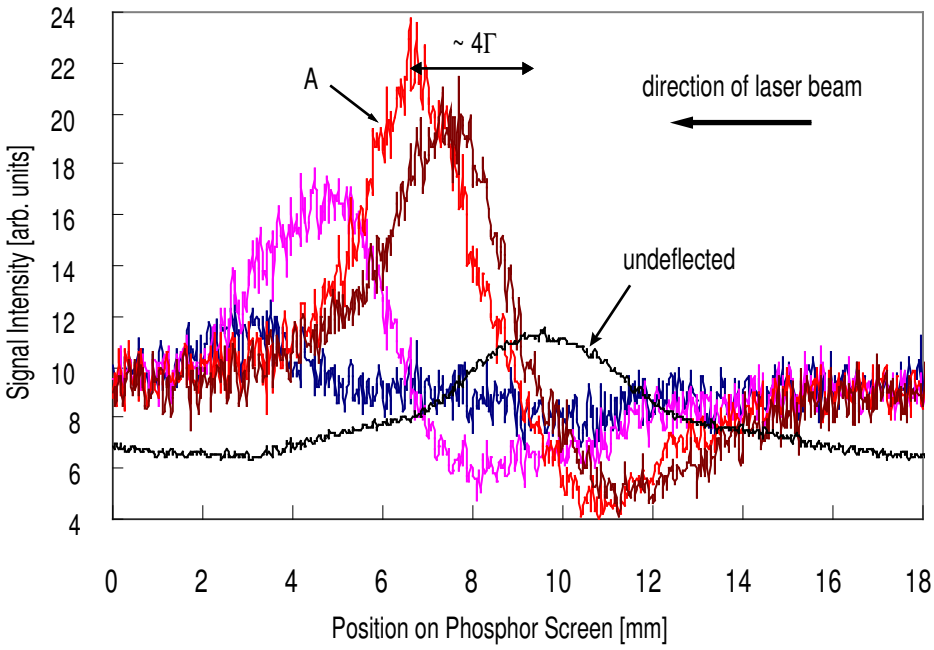

Figure C.2: Deflection of atomic beam. The peak A is deflected by ~ 3 mm which corresponds to $\sim 4\ \Gamma$

Bibliography

[1] Thomas Breeden and Harold Metcalf, *Stark Acceleration of Rydberg Atoms in Inhomogeneous Electric Fields*, Phys. Rev. Lett. **47**, 1726 (1981)

[2] H.J. Metcalf and P. van der Straten, *Laser Cooling and Trapping*, Springer, New York (1999)

[3] Pierre Meystre, *Atom Optics*, Springer-Verlag, New York (2001)

[4] L.de Broglie, *Radiations-Ondes et Quanta*, Comp. Rend. Ac. Sci. **177**, 507 (1923)

[5] C. Davisson and L.H. Germer, *Diffraction of Electrons by a Crystal of Nickel* , Phys. Rev., **30**, 705 (1927)

[6] Otto Stern, *Bending a molecular ray by crystal lattice face*, Naturwiss, **17**, 391 (1929)

[7] Han Pu, Chris Search, Weiping Zhang, and Pierre Meystre, *Atom Optics - From de Broglie Waves to Heisenberg Ferromagnets*, Fortschr. Physics. **50**, 664 (2002)

[8] Richard J. Cook and Richard K. Hill, *An electromagnetic mirror for neutral atoms*, Optics Communications. **43**, 258 (1982)

[9] Peter J. Martin, Bruce G. Oldaker, Andrew H. Miklich, and David E. Pritchard, *Bragg scattering of atoms from a standing light wave*, Phys. Rev. Lett. **60**, 515 (1988)

[10] Philip E. Moskowitz, Phillip L. Gould, Susan R. Atlas, and David E. Pritchard, *Diffraction of an Atomic Beam by Standing-Wave Radiation*, Phys. Rev. Lett. **51**, 370 (1983)

[11] D. Wineland and H. Dehmelt, *Proposed* $10^{14}\Delta\nu < \nu$ *laser fluorescence spectroscopy on* TI^{+} *mono-ion oscillator III* , Bull.Am.Phys.Soc., Ser.II, **20**, 637 (1975)

[12] T.W. Hänsch and A.L. Schawlow, *Cooling of gases by laser radiation*, Optics Communications. **13**, 68 (1975)

[13] M.H. Anderson, J.R. Ensher, M.R. Matthews, C.E. Wieman, and E.A. Cornell, *Observation of Bose-Einstein condensation in a dilute atomic vapor*, Science, **269**, 198 (1995)

[14] *Special Issue on Atom Optics* , Applied Physics B, **54**, (1992)

[15] E.W. Hagley, L. Deng, M. Kozuma, J. Wen, K. Helmerson, S.L. Rolston, and W.D.Phillips, *A Well-Collimated Quasi-Continuous Atom Laser*, Science, **283**, 1706 (1999)

[16] L. Deng, E.W. Hagley, J. Wen, M. Trippenbach, Y. Band, P.S. Julienne, J.E. Simsarian, K. Helmerson, S.L. Rolston, and W.D. Phillips, *Four-wave mixing with matter waves*, Nature, **398**, 218 (1999)

[17] M. Kozuma, L. Deng, E.W. Hagley, J. Wen, R. Lutwak, K. Helmerson, S.L. Rolston, and W.D. Phillips, *Coherent Splitting of Bose-Einstein Condensed Atoms with Optically Induced Bragg Diffraction*, Phys. Rev. Lett., **82**, 871 (1999)

[18] Yu.B. Ovchinnikov, J.H. Muller, M.R. Doery, E.J.D. Vredenbregt, K. Helmerson, S.L. Rolston, and W.D. Phillips, *Diffraction of a Released Bose-Einstein Condensate by a Pulsed Standing Light Wave*, Phys. Rev. Lett., **83**, 284 (1999)

[19] Erich Jurdik, *Laser manipulation of atoms and nanofabrication*, Katholieke Universiteit Nijmegen, Ph.D Thesis (2001)

[20] Jabez J. McClelland, *Nanofabrication via Atom Optics*, in Handbook of Nanostructured Materials and Nanotechnology, ed. by H. S. Nalwa, vol. I, (Academic Press, San Diego, CA, 2000), p. 335-385

[21] M. Partlow, *Bichromatic Collimation to make an Intense Helium Beam*, Stony Brook University, Ph.D Thesis (2004)

[22] M. Partlow, X. Miao, J. Bochmann, M. Cashen, and H. Metcalf, *Bichromatic Slowing and Collimation to Make an Intense Helium Beam*, Phys. Rev. Lett. **93**, 213004 (2004)

[23] C. Cohen-Tannoudji, J. Dupont-Roc, and G. Grynberg, *Atom-Photon Interactions*, Wiley-Interscience, New York (1992)

[24] I.I. Sobelman, *Atomic Spectra and Radiative Transitions*, Springer, Berlin (1979)

[25] P.M. Farrell and W.R. MacGillivray, *On the consistency of Rabi frequency calculations*, Journal of Physics A, **28**, 209 (1995)

[26] G.R. Woestenenk, J.W. Thomsen, M. van Rijnbach, P. van der Straten, and A. Niehaus, *Construction of a low velocity metastable helium atomic beam*, Rev. Sci. Instruments, **72**, 3842 (2001)

[27] Roeland Cornelis Maria Bosch, *Ferromagnetic Nanostructures by Laser Manipulation*, Techische Universiteit Eindhoven, Ph.D Thesis (2002)

[28] R.W. Boyd, *Nonlinear Optics*, Academic Press, San Diego, CA (1992)

[29] Jeff.S. Hack, *Laser Cooling in the Recoil Domain*, Stony Brook University, Ph.D Thesis (2001)

[30] Manfred Wohlecke, Klaus Betzler, Mirco Imlau, *Nonlinear Optics*, Opt. Comm. University of Osnabruck, Lecture Notes (2005)

[31] B.E.A. Saleh and M.C. Teich, *Fundamentals of Photonics*, John Wiley & Sons, New York (1991)

[32] Y.R. Shen, *The Principles of Nonlinear Optics*, John Wiley & Sons, New York (1984)

[33] A. Yariv, *Quantum Electronics*, John Wiley & Sons, New York (1989)

[34] P.A. Franken and J.F. Ward, *Optical Harmonics and Nonlinear Phenomena*, Reviews of Modern Physics, **35**, 23 (1963)

[35] D.A. Kleinman, *Nonlinear Dielectric Polarization in Optical Media*, Physical Review, **126**, 68 (1977)

[36] P.D. Maker, R.W. Terhune, M. Nisenoff, and C.M. Savage, *Effects of Dispersion and Focusing on the Production of Optical Harmonics*, Phys. Rev. Lett. **8**, 21 (1962)

[37] C.L. Tang, *American Optical Society Optics Handbook*, McGraw-Hill,New York (1994)

[38] J.C.J. Koelemeij, *Interaction of UV light with cold metastable helium atoms*, Vrije Universiteit Amsterdam, Ph.D Thesis (2004)

[39] C.D. Boyd and D.A. Kleimann, *Parametric Interaction of Focused Gaussian Light Beams*, J. of Appl. Phys., **39**(8), 3517 (1968)

[40] CASIX Inc., *http://www.casix.com*

[41] A. Ashkin, G.D. Boyd, J.M. Dziedzic, *Resonant optical second harmonic generation and mixing*, IEEE J. Quantum Electronics, **QE2**, 109 (1966)

[42] W.J. Kozlovsky, C.D. Nabors, and R.L. Byer, *Second-harmonic generation of a continuous-wave didode-pumped Nd:Yag laser using an externally resonant cavity*, Optics Letters, **12**, 1014 (1987)

[43] Oleg Anton Kritsun, *Atom Optics with Rydberg States in Inhomogeneous Electrc Fields*, Stony Brook University, Ph.D Thesis, (2003)

[44] TekhnoScan, *Resonant Frequency Doubler, model FD-SF-07, for CW single-frequency lasers*

[45] T.W. Hänsch and B. Couillaud, *Laser Frequency Stabilization Spectroscopy of a Reflecting Reference Cavity*, Optics Communications, **35**(3), 441 (1980)

[46] Grzegorz Lach, Krzysztf Pachucki, *Forbidden transitions in the helium atom*, Phys. Rev. A., **64**, 042510 (2001)

[47] J.R. Woodworth, H.W. Moos, *Experimental determination of the single-photon transition rate between the* 2^3S_1 *and* 1^1S_0 *states of He I*, Phys. Rev. A., **12**, 2455 (1975)

[48] Mark Feldman, *Measurement of the He* 3^3P *Fine Structure Using Time Resolved Level Crossing Spectroscopy*, Stony Brook University, Ph.D Thesis (1980)

[49] Tim Karcher, *Vacuum System Science and Engineering*, Course notes, Arizona State University (1998)

[50] J.M. Lafferty, *Foundations of Vacuum Science and Technology*, John Wiley & Sons,Inc. (1998)

[51] M. Pirani and J. Yarwood, *Principles of Vacuum Engineering*, Reinhold Publishing Corporation, New York (1961)

[52] D.W. Fahey, W.F. Parks and L.D. Schearer, *High flux beam source of thermal rare-gas metastable atoms*, Journal of Physics E : Scientific instruments, **13**(4), 381 (1980)

[53] W. Rooijakkers, W. Hogervorst, W. Vassen, *An intense collimated beam of metastable helium atoms by two-dimensional laser cooling*, Optics Communications, **123**, 321 (1996)

[54] M.J. Bellanca, *Sub-Recoil Velocity Selective Resonances in Metastable Helium*, Stony Brook University, Ph.D Thesis (1999)

[55] N.A. Surplice and R.J. D'Arcy, *Reduction in the work function of stainless steel by electric fields*, Journal of Physics F : Metal Physics, **2**, L8 (1972)

[56] R.D. Rundel, F.B. Dunning, J.S. Howard, J.P. Riola, and R.F. Stebbings, *A Gas Cell Method for the Measurement of Secondary Electron Ejection Coefficients for Metastable Atoms on Metal Surfaces*, Review of Scientific Instruments, **44**, 60 (1973)

[57] R.W. Drever and J.L. Hall, *Laser Phase and Frequency Stabilization Using an Optical Resonator*, Applied Physics B, **31**, 97 (1983)

[58] W. Demtröder, *Laser Spectroscopy: Basic Concepts and Instrumentation*, 3rd edition, Springer-Verlag Berlin Heidelberg (2003)

[59] Carl E. Wieman and Leo Hollberg, *Using diode lasers for atomic physics*, Review of Scientific Instruments, **62**(1), 1 (1991)

[60] Kilian Talo Theodor Singer, *Interactions in an ultracold gas of Rydberg atoms*, Ph.D Thesis , Albert-Ludwigs-University, (2004)

[61] Thomas.F.Gallagher, *Rydberg Atoms*, Cambridge University Press, (1994)

[62] H.E.White, *Introduction to Atomic Spectra*, McGraw-Hill,New York, (1934)

[63] W.N.Hartley, *LVI.-On homologous spectra*, Journal of the Chemical Society, Transactions, **43**, 390 (1883)

[64] J.R.Rydberg, *On the Structure of the Line Spectra of the Chemical Elements*, Phil.Mag.5th Ser, **29**,331 (1890)

[65] J.J.Sakurai, *Modern Quantum Mechanics*, Addison Wesley, (1994)

[66] H.A.Bethe and E.E.Salpeter, *Quantum Mechanics of one-and two-electron atoms*, Academic Press Inc., New York, (1957)

[67] M.J.Seaton, *Quantum defect theory*, Reports on Progress in Physics, **46**(2), 167 (1983)

[68] C.J. Lorenzen, K.Niemax, *Quantum Defects of the* $n^2P_{1/2;3/2}$ *Levels in* ^{39}KI *and* ^{85}RbI, Physica Scripta, **27**, 300 (1983)

[69] M.L.Zimmerman, M.G.Littman, M.M.Kash, Daniel Kleppner, *Stark structure of the Rydberg states of alkali-metal atoms*, Physical Review A, **20**(6), 2251 (1979)

[70] H.J.Silverstone, *Perturbation theory of the Stark effect in hydrogen to arbitrarily high order*, Physical Review A, **18**, 1853 (1978)

[71] E Luc-Koenig and A.Bachelier, *Systematic theoretical study of the Stark spectrum of atomic hydrogen*, Journal of Physics B, **13**, 1743 (1980)

[72] Peter M. Koch, *Resonant States in the Nonperturbative Regime: The Hydrogen Atom in an Intense Electric Field*, Physical Review Letter, **41**, 99 (1978)

[73] C.T.W.Lahaye and W.Hogervorst, *Stark manifolds and electric-field-induced avoided level crossing in helium Rydberg states*, Physical Review A, **39**(11), 5658 (1989)

[74] W.C.Martin, *Improved* ^4HeI *1snl ionization energy, energy levels, and Lamb shifts for 1sns and 1snp terms*, Physical Review A, **36**(8), 3575 (1987)

[75] David R. Herrick, *Sum rules and expansion formula for Stark radiative transitions in the hydrogen atom*, Physical Review A, **12**, 1949 (1975)

[76] Thomas Bergeman, Professor, Department of Physics and Astronomy, Stony Brook University, *in private communication*

[77] Andreas Stefan Gürtler, *Rydberg atoms in low-frequency fields*, Ph.D Thesis , Fom Institute for Atomic and Molecular Physics, Amsterdam, (2003)

[78] R.D.Cowan, *TheTheory of Atomic Structure and Spectra*, University of California,Berkeley, (1981)

[79] G.W.F. Drake, *Atomic, Molecular, & Optical Physics Handbook*, AIP Press (1996)

[80] K. Bergmann, H. Theuer, B.W. Shore, *Coherent population transfer among quantum states of atoms and molecules*, Reviews of Modern Physics, **70**(3), 1003 (1975)

[81] J. Oreg, F.T. Hioe, and J.H, Eberly, *Adiabatic following in multilevel systems*, Physical Review A, **29**, 690 (1984)

[82] U. Gaubatz, P. Rudecki, M. Becker, S. Schiemann, M. Kulz, and K. Bergmann, *Population switching between vibrational levels in molecular beams*, Chem. Phys. Lett. , **149**, 463 (1988)

[83] A. Einstein, *Zur Quantentheorie der Strahlung*, Physikalische Zeitschrift, **18**, 121 (1917)

[84] I.i. Rabi , *Space Quantization in a Gyrating Magnetic Field*, Phys. Rep., **51**, 652 (1937)

[85] B.W.Shore, *The Theory of Coherent Atomic Excitation*, Wiley, New York, (1990)

[86] M. Khudaverdyan, *Addressing of individual atoms in an optical dipole trap*, Diploma Thesis, U. of Bonn, (2003)

[87] J.C. Camparo and R.P. Frueholz, *A dressed atom interpretation of adiabatic rapid passage*, J.Phys.B: At. Mol. Phys., **17**, 4169 (1984)

[88] J.G. Powles, *The adiabatic fast passage experiment in magnetic resonance*, Proc. Phys. Soc., **71**, 497 (1958)

[89] J.S. Melinger, Suketu R. Gandhi, A. Hariharan, J.X. Tull, and W.S. Warren , *Generation of narrowband inversion with broadband laser pulses*, Phys. Rev. Lett., **68**, 2000 (1992)

[90] N.V. Vitanov, M. Fleischhauer, B.W. Shore and K. Bergmann , *Coherent Manipulation of Atoms and Molecules by Sequential Pulses*, Advances of Atomic, Molecular, and Optical Physics, **46**, 55 (2001)

[91] S.H. Autler and C.H. Townes, *Stark Effect in Rapidly Varying Fields*, Physical Review, **100**, 703 (1955)

[92] Jianbing Qi, Guenadiy Lazarov, Xuejun Wang, Li Li, Lorenzo M.Narducci, A.Marjatta Lyyra, and Frank C.Spano *Autler-Townes Splitting in Molecular Lithium: Prospects for All-Optical Alignment of Nonpolar Molecules*, Physical Review Letters, **83**, 288 (1999)

[93] Ruth Garcia-Fernandez, Aigars Ekers, Janis Klavins, Leonid P. Yatsenko, Nikolai N. Bezuglov, Bruce W. Shore, and Klaas Bergmann, *Autler-Townes effect in a sodium molecular-ladder scheme*, Physical Review A, **71**, 023401 (2005)

[94] C.Cohen-Tannoudji, B.Diu, and F.Laloë, *Quantum Mechanics*, New York: Wiley, (1977)

[95] Juris G. Kalnins, Jason M. Amini, and Harvey Gould, and Harvey Gould, *Focusing a fountain of neutral cesium atoms with an electrostatic lens triplet*, Physical Review A, **72**, 043406 (2005)

[96] M. Morinaga, *Focusing ground-state atoms with an electrostatic field*, Applied Physics B, **79**, 679 (2004)

[97] W. Ketterle and D. E. Pritchard, *Trapping and focusing ground state atoms with static fields*, Applied Physics B: Lasers and Optics, **54**, 403 (1992)

[98] Heung-Ryoul Noh, Kazuko Shimizu, and Fujio Shimizu, *Imaging of an atomic beam with electrostatic lenses*, Physical Review A, **61**, 041601 (2000)

[99] Juris Kalnins, Glen Lambertson, and Harvey Gould, *Improved alternating gradient transport and focusing of neutral molecules*, arXiv:physics/0112073, **v1**, 21, (2001)